Precipitation behaviour and recrystallisation resistance in aluminium alloys with additions of hafnium, scandium and zirconium

An experimental investigation

by

Håkon Hallem

A thesis submitted to
The Norwegian University of Science and Technology (NTNU)
in partial fulfilment of the requirements for the degree of

Philosophiae Doctor

Trondheim

September 2005

Acknowledgements

The work presented in this thesis has been carried out at the Department of Materials Technology, the Norwegian University of Science and Technology (NTNU), Trondheim, during the period 2002-2005. This research was a part of the KMB project Heat Treatment Fundamental (Project no: 143877/213), funded by the Norwegian Research Council. Funding from the industry partners; Hydro Aluminium, Raufoss ASA and Elkem, through the Heat Treatment Fundamentals KMB project, is also gratefully acknowledged. Special thanks go to my supervisor, Prof. Knut Marthinsen, and co-supervisors Dr. Børge Forbord and Dr. Oddvin Reiso for their encouragement, enthusiasm, fruitful discussions and help they have given me through these three years. I would like to thank Dr. Børge Forbord specially for his friendship and for being an excellent colleague to work with. A special thank also to Prof. Nils Ryum who actually initiated this work.

Acknowledgements also goes to my colleagues at the Department of Materials Technology and SINTEF, in particular, Dr. Stian Tangen, Dr. Bjørn Holmedal, Mr. Hans Bjerkaas, Mr. Tor Nilsen, Dr. Jarle Hjelen, Mr. Wilhelm Dall, Ms. Tone Anzjøn, Ms. Birgitte Karlsen and Mr. Wouter Rittel who all assisted me during the work on this thesis. Dr. Jostein Røyset, Dr. Jan Sæter and Mr. Lars Auran at Hydro Aluminium are specially acknowledged for providing ideas and industrial viewpoints into my research. Special thanks also goes to William Lefebvre and Fredrik Danoix for the Atom Probe work done in Rouen (France). I would also thank PhD. Yancy Riddle for improving my TEM skills and Ms. Ingrid Page for the help with the manuscript.

To the rest of you, which I have forgotten: Thank You!

Finally I would like to thank my wife Irene and my two sons; Fredrik and Mats for being so patient during my time as a PhD-student.

Trondheim, September 2005

Håkon Hallem

Contents

Abstract

A comprehensive study of the effect of adding hafnium (Hf), scandium (Sc) and zirconium (Zr) to aluminium alloys has been carried out with a special focus on the effect of Hf, alone and in various combinations with Sc and Zr. These elements form finely dispersed precipitates with aluminium which are important to prevent recrystallisation in thermomechanically processed Al-alloys. The overall objective of the present work has been to optimize the addition of these dispersoid-forming elements to provide Al-alloys with the best possible recrystallisation resistance after extrusion.

The objective of the work presented in Part A was to identify adequate levels of Hf, Zr, Sc, Fe and Si in Al-Hf-(Zr)-(Sc)-(Fe)-(Si)-alloys with respect to: (i) obtaing a cast structure with a high supersaturation of Hf, Zr and Sc and without columnar grains and (ii) finding an adequate homogenisation procedure and to provide alloys with optimum recrystallisation resistance. The results showed that twinned columnar grains (TCGs) formed during solidification at high Hf-contents (~1,1 wt%) in both Al-Hf-Zr and Al-Hf-Sc alloys. However, when the Hf-content was kept below ~0.7 wt% a more equiaxed structure was obtained. From a selection of experiments a suitable homogenisation procedure for these alloys was found to be: slow heating (50^{o}C/hr) from room temperature to 475^{o}C followed by 5h-20h annealing time at this temperature. This is due to the fact that both Al_3Hf and Al_3Zr show poor precipitation when the heating rate is too fast. The effect of TCGs on the recrystallisation resistance after cold rolling was also examined. Despite the presence of twinned columnar grains a remarkably high recrystallisation resistance was found for Al-1,1wt%Hf-0,17wt%Sc, which remained unrecrystallised at 600^{o}C after 90% cold rolling

In Part B the nucleation and growth of dispersoids during homogenisation of Al-Zr-Sc-, Al-Hf-Sc and Al-Hf-Sc-Zr were studied in great detail by 3D atom probe and TEM investigations. A high number density of Sc-rich clusters was observed in the early stages of precipitation and these clusters subsequently transform to spherical Al_3Sc-dispersoids displaying a $L1_2$-structure. Further annealing results in segregation of Zr, Hf and more Sc to the dispersoid/α-Al matrix interfaces, and upon completion of precipitation annealing Zr-, Hf-, and Sc-containing “shells” were observed around already formed Al_3Sc-dispersoids. Due to the

precipitation of Al_3Sc dispersoids a dense and homogeneous distribution of dispersoids was observed, while the Hf and/or Zr which form the ”shell” slow down the coarsening of these dispersoids ($Al_3(Sc,Hf/Zr)$). This precipitation behaviour explains why alloys containing both Sc, Zr (and Hf) behave so well as far as recrystallisation resistance is considered (c.f. results in both Part A and Part C)

The objective of Part C was to study the effect of dispersoids on recrystallisation resistance of a variety of carefully selected alloys during extrusion and also after subsequent annealing and cold rolling of the extruded profiles. An Al-(Fe)-(Si) alloy with both Hf, Sc and Zr additions displayed a remarkable recrystallisation resistance as only thin surface layers recrystallised during post-extrusion annealing at 600^{o}C. The same alloy also revealed an unrecrystallised structure even after annealing of 100hrs at 500 and 550^{o}C. A variant containing only Hf was far less resistant towards recrystallisation as it recrystallised completely already during extrusion. A particular result worth mentioning is that an extruded Al-Sc-Zr alloy did resist recrystallisation even after 80% cold rolling and annealing 1hr at 600^{o}C.

From the investigations carried out in this thesis it has been shown that alloys containing both Sc, Zr (and Hf) performed best in terms of recrystallisation resistance, with Sc as the key element to ensure a homogeneous and dense distribution of dispersoids. It is further clear that hafnium can not replace neither zirconium nor scandium completely. Though, additions of hafnium in combinations with Sc and Zr can increase the dispersoid distribution/density and possibly make these alloys even more temperature stable during forming and annealing.

1 Introduction to the thesis

1.1 The purpose of the thesis

The overall objective for this work, is to provide the industry with aluminium alloys which after thermomechanical processing (e.g. rolling or extrusion) are able to withstand high temperatures without recrystallising, since recrystallisation of the material in this condition may lead to a significant deterioration of material properties (strength loss, anisotropic properties/texture, increased tendency to weld-cracking, decreased corrosion resistance and fracture toughness). Aluminium alloys with good properties at elevated temperatures have a potential use in high temperature applications where a high strength/weight ratio is required, for instance in the automotive & aerospace industry. Many components in automobiles and aircrafts are subjected to high temperatures, e.g. engine parts, fuselage and heat exchangers. In order to ensure that aluminium alloys, (e.g. AA3xxx), are considered for such applications in the future, alloys with satisfying mechanical properties at elevated temperatures are required. This is the basis for the investigations carried out in this work, and Figure 1.1 shows a typical process route for such alloys considered here.

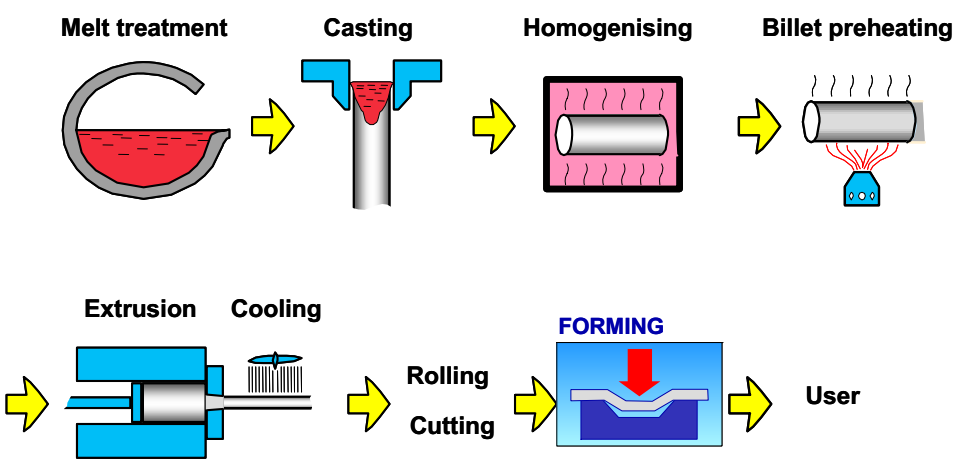

Figure 1.1 Typical process schedule for non-heat treatable aluminium alloys.

After extrusion (or rolling) the material is in a deformed state where the material has gained strength through strain hardening. To maintain the properties it is important to prevent recrystallisation during subsequent processing and/or normal service conditions, at elevated temperatures.

The use of dispersoids in aluminium alloys for controlling microstructure through the control of recovery, recrystallisation and grain growth is well established. Currently elements like Cr and Mn are commonly used as recovery, recrystallisation and grain growth inhibitors in aluminium alloys. However, these elements alone can not maintain a adequate structure at high temperatures and there has been an increasing interest in investigating the beneficial effects that can be achieved by adding rear earth elements to wrought aluminium alloys. Most of these studies have been carried out with scandium (Sc). In combination with a more common element industrially, zirconium (Zr), they display a remarkable behaviour concerning recrystallisation resistance at high temperatures.

A systematic development of Sc-containing aluminium alloys took place in the former USSR in the 1980's, and the interest for scandium as an alloying element in aluminium alloys hit the western world approximately 10 years later. Even though a number of improvements of Al alloys have been demonstrated through the addition of scandium, the current use of such alloys are still very limited. This is related to the very high price of scandium. [Røyset and Ryum (2005)]. Zirconium (Zr), on the other hand, which also alone gives improved capabilities of Al alloys, is cheaper than Sc and is today a relatively common alloying element

Other elements than scandium and zirconium which also have been investigated to a larger or and less extent are titanium (Ti), vanadium (V), and yttrium (Y). Hafnium (Hf) is an element which is positioned close to these elements in the periodic table and which thus is expected to have similar properties to the above mentioned elements. However, in spite of this, Hf is a relatively untried alloying addition to aluminium and little is known about the effect on microstructure and properties of Hf-containing Al-alloys. With this in mind the present work was set out with the following objectives:

- To increase the knowledge about Hf-containing aluminium alloys in general and to gain more insight about how Hf affect the microstructure and properties of Al-alloys. In particular the precipitation behaviour of such alloys; with Hf alone and in

combination with other dispersoid forming elements like Sc and Zr.

More specifically the work was designed to answer or shed light on the following questions:

- Will Hf affect the casting structure with resepect to grain size and segregation of elements, and to which extent will this affect the precipitation behaviour during subsequent processing?

- Which effects do hafnium have on microstructure and properties in general compared to more well known elements like scandium and zirconium?

- How does hafnium interact and perform together with scandium and/or zirconium in Al-Hf-(Sc)-(Zr) alloys?

- What is the performance of Al alloys with these different alloying elements alone and in various combinations in terms of recrystallisation behaviour?

Since both zirconium and hafnium are much cheaper than scandium, an important motivation for exploring the possible use of Hf as and alloying element is to which extent it may replace scandium and/or zirconium as the main alloying element. Moreover, Zr and Hf are always found together in natural combinations and are two of the most difficult elements to separate. It would therefore be an extra cost benefit if these elements can be used together.

To investigate these aspects, a number of different Hf containing alloys have been produced and investigated with respect to precipitation behaviour and recrystallisation resistance.

1.2 The structure of the thesis

The thesis begins with an introductory chapter giving some theoretical background starting with the different alloying elements/systems. Some relevant theory concerning precipitation, recrystallisation and coarsening is also given in this chapter. Then a chapter covering the alloy selection, processing of the materials and a general introduction to the experimental techniques used to characterise the materials is presented. The actual experimental investigations of the thesis are divided into three parts, Parts A-C, written as separate chapters. However, each part considers aspects of the same main objective, i.e. precipitation of dispersoids. These parts are as follows:

Part A:
Investigations to identify adequate levels of Zr, Sc, Fe and Si in Al-Hf-(Zr)-(Sc)-(Fe)-(Si)-alloys and to find an appropriate annealing procedure of these alloys, both aspects in view of the precipitation behaviour and eventual recrystallisation resistance after cold rolling.

Part B:
Investigations to study nucleation and growth of dispersoids during homogenisation of Al-Hf-Sc and Al-Hf-Sc-Zr by 3D atom probe and TEM.

Part C:
Investigations to study the effect of dispersoids on recrystallisation resistance in Al-Hf-(Zr)-(Sc)-(Fe)-(Si)-alloys after extrusion, and also after subsequent annealing and cold rolling of the extruded profiles.

2 Theoretical background

In the theoretical background, the two first parts (Chapters 2.1 and 2.2) give a general introduction to the different alloy systems studied in this work with phase diagrams and some elements of their precipitation characteristics. The second part (Chapters 2.3 to 2.6) discusses different aspects of the various processing steps (cf. Fig. 1.1) together with important microstructural phenomena which occur during processing and some relevant theory.

2.1 Alloy systems

Aluminium-Hafnium alloys

The Al rich part of the Al-Hf system was first studied by Rath et al. (1960) and the phase diagram is similar to that of the more well-known Al-Zr system which is given by Fink and Willey (1939). The maximum solubility of Hf in Al is according to Rath determined to be 0,186 at%Hf (~1,22 wt%Hf), at a peritectic temperature of 662,2^{o}C (see Figure 2.1).

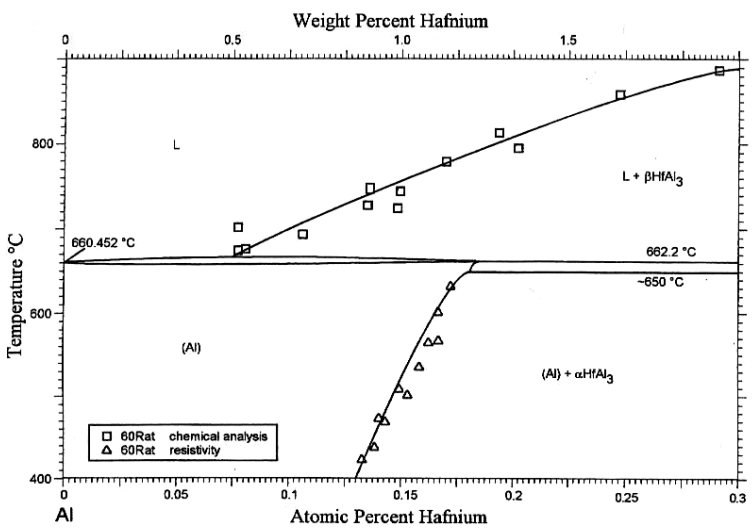

Figure 2.1 Al-Hf phase diagram [Murray et al. (1998)].

Norman and Tsakiropoulos (1991, 1992) studied the effect of Hf in Al, using rapid solidification. They observed that with a Hf level above 2wt%, primary Al_3Hf was obtained. Moreover the grain size decreased with increasing alloy composition and the $L1_2$-Al_3Hf phase (c.f chapter 2.2) acted as a grain refiner, reducing the grain size from 300 μm to 5 μm. Hori et al. (1980) have also shown that the grain size decreases with increasing Hf levels above ~2-3 wt%.

Aluminium-Zirconium alloys

Zirconium is peritectic with Al and the maximum solubility of Zr in Al is 0.28wt%, see Figure 2.2. Arjuna et al. (1997) found Zr to be a potential grain refiner in Al-alloys at high concentrations (2wt%). However, they also reported that Zr has a "poisoning" effect (interrupting the effect of the grain refiner) when other grain refining elements are added, e.g. Ti and B.

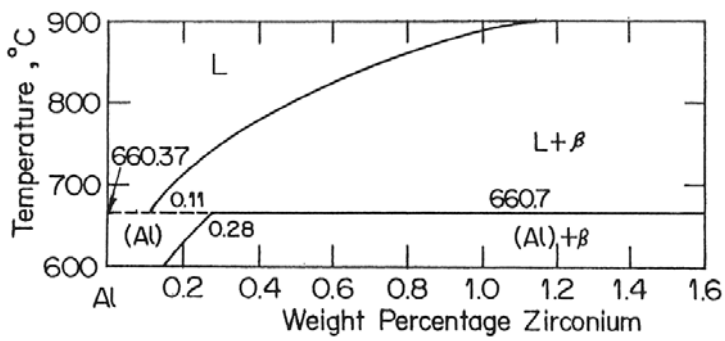

Figure 2.2 Al-Zr phase diagram where β is Al_3Zr [Rajagopalan (1999)].

Aluminium-Scandium alloys

One of the first publications of the complete Al-Sc phase diagram in English was by Russian scientists in 1964 [Savitsky et al. (1964)]. In the Al-Sc system the equilibrium eutectic solidification takes place at a temperature of about 660°C (Figure 2.3) and with a composition of ~ 0,55wt% Sc [Røyset (2002), Røyset and Ryum (2005)]. The maximum solubility for Sc in Al is 0,38 wt%.

Sc has a grain refining effect making small equiaxed grains form instead of long dendrites which can reduce porosity and hot-cracking. Norman et al. (1998) showed that hypereutectic (>0,55wt%) addition of Sc to Al is

effective in reducing as-cast grain size. They also showed that the change from large dendritic grains to fine spherical grains is realised by the addition of Sc to Al. When adding other elements to an Al-Sc alloy this grain refining limit will usually be shifted to a lower Sc level .

The most promising combination with Sc so far with respect to recrystallisation resistance is Zr, due to fast precipitation and slow coarsening of the dispersoids [Riddle (2000), Røyset and Ryum (2005)]. An isothermal section of the Al-Sc-Zr phase diagram is shown in Figure 2.4.

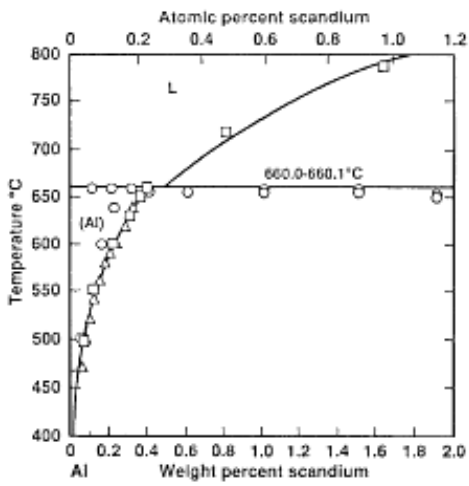

Figur 2.3 Al-Sc phase diagram [Murray et al. (1998)].

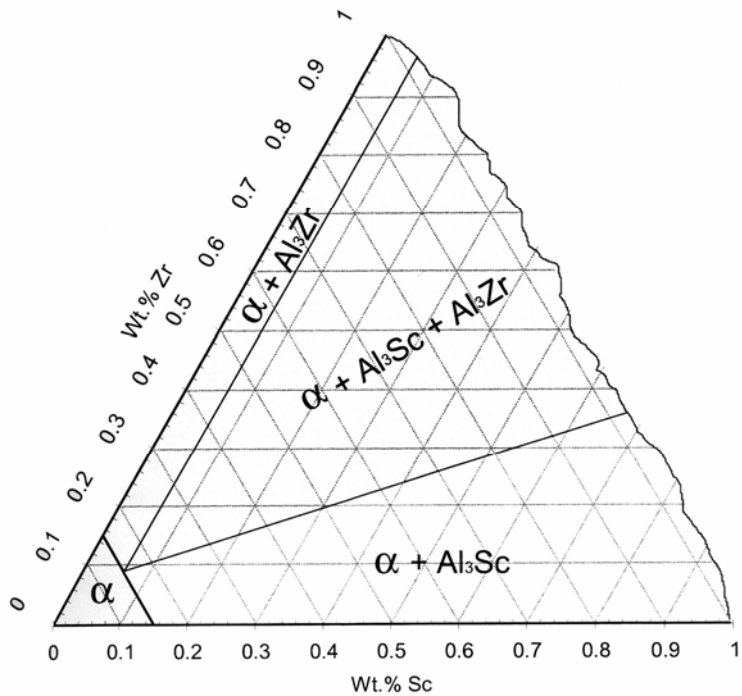

Figur 2.4 Re-drawn isothermal section of the Al-corner of the Al-Sc-Zr phase diagram at 600°C from Røyset and Ryum (2005).

2.2 Precipitation of Al -(Hf), -(Sc) and -(Zr)

The structure of the phases

When Hf, Sc and Zr together with aluminium do form precipitates in these alloys (alone or in combination) during annealing they form metastable phases of $L1_2$ structure or stable phases with $D0_{22}$ or $D0_{23}$ structure. Figure 2.5 illustrates the different unit cells of these structures [Harada (2000), (2002)]

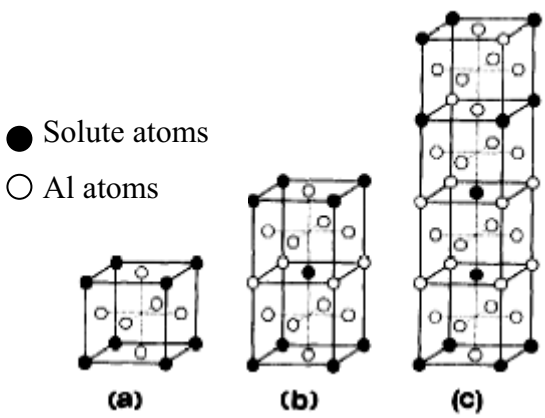

Figure 2.5 The unit cells of the three structures, a) $L1_2$-structure, b) $D0_{22}$-structure and c) $D0_{23}$-structure.

Precipitation in hafnium containing alloys

Rath et al. (1960), Potzschanke and Shubert (1962) and Tsyganova et al. (1970) were the first ones to study equilibrium phases in the Al-Hf system. However, few studies on precipitation of metastable phases in Al-Hf alloys have been reported. Ryum (1975) observed heterogeneously distributed dispersoids which were coherent with the matrix after long annealing time at >400°C in an Al-1,78wt%Hf alloy. Ryum also observed discontinuously precipitated dispersoids in the same alloy at lower annealing temperatures, 200°C (see Chapter 2.5.1 for an explanation of discontinuous and continuous precipitation). Hori et al. (1980), on the other hand, were not able to observe any continuous precipitation in an Al-1wt%Hf even after 2000 hrs at 450°C. This indicates that Al_3Hf dispersoids are extremely difficult to precipitate in binary Al-Hf-alloys. However, when Al_3Hf forms, it forms meta-stable coherent dispersoids ($L1_2$) which has a $D0_{23}$ and/or a $D0_{22}$ equilibrium form [Boller et al. (1960), Murray et al. (1998)]

Precipitation in zirconium containing alloys

To date the most effective dispersoids to prevent recrystallisation used in industry is Al_3Zr. During thermo-mechanical processing the presence of a fine dispersion of spherical and coherent metastable Al_3Zr dispersoids having cubic ($L1_2$) structure ($D0_{23}$ equilibrium phase), is well known to

inhibit recrystallisation in a wide range of aluminium alloys. This is done by pinning the moving grain boundaries, also called Zener drag , see Chapter 2.5.6 [Riddle (2000), Forbord (2004b), Humphreys and Hatherly (1995)].

Studies of ternary Al-alloys containing Zr and Si contents indicate that there is a critical amount of each solute element required in order to enable precipitation of Al_3Zr [Westengen (1980), Reiso (1980)]. Below these critical amounts, Al_3Zr will not precipitate resulting in microstructures which have limited resistance to recrystallisation (see Chapter 2.2.1). Furthermore the same studies showed that the preheating condition, including heating rate to the preheating temperature affected the distribution of Al_3Zr when it did precipitate. In many cases heterogeneous pockets of Al_3Zr and/or preferential nucleation on boundaries are observed.

Precipitation in scandium containing alloys

Al_3Sc form an $L1_2$ structure which precipitate more homogeneous than Al_3Hf or Al_3Zr, and thereby exerting larger recrystallisation resistance in these alloys. Some areas in which scandium can be used are: (i) As a grain refiner. As mentioned earlier, Sc can act as a grain refiner due to precipitation of particles. (ii) To control of grain structure by dispersoids. (iii) As a mean to precipitation strengthening. On a per-weight basis Sc imparts the highest precipitation strengthening effect over any other principal alloying element, as is shown in Table 2.1 by Drits et al.(1984).

Table 2.1 Comparing of strengthening effect/volume fraction for different alloys Drits et al. (1984)

Alloy (wt%)	**$\Delta\sigma(YS)/f_v$ (MPa / %)**
Al-6Cu-0,4Mn	18,7
Al-4Cu-1,5Mg	38,3
Al-4,2Cu-0,6Mg-1Si	41,4
Al-5,5Mg-2,8Li	48,0
Al-6Zn-2,3Mg-1,7Cu	62,9
Al-4,5Zn-1,8Mg	84,6
Al-1Mg-0,6Si-0,25Cu	84,8
Al-0,5Sc	250,0

Combination of elements; Hf, Sc and Zr

It has been reported in the literature that elemental substitution exists in dispersoids in alloys with these elements allowing zirconium and scandium containing Al-Sc-Zr alloys to precipitate $Al_3(Sc_{1-x}Zr_x)$ phases. Alloys with this combination of elements are so far the most promising with respect to recrystallisation resistance. The addition of Zr, only marginally affects the initial stage of the precipitation, while it slows down the coarsening rate of the dispersoids ($Al_3(Sc_{1-x}Zr_x)$) much compared with Al-Sc alloys [Zakharov (1997)]

Al alloys with Hf are not frequently reported in the literature, but Zakharov (1994) mention combinations of Al-Hf-Zr, Al-Hf-Sc and Al-Hf-Sc-Zr. When adding Hf to an Al-0,2wt%Sc alloy, a $Al_3(Sc_{1-x},Hf_x)$ phase is formed. The dispersity of these particles is higher than for Al_3Sc, but less than for $Al_3(Sc_{1-x},Zr_x)$. It is also concluded that more hafnium than 0,15wt% should be added to gain a better or satisfying effect.

2.2.1 Effect of addition of Fe and Si on precipitation

Depending of the composition, the binary systems (Al-Hf, Al-Sc and Al-Zr) can form different intermetallic phases with other elements like Fe and Si which are normally present in industrial Al-alloys. The precipitation of these phases can potentially affect the precipitation of the Al_3X types of dispersoids. Below the effect of Fe and Si is discussed.

Effect of Fe

Fe does not form ternary compounds with aluminium (AlScFe) or binary compounds with scandium (ScFe) [Røyset (2005)]. The only phases which form are probably pure aluminium, Al_3Sc, Al_3Fe. Fe has small or no effect on the solubility of Sc in Al or on the precipitation kinetic of Al_3Sc. However, Fe can affect the recrystallisation resistance at Al-Sc alloys. It has been observed that the recrystallisation resistance of an Al-0,4wt%Sc alloy was reduced from 580°C to 570°C by adding 0,7wt%Fe [Zakharov (1994)]. No similar observations are reported in the literature concerning the effect of Fe on the recrystallisation properties of Al-Hf or Al-Zr alloys.

Effect of Si

In the Al-Sc-Si system: Si, Al_3Sc, ScSi and a ternary phase called V-phase (Sc_2AlSi_2) have been found in equilibrium with the α-matrix. The latter phase "consume" the Sc and reduces the possibilities to form large volume fractions of Al_3Sc, which in turn leads to a reduced recrystallisation resistance [Tyvanchuk et al. (1988), Kharakterova et al. (1994)]. It is also well known that Si additions affect precipitation in Al-Zr alloys [Westengen et al. (1980), Reiso et al. (1980)], and this is also the case for Al-Hf alloys [Hallem et al. (2004)]. This means that cautions should be taken when Si is added to these types of alloys.

2.3 Solidification and homogenisation

2.3.1 Directional solidification

Generally in aluminium castings, the solidification pattern gives a good indication of where shrinkage porosity will be located. Directional solidification in aluminium castings reduces (or eliminates) porosity. The directional solidification technique allows components to be produced from the melt in a single-stage process, and leads to a composite of phases that are thermodynamically stable, chemically compatible, well aligned and finely dispersed. Directional solidification is therefore the solidification procedure used in this work

2.3.2 Twinned columnar grains (TCG)

A microstructural feature which sometimes occur during solidifications is the formation of socalled twinned columnar grains (TCG). TCGs are often termed feather crystals because of the feather shaped pattern observed on macro-etched sections. However, when the feather crystals are observed at high magnifications they are found to consist of twinned grains. TCGs have often been found to form in cases where the grain refinement has been poor [McCartney (1989)]. Previous investigations [Arjuna (1997)] have shown that the formation of such crystals quite often is connected to the amount of alloying elements, which is the case in the present work as far as it concerns Zr and Hf.

According to literature TCGs are most likely formed if (i) the temperature gradient ahead of the solidification front is steep, (ii) the cooling rate is high and/or (iii) the grain refinement has been insufficient. However, their growth kinetics is not fully understood [McCartney (1989)]. It has been suggested that a TCG has a much smaller tip radius than a normal columnar dendrite. This is believed to lead to a more efficient rejection of solute than is the case for normal dendrites, leading to a more rapid growth at a given columnar front undercooling ΔT_C.

2.3.3 Homogenisation

The homogenisation process generally has to main goals; 1) to remove the effects of microsegregation during casting and dissolve the large, soluble eutectic intermetallic particles that degrade the properties and 2) to precipitate second phase particles. From literature a heating rate of ~50^{o}C/hr up to temperatures around 450-475^{o}C has been found suitable for these types of alloys to get good precipitation [Røyset and Ryum (2005), Riddle et al. (2002), Westengen et al.(1980)]. However, adequate holding times can vary for different alloys. It should be mentioned that Forbord (2004b) have shown that in alloys which contain both Sc and Zr, homogenisation is not always necessary to get the desired precipititation behaviour in these alloys.

Ramping can also be important so slow diffusing elements like Hf and Zr do get necessary time to form the appropriate dispersoids, $Al_3(Sc,Zr)$ or $Al_3(Sc,Hf)$ [Forbord et al. (2004a), Hallem et al. (2004b)].

2.4 Deformation

2.4.1 Characterization of the deformed structure

Cells and subgrains

During deformation processes like extrusion and rolling, characteristic deformation microstructures do form in the material. At small strains ($\varepsilon < 0.5$) a typical deformation structure in Al may be described by four parameters (see Figure 2.6 a); cell size (δ), cell wall thickness (h), wall dislocation density (ρ_b), and the dislocation density in the interior of the cells (ρ_i). Increasing strain ($\varepsilon > 0.5$) leads to more accumulation of

dislocations in the boundaries, which make them become more well defined and with a definite misorientation. The cell structure has now been replaced by a subgrain structure consisting of well-defined subgrain boundaries with a sharp misorientation. The microstructure may in this condition be described by three parameters (see Figure 2.6 (b)); i.e. the subgrain diameter (δ), the interior dislocation density (ρ_i), and the boundary misorientation (φ) [Nes (1998)].

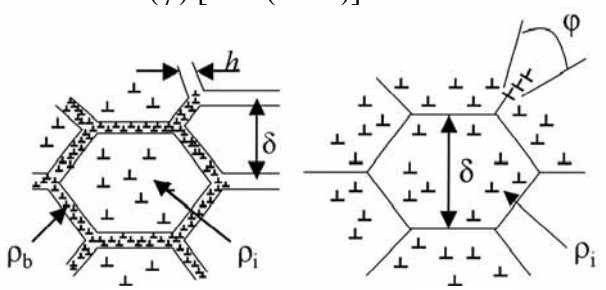

Figure 2.6 A schematic microstructural description of deformed aluminium at (a) small strains and (b) large strains.

The driving pressure for possible subsequent recrystallisation is derived from the energy stored in the dislocation substructure formed during deformation. This driving pressure is most conveniently represented by the stored energy associated with the subgrains and the internal dislocation network, as follows:

$$P_D = \rho_i \Gamma + \frac{\alpha \gamma_{SB}}{\delta} \tag{2.1}$$

where ρ_i is the dislocation density in the interior of the subgrains, Γ is the dislocation line tension ($\Gamma \sim Gb^2/2$), α is a geometric constant ($\alpha \sim 3$), δ is the subgrain size and γ_{SB} is the energy of the subgrain boundaries, given by the Read-Shockley (1950) relation:

$$\gamma_{SB} = \frac{Gb}{4\pi(1-\nu)} \varphi \ln\left(\frac{e\varphi_c}{\varphi}\right) \tag{2.2}$$

where G is the shear modulus, b is the burgers vector, ν is the Poisson ratio, φ is the angle of misorientation and φ_c is the critical misorientation for a boundary to be defined as a high angle boundary (of the order 15°).

Application of the Read-Shockley relation assumes a periodic, equiaxed substructure, which at least is a reasonable assumption for a hot deformed aluminium alloy. The following expression for the driving pressure is thus obtained:

$$P_D = Gb^2 \frac{\rho_i}{2} + \alpha \frac{Gb}{4\pi(1-\nu)} \frac{\varphi}{\delta} \ln\left(\frac{e\varphi_c}{\varphi}\right) \tag{2.3}$$

As the dislocation density inside the subgrains is usually responsible for only 1-2% of the total stored energy, a simplified expression can be calculated directly from the subgrain size (δ) and the misorientation across subgrain boundaries (φ) as:

$$P_D = k \frac{\varphi}{\delta} \tag{2.4}$$

where k is a constant.

Cold versus hot deformation

In hot working, corresponding to the deformation conditions one have during extrusion and hot rolling, deformation takes place at elevated temperatures. Under such conditions dynamic recovery (i.e. annihilation of dislocations which counteract accumulation of dislocations, see also section 2.5.2) do take place. This reduces the amount of work hardening in the material and keeps the flow stress of the material at a reasonably low level, thus enabling it to be deformed more easily. During cold working on the other hand, dynamic recovery, which is a thermally activated process is suppressed and the material work hardens much more severely, making the material much more difficult to deform. This is reflected in the materials microstructure through a much higher stored density of dislocations and smaller subgrains. Referring to Eq. 2.3 we see that this means a much higher amount of stored energy, and thus a much higher driving force for recrystallisation in cold worked material. This means that a cold worked material may recrystallise much more easily than a hot deformed material, which again put stronger demands on the

recrystallisation resistance of the material if one wants to prevent recrystallisation even after cold deformation. For more details it is referred to e.g. Humphreys and Hatherly (1995).

2.4.2 Deformation heterogeneities

Two conditions are necessary for the nucleation of new strain free (recrystallised) grains in a deformed matrix: (i) locally a large amount of stored energy and (ii) large misorientation gradients. These conditions are found at socalled deformation heterogeneties in the material which develop during deformation. Deformation heterogeneities acts as nucleation sites for recrystallisation and will thereby promote such a process. Typical deformation heterogeneities found in aluminium are listed below [Humphreys and Hatherly (1995)]:

- Deformation zones surrounding coarse second phase particles
- Slip bands/micro bands
- Transition bands
- Shear bands

An important and often the most dominant nucleation mechanism in aluminium alloys is related to deformation zones surrounding coarse second phase particles. This mechanism, called particle stimulated nucleation of recrystallisation (PSN) has also been observed during this investigation, and is described somewhat more detailed in the following.

Deformation zones surrounding coarse second phase particles

When a matrix containing hard second phase particles is deformed, strain incompatibilities arise around the particles. In order to account for this geometrical effect, an arrangement of geometrically necessary dislocations needs to be introduced. Consequently, deformation zones are gradually being built up around the hard non-deformable particles as illustrated in Figure 2.7. The deformation zones are characterized by a rotated zone in front and behind large particles, surrounded by a distorted region, and it is generally accepted that the deformation zones extend to a distance equal to about a particle diameter from the surface of the particles (see also section 2.5.6).

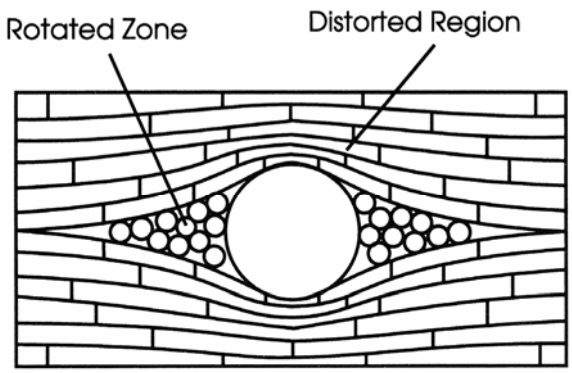

Figure 2.7 Schematic illustration of a deformation zone surrounding a coarse particle [Porter and Humphreys (1979)].

2.4.3 Dynamic recrystallisation

Dynamic recrystallisation is frequently observed during hot deformation of ordered alloys. This phenomenon generally starts at the old grain boundaries, and is to be expected in materials where recovery is slow and there is a retention of large amounts of stored energy. After deformation to large strains, particularly at elevated temperatures, a microstructure consisting predominantly of high-angle grain boundaries may be formed. Such a microstructure is similar to that resulting from conventional recrystallisation, but because no recognisable “nucleation” and “growth” of the recrystallised grains occur, and the microstructure evolves relatively homogeneously throughout the material, the process can reasonably be classified as continuous recrystallisation or also called geometric dynamic recrystallisation [Humphreys and Hatherly (1995)].

2.5 Microstructural reactions during annealing

2.5.1 Precipitation during annealing

Precipitation kinetic

Røyset and Ryum (2005) suggested that if one assumes that the Johnson-Mehl-Avrami-Komolgorov (JMAK) relationship is valid for the precipitation reaction, one can express the fraction transformed X as a function of the reaction time t by the equation

$$X(t)=1-exp[-kt^n] \quad (2.5)$$

Here k is a constant and the exponent n is dependent on the nucleation rate. For a situation described by Hyland (1992) where the precipitates nucleate at a constant rate, the theoretically value of n is equal to 5/2 [Christian (1975)].

Røyset and Ryum (1998) studied an Al-Sc alloy and applied a heat treatment procedure quite similar to the one used by Hyland (1992). Under such conditions one should expect the precipitation kinetics also to be quite similar. However, Røyset and Ryum (1998) reported that the exponent n of the JMAK relationship was approximately 1.65–1.85 for the temperature range of concern. This result does indicate large deviations from the condition of a constant nucleation rate. It is rather more what one should expect in the case of site saturation nucleation kinetics, i.e. the condition that all the particles are nucleated simultaneously, which in the JMAK equation would yield an exponent n of 3/2.

The precipitation in Al-Hf and Al-Zr is reported to be much more heterogeneous and have a much larger variation in dispersoid size than in the Sc containing alloys [Ryum (1969), Ryum (1975), Forbord (2004b), Hallem et al. (2004)]. From these observations it is not reasonable to make the same assumption as for the Sc-free alloys like Al-Hf and Al-Hf-Zr as for Sc containing alloys, i.e. site saturation nucleation kinetics.

Continuous precipitation

Continuous precipitation of $Al_3Hf/Al_3Sc/Al_3Zr$ is a bulk decomposition process of supersaturated solid solution of Hf/Sc/Zr in Al and can in the isothermal case be characterised by a nucleation stage, a growth stage,

and finally a coarsening stage. It may be described as a diffusional reaction in a multi-component system in which atoms are transported to the growing nuclei by diffusion over relatively large distances in the parent phase and during which the mean composition of the parent phase changes continuously towards its equilibrium value. Continuous precipitation is usually the desired precipitation mode to obtain a fine dispersion of homogeneously distributed dispersoids.

Discontinuous precipitation

Under certain conditions, precipitation is dominated by a different precipitation mode called discontinuous precipitation. Discontinuous precipitation has been reported from investigations of Al-Hf [Norman (1991)], Al-Zr [Ryum (1969), Nes and Billdal (1977)], Al-Sc [Blake and Hopkins (1985) , Røyset and Ryum (1998), Norman et al. (1998)] and Al-Sc-Zr [Riddle (2000), Hallem (this work, Figure 2.9)] alloys. This precipitation mechanism is sometimes referred to as cellular precipitation, and in the alloys described in this work it may be described as decomposition of supersaturated solid solution into α-Al and Al_3X (X = Sc, Hf and Zr) at a moving grain boundary. As the grain boundary moves, it leaves behind a characteristic fan-shaped array of precipitates. Consequently, the matrix orientation of the discontinuously transformed volume may change from its original orientation, i.e. the discontinuously transformed volume appears as a new separate grain of a different orientation (or in some cases a perturbation of a pre-existing grain boundary). Normally the transformation rate of discontinuous precipitation is controlled by grain boundary diffusion on the transformation front, while in continuous precipitation the growth rate depends on volume diffusion.

Discontinuous precipitation is most frequently reported in alloys with Sc contents above 0,4wt% [Blake and Hopkins (1985), Norman et al.(1998)], and Røyset and Ryum (2005b) suggested an TTT diagram for the different precipitation mechanisms in an Al-0,2wt%Sc alloy (see Figure 2.8). Discontinuous precipitation is also frequently observed in Al-Hf and Al-Zr alloys, e.g. Norman and Tsakiropoulos (1991) found tree distinct morphologies of rod/filament like discontinuous precipitates in an Al-Hf alloy.

As a result of their rather coarse nature and inhomogeneous dispersion, discontinuously precipitated Al_3X do not contribute to any large extent to

the strength of the alloy, and also leads to a smaller amount of alloying element in supersaturated solid solution being available for subsequent continuous precipitation. This in turn also leads to a lower recrystallisation resistance. Thus discontinuous precipitation is in general regarded as an undesired precipitation mode. Figure 2.9 shows discontinuous precipitation (feather shaped) and continuous precipitation (white dots) in an Al-0,15wt%Sc-0,15wt%Zr alloy.

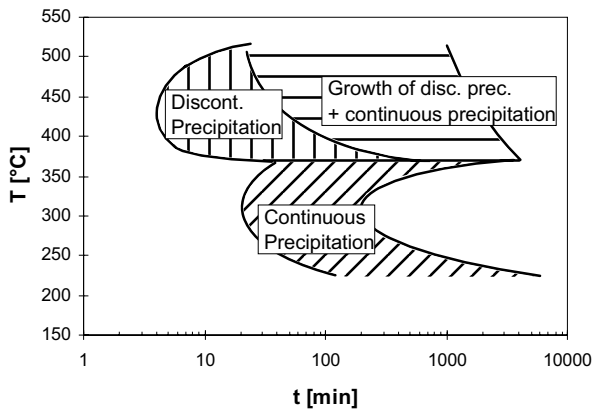

Figure 2.8 TTT diagram of precipitation in Al-0,2wt%Sc alloy after solutionising at 600°C and direct quench to aging temperature [Røyset and Ryum (2005b)]

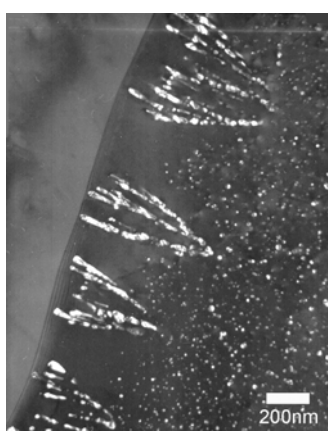

Figure 2.9 Al-Sc-Zr alloy showing dis- and continuously precipitation [Hallem, present work] after 50°C/hr to 475°C for 20hrs.

2.5.2 Recovery

Recovery is usually defined as the softening reactions taking place prior to nucleation of new and strain free grains. For high stacking fault energy materials, such as aluminium, dislocation climb and cross slip occurs readily, and the deformed material recovers to form subgrains also at low deformations and/or annealing temperatures. The dislocation density within the interior of the subgrains decreases during the recovery process. The energy of a boundary increases with misorientation, but the energy per dislocation decreases with misorientation, *i.e.* there is a driving force to form fewer and more misoriented boundaries.

The magnitude of recovery contributing to the softening reactions depends on the rate of recovery compared to the nucleation- and growth rate of the recrystallised grains. It is often assumed that the recovery rate is controlled by subgrain growth in heavily cold deformed materials. In accordance with Eq. 2.3 and/or 2.4 recovery thus lowers the driving pressure for recrystallisation, and also the kinetics of the recrystallisation process (cf. Eq. 2.7 given in Chapter 2.5.3).

2.5.3 Recrystallisation mechanisms

Static recovery and static recrystallisation are competitive mechanisms during annealing of wrought alloys. Recrystallisation is a softening reaction defined by nucleation and growth of new dislocation free grains at the expense of the deformed microstructure. Even after considerable recovery the microstructure still contains large amounts of stored energy, and a further reduction is obtained by recrystallisation. Recrystallisation by nucleation and growth is often called primary- or discontinuous recrystallisation. If nucleation of recrystallisation is to occur, then the nucleus must have a size advantage and a misorientation advantage by being partly or fully surrounded by a high angle grain boundary (e.g. Humphreys and Hatherly, 1995). The kinetics of recrystallisation is analogous to other phase transformation controlled by nucleation and growth.

Nucleation of recrystallisation

The normal process of recrystallisation in metals is the formation of small regions of nearly perfect crystals (nuclei; typically at deformation heterogeneities as discussed in Chapter 2.4.2) and the growth of these into the surrounding deformed material. The critical size of a nucleus can be calculated by the Gibbs-Thompson relation:

$$\delta > \delta_c = \frac{4\gamma_{GB}}{P_D - P_Z} \tag{2.6}$$

where δ is the diameter of the deformation free volume, γ_{GB} is the specific grain boundary energy and P_D is the stored energy given by Eq. 2.1 and 2.3. P_Z is the Zener drag for situations where a fine dispersion of small particles is present, as defined later by Eq. 2.17 in Chapter 2.5.6. A grain fulfilling the requirement of equation 2.6 will grow with a growth rate G given by:

$$G = M\left(P_D - P_Z - \frac{2\gamma_{GB}}{R}\right) \tag{2.7}$$

where M is the mobility of the grain boundary defined by:

$$M = \frac{M_0}{RT}\exp\left(\frac{-U_{GB}}{RT}\right) \tag{2.8}$$

where M_0 is a constant, T is the annealing temperature, R is the universal gas constant and U_{GB} is the activation energy for grain boundary migration. Moreover, if the standard assumption of site saturation nucleation and a random distribution of nucleation sites can be applied, the following transformation kinetics law is obtained:

$$X(t) = 1 - \exp\left[-\frac{4}{3}\pi N_{TOT}(Gt)^3\right] \tag{2.9}$$

where $X(t)$ is the fraction recrystallised after an annealing time t.

The concept of nucleation in recrystallisation is diffuse. However, a strain free grain of a size determined by equation 2.6 is required in order to provide further growth. The process prior to this stage, *i.e.* the nucleation

reaction, requires growth or coalescence of subgrains/sub-boundaries. In any case, equations 2.7 and 2.9 will determine the transformation rate.

2.5.4 Flow stress

The combined effect of static recovery and recrystallisation on mechanical properties during annealing after hot or cold deformation may be given by the following relationship [Vatne et al. (1996, 1998), Sæter (1998)] :

$$\sigma_y(t,T) = \sigma_{y,0} + MG_0 b\left(\alpha_1\sqrt{\rho_i(t,T)} + \alpha_2\left(\frac{1}{\delta(t,T)}\right)\right)\left(1 - X_{rex}(t,T)\right) \quad (2.10)$$

Eq. 2.10 gives the yield stress, $\sigma_y\ (t,T)$ at a given time (t) and temperature T. $\sigma_{y,0}$ is the yield stress of the undeformed material, G_0 is the shear modulus at room temperature, M is the Taylor factor and α_1 and α_2 are material constants. $\rho_i(t,T)$ and $\delta(t,T)$ are the instantaneous mean values of the cell interior dislocation density and the subgrain size, respectively, at a given time and temperature due to static recovery (see Figure 2.6).

From Eq. 2.10 we see that if recrystallisation can be prevented, the variation in mechanical strength during annealing is given by the recovery part alone and is proportional to the cell interior dislocation density and inversely proportional to the sub-grain size. Often the latter is the dominating part and the drop in mechanical strength will be governed by possible sub-grain growth.

2.5.5 Particle free systems

To get the nuclei to grow and become a recrystallised grain in a particle free system, the grain must have a critical size as given by equation (2.11) (cf. Eq. 2.6).

$$R_c = \frac{2\gamma_{GB}}{P_D} \quad (2.11)$$

Here R_c is a critical particle radius, P_D the driving force (as defined in Eqs. 2.3 and 2.4) and γ_{GB} is the grain boundary energy.

The first model for nucleation of recrystallisation, proposed by Cahn (1950), is subgrain growth. Deformation of (unalloyed) aluminium results in the formation of subgrains. These subgrains often contain a localised high density of dislocations near subgrain boundaries creating a misorientation between neighbouring subgrains. If the misorientation angle is low (1-5°) then the subgrain boundary may move by annihilation and incorporation of dislocations from the matrix. This increases misorientation between neighbouring subgrains and leaves a strain free grain behind the advancing boundary.

At about the same time as the subgrain growth model, Beck and Sperry (1950) developed the SIBM (strain induced boundary migration) model using observations in deformed high purity Al. Under SIBM, neighboring subgrains contain a difference in dislocation density. During annealing the boundary between these two grains minimises the energy of the system by bulging into the subgrain containing material associated with the highest stored energy. Equilibrium conditions show that the bulges created should approach a tip angle of 120°. As annealing continues the bulge penetrates further into and consumes the high energy (deformed) matrix. This volume contained by the bulge along boundaries is considered to be a recrystallised grain.

Subgrain coalescence is another model that was proposed by Hu (1962) and further developed by Li (1962) and is related to subgrain growth. Subgrain coalescence also considers the rotation of subgrains that are created during deformation. If the original misorientation between subgrains is small (1-5°) then it is thermodynamically favourable for these subgrains to minimise these misorientation by rotating towards each other. This rotation minimises the energy between boundaries. When the two grains no longer are misorientatied, recrystallisation is considered to have occurred locally.

2.5.6 Particle containing systems

There are two mechanisms that affect recrystallisation in systems containing second phase particles. Particle size and spacing dictate whether the second phase will act as a site to nucleate recrystallisation, termed particle stimulated nucleation (PSN), or whether it will retard recrystallisation by dragging boundaries, termed Zener drag.

Particle stimulated nucleation (PSN).
Since the observations by Humphreys (1977, 1979) there have been a general acceptance that nucleation at deformation zones developed around coarse second phase particles is an important nucleation mechanism in commercial particle containing alloys, and particularly after cold deformation (see Chapter 2.4.2) and/or high Zener-Hollomon parameters:

$$Z = \dot{\varepsilon} \exp\left(\frac{Q}{RT}\right) \tag{2.12}$$

Where $\dot{\varepsilon}$ and T are the strain rate and temperature during deformation, respectively and Q is the activation energy.

The main parameters that determine the occurrence of PSN are the strain, particle size and Zener Hollomon parameter as observed in Figure 2.10. During low temperature deformation the energy stored in the deformation zones is relatively large, and the critical step in the nucleation process is assumed to be the growth of new grains out of the deformation zone. For a successful particle stimulated nucleation event, the deformation zone has to be larger than a critical value (λ_C), or equivalently, the particle has to be larger than a critical particle diameter ($\eta_C = \lambda_C / 3$). A mathematical expression for the critical particle size for successful particle stimulated nucleation follows from the Gibbs Thomson relationship and may be expressed as follows [Nes (1980)]:

$$\eta_C = \frac{\lambda_C}{3} = \frac{4\gamma_{GB}}{(P_D - P_Z)} \tag{2.13}$$

where again P_D is the driving pressure for recrystallisation provided by the stored energy and P_Z is the Zener drag.

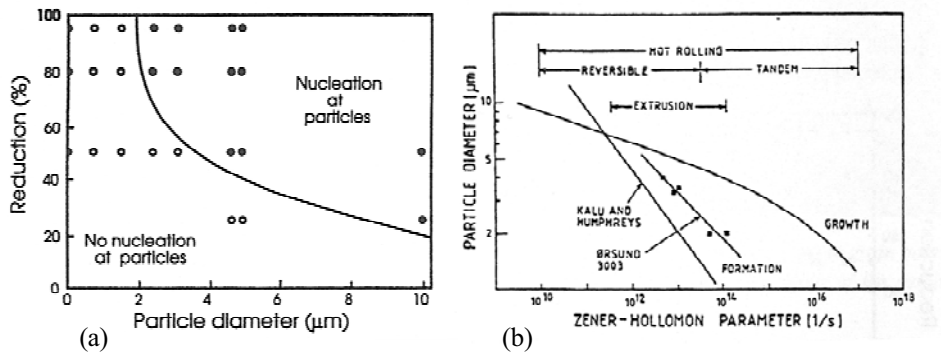

Figur 2.10 (a) The effect of particle size and rolling reduction on particle stimulated nucleation (Humphreys, 1977). (b) The effect of Zener-Hollomon parameter on the formation and growth of nuclei formed during particle stimulated nucleation (Furu *et al*., 1993).

During high temperature deformation the formation of deformation zones around the particles are strongly retarded due to annihilation of dislocations during dynamic recovery and the critical particle diameter for nucleation increases because large enough deformation zones do not form at the smallest particles. This situation has been treated by Humphreys and Kalu (1987), who observed that the critical particle diameter to form a deformation zone at temperature T is given by:

$$\eta_C = \left(\frac{K}{TZ}\right)^{1/3} \tag{2.14}$$

where K is a constant and Z is the Zener-Hollomon parameter (see Eq 2.12).

In addition, the stored energy of deformation is lowered at high deformation temperatures, altering the conditions for growth of a nucleus. The condition for nucleation by PSN is given by formation and growth as a function of Z. Experimental investigations by Furu *et al.* (1993) have shown that AA3003 and AA3004 alloys deformed at $Z>10^{12}$/s indicated growth controlled nucleation, while measurements from AlSi-alloys deformed at $Z<10^{12}$/s indicated formation controlled PSN activation (Kalu and Humphreys, (1986)). These observations indicate that during hot deformation the occurrence of PSN is limited due to a reduced formation of deformation zones. A general analysis of the effect of large particles

and their distribution on recrystallisation has recently been presented by Marthinsen *et al.* (2003).

Zener drag:

A dispersion of small second phase particles will exert a restraining force on a moving boundary, giving a retarding effect both on the migration of low and high angle boundaries during recovery, and high angle boundaries during recrystallisation. As first recognised by Zener and Smith, and as published by Smith (1948), the interaction force from a single incoherent spherical particle on a grain boundary is given by:

$$F_Z = 2\pi r\gamma_{GB}\cos\varphi\sin\varphi \tag{2.15}$$

where γ_{GB} is the grain boundary energy, r is the radius of the particle and φ is the angle at which the boundary meets the particle. This dragging force has its maximum value for $\varphi = 45^o$ and the maximum pull of one particle is then given by:

$$F_Z = \pi r\gamma_{GB} \tag{2.16}$$

Since a part of the moving boundary is removed when the boundary interacts with the particle, the system lowers its energy by the particle/boundary configuration. The boundary is hence attached to the particle, and bows out when it meets a particle. In a real metal, there is an array of particles, and the retarding pressure from this distribution of particles, commonly known as the Zener drag, was first estimated by Smith (1948) from a random distribution of particles to be:

$$P_Z = \alpha\gamma_{GB}\frac{f_v}{r} \tag{2.17}$$

where f_v is the volume fraction of particles of radius r and α is a geometric constant. A common value for α found in many textbooks [e.g. Humphreys and Hatherly (1995)] is α = 3/2. Thus, the effective driving pressure becomes $P=P_D-P_Z$. If the particle distribution is non-random, the effect on the microstructure might be quite different, as demonstrated by *e.g.* Nes *et al.* (1985) and Benum and Nes (1997).

The attachment of a grain boundary to an incoherent particle results in a reduction of energy W:

$$W = \pi \gamma_{GB} r^2 \tag{2.18}$$

However an often overlooked point is that Zener's approximation is valid for incoherent particles only, as in the case of Cr or Mn containing dispersoids. When the boundary impinges on coherent particles there must be an increase in the particle/matrix interfacial energy from a low value of $\gamma_{coherent}$ to a high value of $\gamma_{incoherent}$ in order for the boundary to pass [Doherty (1982)].

$$W' = 4\pi r^2 (\gamma_{incoherent} - \gamma_{coherent}) \tag{2.19}$$

This is the case if the operating mechanism makes coherent particles incoherent by the passing of a boundary. Therefore a permanent energy increase occurs after the boundary has passed the particle of W':

Usually $\gamma_{coherent}/\gamma_{incoherent} << 1$ and $\gamma_{incoherent} = \gamma_{GB}$.

$$W' \cong 4\pi r^2 \gamma_{GB} \tag{2.20}$$

The resulting equation for the Zener drag when a coherent particle becomes incoherent in response to a boundary passing these is:

$$P_Z = \frac{6\gamma_{GB} f_v}{r} \tag{2.21}$$

Compared with Eq. 2.14 with $\alpha = 3/2$, this suggests that coherent particles may be at least four times more effective than incoherent particles in preventing/retarding recrystallisation. However, a study by Nes et al. (1985) suggested that coherent particles may only be twice as effective in pinning grain boundaries as incoherent particles of the same size.

Zener drag is determined by a combination of particle radius, interparticle spacing and dispersoid volume fraction. In Zener's analysis the mean particle spacing, λ, relates to the size and volume fraction of the particle dispersion by equation 2.22 .

$$\lambda = r\left(\frac{4\pi}{3f_v}\right)^{\frac{1}{3}} \tag{2.22}$$

A maximum Zener drag is thus obtained for a high volume fraction of small particles, or in other words a high number density of closely spaced particles result in the most effective retardation of boundary migration. As seen from Eqs. 2.6 and 2.11 this also maximizes the critical nucleation size and/or particle size for nucleation of recrystallisation in the material and is just the condition needed to prevent or minimize the possibility of recrystallisation to occur, i.e. to provide the best possible recrystallisation resistance.

However, to maintain the recrystallisation resistance during further processing and/or high temperature exposure it is also important to avoid or minimize possible particle coarsening.

2.5.7 Particle coarsening

In order to reduce the total interfacial energy, a high density of small particles will tend to coarsen into a lower number density of larger particles during annealing. This will lead to an undesirable degradation of mechanical properties due to a reduction in the total Zener drag as explained in the previous chapter (Chapter 2.5.6). Particles usually coarsen by diffusion of solute (i) through the matrix or (ii) along the grain/subgrain boundaries, two situations that represent largely different diffusion conditions. As a consequence the kinetic relationships in these cases are quite different as well. In the following chapters the origin of particle coarsening and some general kinetics expressions for this process will be given. The influence of certain factors assumed to affect the coarsening rate will also be discussed.

The origin of particle coarsening

Greenwood (1956) first treated growth of precipitates by diffusion of solute in a matrix. The basic equations that form the beginning of the analyses are: (i) The Gibbs-Thomson equation for the concentration of solute in equilibrium with a particle of radius r:

$$C_r = C_e \exp\left(\frac{2\sigma V_m}{RTr}\right) \tag{2.23}$$

and (ii) Fick's law for the diffusion flux j:

$$j = -D\frac{\delta C}{\delta r} \tag{2.24}$$

where C_r is the concentration of solute at the particle/matrix interface in equilibrium with a particle of radius r, C_e is the solute concentration in equilibrium with a particle of infinite size, σ is the particle/matrix surface energy, V_m is the molar volume of solute, D is the diffusivity, T is the temperature and R is the universal gas constant (see also Chapter 2.6). It should be noted that the Gibbs-Thomson equation is based on ideal solution thermodynamics. However, from this equation it is easy to see that the solubility increases when the particle size decreases. A second particle with a small radius (and/or large curvature) has a higher molar free energy than a particle with a large radius (and/or) small curvature, and as a consequence there will be a driving force for the diffusion of solute from small particles to larger ones.

Coarsening theories

The theory of coarsening through the volume was further developed by Lifshitz and Slyozov (1961) and independently by Wagner (1961) (LSW-theory) to model the kinetics of precipitate growth from supersaturated solid solutions after the completion of nucleation. Classical coarsening theories involves the solution of three basic relationships: (i) A kinetic equation which gives the growth rate of an individual particle and may be derived from Equations 2.23 and 2.24, (ii) an equation of continuity which must be obeyed by the particle size and distribution and (iii) a conservation equation, which imposes a condition that the quantity of matter in a defined system remains constant (see Jayanth and Nash (1989)

for further details). By solving these relationships the following expression for the coarsening rate was derived in the LSW-theroy:

$$r^3 - r^3_0 = kt \qquad (2.25)$$

In this equation r is the mean radius at time t, r_0 is the mean radius at t=0 and k is a growth rate constant. However, this widely used relationship ignores several factors, which may influence the coarsening kinetics and lead to incorrect conclusions comparing theory and experiment. For instance the LSW-theory is strictly speaking only applicable when the second phase volume fraction, f_v, is very small. It is assumed in the theory that the mean distance between particle centres is large compared to the particle dimensions. When f_v increases, however, the mean separation between particles of a given size decreases, and the diffusion paths become shorter. As a consequence the coarsening rate would increase with increasing volume fraction. Ardell (1972) modified the LSW-theory to include this effect on the kinetics, i.e. the rate constant k was made sensitive to the volume fraction. It was concluded that even at very small volume fractions (f_v<0,01) there is a significant effect.

The rate of particle coarsening will also change drastically if the diffusion of solute occurs along grain/subgrain boundaries. This is a very likely mechanism if particles are located on the boundaries. Due to the more open diffusion path the activation energy for boundary diffusion, U_{GB}, will usually be lower than that for volume diffusion, U_v. At low temperatures $U_v << U_{GB}$ and even though the diffusion cross-section is much larger than for volume diffusion, the particles get most solute from grain boundaries. Furthermore, if we are dealing with slowly diffusing elements, boundary diffusion may dominate even at relatively high temperatures. Diffusion controlled coarsening on low angle boundaries and high angle boundaries has been the subject of many studies. Yang et al. (1992), Kirchner (1971) and Speight (1968) all found the coarsening to be of this form:

$$r^4 - r^4_0 = kt \qquad (2.26)$$

In a special case treated by Ardell (1972) an expression with an even higher exponent was derived. It was assumed that the precipitates were uniformly distributed on a dislocation network, similar to that often encountered at a low angle boundary. Under the assumption of pipe diffusion of solute to spherical particles only, it was concluded that when

the particle size and dislocation spacing are of the same order the exponent in equation 2.26 was equal to 5.

Loss of coherency/ semi coherency

When an Al_3X or Al_3 (X,Y) type of dispersoid grows, it will at a certain time reach a critical size where an interfacial dislocation at the Al/Al_3X interface would be more energetically favourable than increasing the matrix strain. A simple lattice approximation for the critical size can be derived from the lattice parameters, assuming that the critical size is reached when the misfit over the whole particle diameter equals the burgers vector of the Al matrix;

$$d_{crit} = b/\delta \tag{2.27}$$

where b is the burgers vector of Al and δ is the misfit between Al and Al_3X [Røyset and Ryum (2005)]. This value is found to be approximately 21,5 nm in diameter in Al-Al_3Sc at ambient temperatures. A smaller misfit between the dispersoid and the matrix, gives more stable dispersoids at elevated temperatures. However, when calculating these values the temperature dependency of the misfit δ must be taken into account. The effect of elements in solid solution must also be taken into account. As the temperature rises, more elements go into solid solution and thereby alter the lattice parameter [Røyset and Ryum (2005)]. Table 2.2 shows some lattice parameters for different trialuminides.

In Al-Sc alloys the loss of coherency during isothermal annealing has been reported to be accompanied by an increased average coarsening rate. The increased coarsening rate has been attributed either to diffusion of Sc along dislocation lines [Drits et al. (1982), (1984)] or to the increased particle/matrix interface energy of a semi coherent particle [Iwamura and Miura (2004)]. However, there are also several data sets in the literature that do not indicate an increased growth rate after the loss of coherency [Riddle and Sanders (2000)]

Table 2.2 Structure and lattice parameters for different trialuminids.

Phase	Equ. Structure	Lattice parameter [Å]	Reference
Al		a = 4,0496	Gscneider 1989
Al_3Sc	$L1_2$	a = 4,103 a = 4,103	Gscneider 1989 Harada 2002
Al_3Ti	DO_{22}	a = 3,854 a = 3,848	Harada 2000/2002 Villars 1985, Pearson
Al_3V	DO_{22}	a = 3,780 a = 3,780	Harada 2000/2002 Villars 1985, Pearson
Al_3Zr	DO_{23}	a = 4,009 a = 4,01	Harada 2000/2002 Villars 1985, Pearson
Al_3Y	DO_{19}	a = 6,276	Harada 2000/2002
Al_3Hf	DO_{23}	a = 3,988 a = 3,919	Harada 2000/2002 Villars 1985, Pearson
$Al_3(Sc_{0,75}Zr_{0,25})$	$L1_2$	a = 4,095	Harada 2000/2002
$Al_3(Sc_{0,5}Zr_{0,5})$	$L1_2$	a = 4,092	Harada 2000/2002
$Al_3(Sc_{0,25}Zr_{0,75})$	$L1_2$	a = 4,095	Harada 2000/2002
$Al_3(Sc_{0,9}Hf_{0,1})$	$L1_2$	a = 4,095	Harada 2000/2002
$Al_3(Sc_{0,75}Hf_{0,25})$	$L1_2$	a = 4,091	Harada 2000/2002
$Al_3(Sc_{0,5}Hf_{0,5})$	$L1_2$	a = 4,086	Harada 2000/2002

2.6 Diffusion

Diffusion is fundamental and ever-present in understanding the behavior of materials at elevated temperatures. Diffusion processes play a key role in the kinetics of many microstructural phenomena that occur during the processing of materials. Typical examples are nucleation of new phases, diffusive phase transformations, precipitation and dissolution of a second phase, recrystallisation, and high-temperature creep.

Migration of atoms in solid state may be described by Fick's 2. law for diffusion:

$$\frac{\partial C}{\partial t} = D \cdot \nabla^2 C \tag{2.28}$$

where D is the diffusion coefficient. The diffusion coefficient depends on the direction (x, y and z) of diffusion, the solute concentration and the temperature. However, it is usual to assume isotropic material and that D is independent of concentration as assumed in Eq 2.28. The diffusion coefficient may be expressed in terms of an Arrhenius relationship as:

$$D = D_0 \exp\left(-\frac{Q}{RT}\right) \tag{2.29}$$

where D_0 is the Pre-exponential constant, Q is the activation energy, T is the temperature and R is the universal gas constant. Table 2.3 show diffusion data for transition metals, while Figure 2.11 displays the different diffusion speeds put in an Arrhenius plot.

Table 2.3 Reported diffusion data for transition metals solutes in Al.

	Pre-exp., D_0 (m^2/s)	**Activation energy, Q (kJ/mol)**	**Temp. Range (°C)**	**References**
Al (self)	1,88 x10^{-5}	126	85-643	Madelung (90)
	1,71 x 10^{-4}	142	-	Brandes (83)
3d Transition Metals				
Cr	10,0	282	600-650	Rummel (95)
V	1,60	303	-	Bergner (77)
Fe	7,7 x 10^{-1}	221	450-658	Rummel (95)
Ti	1,12 x 10^{-1}	260	-	Bergner (77)
Mn	8,7 x 10^{-3}	208	470-655	Rummel (95)
Sc	5,31 x 10^{-4}	173	540-655	Fujikawa (97)
4d Transition Metals				
Zr	7,28 x 10^{-2}	242	530-640	Marumo (73)
5d Transition Metals				
Hf	1,2 x 10^{-2}	242	600-650	Minamino (87)

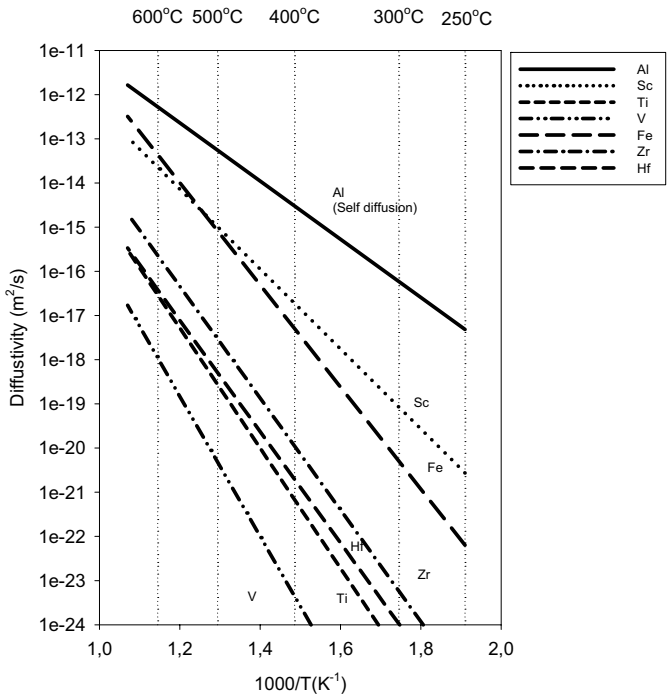

Figure 2.11 Diffusion speed of different transition elements in Al, from Table 2.3.

3 References

Ardell, A.J., Acta Metall., v20, p.601, 1972

Arjuna, A.R., Murty, B.S., Chakraborty, M., Materials Science and Technology, v13, pp.769-777, 1997

Benum, S., Nes, E., Acta Mat., 45, p. 4593, 1997

Beck, Sperry., J. Applied Phys., v21, p.150, 1950

Bergner, D., and van Chi, N., *Untersuchungen zur Diffusion von 3 d-Metallen in Al.* Wissenschaftliche Zeitschrift der Padagogischen Hochschule, 15(3), 1977

Blake, N., Hopkins, M.A., J. Mater. Sci., 20, pp.2861-2867, 1985

Boller, H., Nowotny, H., Wittman, A., Monatsh. Chem., 91, pp.1174-1184, 1960

Brandes, E.A., Smithells Metals Reference Book, Butterworths, 1983

Cahn., Proc. Phys. Soc. A (London)v60, p.136, 1950

Cristian, J.W., *" the theory of transformation in metals and alloys "*, 2nd edn, Pergamon Press Ltd, 1975

Doherty, R.D., Met. Sci., v16, p.1, 1982

Drits, M.E., Toropova, L.S., Bikov, U.G., Anastaseva, G.K., Proc. 'Diffusion in metals and alloys', Tihany, Hungary, pp.616–623, 1982

Drits, M.E., Ber, L.B., Bykov, G.Yu., Toropova, L.S. Anastaseva, G.K., Phys. Met. Metall., 57, (6), pp.118–126, 1984

Fink, W.L., and Willey, L.A., Trans. Met.Soc. AIME, 133, p.69, 1939

Forbord, B., Lefebvre, W,. Danoix, F., Hallem, H., Marthinsen, K., Scripta Mat., Vol.51, 4, p.333, 2004a

Forbord, B., Hallem, H., Marthinsen, K., ICAA-9, Brisbane, Australia, 1179-1185, 2004b

Fujikawa, S.I., Defect and Diffusion Forum, 143-147: pp.115-120, 1997

Furu, T., Marthinsen, K., Nes, E., Mat. Sci. Forum, 113-115, p.41, 1993

Gschneider, K.A.Jr., Calderwood, F.W., 10(1), pp.34-36, 1989

Greenwood, G.W., Acta Metall., v4, p.243, 1956

Hallem, H., Forbord, B., Marthinsen, K., Materials Science and Engineering A, Volumes 387-389, pp. 940-943, 2004

Hallem, H., Forbord, B., Marthinsen, K., ICAA9, Australia, pp.825-831, 2004b

Harada, Y., and Dunand, D.C., Acta Mater., 48, pp.3477-3487, 2000

Harada, Y., and Dunand, D.C., Materials Science and Engineering, A329-331, pp.686-695, 2002

Hori, S., Furushiro, N., Fujitani, W., Vol 30, No11, pp.617-625, 1980

Hu., Trans. AIME, v224, n75, 1962

Humphreys, F. J., Acta Met., 25, p.1323, 1977

Humphreys F. J., Acta Met., 27, p. 1801, 1979

Humphreys F. J., Kalu P. N., Acta Met., 35, p. 2815, 1987

Humphreys, F. J., and Hatherly, M., *Recrystallization and Related Annealing Phenomena*, Elsevier Science Ltd., Oxford ,1995

Hyland, R.W.Jr., Metall. Trans. A, 23A, pp.1947–1955, 1992

Iwamura, S., and Miura, Y., Acta Mater., 52, pp.591–600, 2004

Jayanth, C.S., Nash, P., J. Mat. Sci., 24, pp.3041-3052, 1989

Kalu, P. N., Humphreys, F. J., Proc. 7th Int. Risø Symp. on Metallu(Eds. Hansen et al.), Risø National Laboratory, Roskilde, p.385, 1986

Kharakterova, M. L., Eskin, D. G., Torpova, L. S., Acta metal. Mater, vol 42, No 7, pp.2285-2290, 1994

Kirchener, H.O.K., Met. Trans., 2, p.2861, 1971

Li., Appl. Phys., v33, n10, p.2958, 1962

Lifshitz, I., Slyozov, V., J. Phys. Chem. Solids, v19, p.35, 1961

Marthinsen, K., Daaland, O., Furu, T., Nes, E., Met. Mat. Trans., 34A, p.2705, 2003

Madelung, O., ed. *Landolt-Börnstein: Numerical Data and Functional Relationships in Science and Technology*. Diffusion in Solid Metals and Alloys, ed. H. Mehrer. Vol. 26., Springer-Verlag: Berlin, 1990

Marumo, T., Fujikawa, S., Hirano, K-I., J. Japan Inst. Light Metals. Vol. 23, no.1, pp.17-25. 1973

Minamino, Y., Yamane, T., Nakagawa, S., Araki, H., I., J. Jpn. Inst. Light Met. Vol. 37, no. 1, pp.72-82. 1987

McCartney, D.G., Int.Mat.Review., Vol. 34, No. 5, pp.247-260, 1989

Murray, J.L., McAlister, A.J., Kahan, D.J., J of Phase Equilibria Vol. 19, No 4, pp.376-380, 1998

Norman, A.F., and Tsakiropolous, P., Internat. J. Rapid Solidification, 6, pp.185-213, 1991

Norman, A.F., and Tsakiropolous, P., Internat. J. Rapid Solidification, 7,pp109-126, 1992

Norman, A.F., Pragnell, P.B., McEwen, R.S., Acta Mater, 46, pp.5715-5732, 1998

Nes, E. and Billdal, H., Acta Met., Pergamon Press, vol 25, pp.1039-1046, 1977

Nes, E., Proc 1st Int. Risø Symp. (eds. Hansen *et al*.), p.85, 1980

Nes, E., Ryum, N., Hunderi, O., Acta Met., 33, p.11, 1985

Nes, E., Prog. Mat Sci. 41, p.129, 1998

Porter, J., and Humphreys, F.J., Metal Sci, 13, p.83, 1979

Potzschanke, M., and Shubert, K., Z.Metall, 53, pp.548-561, 1962

Rajagopalan, P.K., Sharma, I.G., Krishnan, T.S., Journal of alloys and compounds, 285, pp.212-215, 1999

Rath, B.B., Mohantry, G.P., Mondolfo,L.F., J. Inst. Metals, 89, pp. 248-249, 1960

Read, W.T., Shockley, W., Phys. Rev., 78. pp.275-289, 1950

Reiso, O., Westengen, H., Auran, L., Aluminium, pp.186-189, 1980

Riddle, Y.W., and Sanders, T.H.Jr., Mater. Sci. Forum, Vols.331–337, pp.939–944, 2000

Riddle, Y.W., PhD thesis, Georgia Tech, GA, USA, 2000.

Riddle, Y.W., Hallem, H., Ryum, N., Mats.Sci.Forum, Vols.396-402, pp.563-568, 2002

Rummel, G., Zumkley, T., Eggermann, M., Freitag, K., Mehrer, H., Z. Metallkd. Vol. 86, no. 2, pp. 122-130, 1995

Ryum, N., Acta Met,v17, pp.269-278, 1969

Ryum, N., Journal of Material Science, 10, pp. 2075-2081, 1975

Røyset, J., and Ryum, N., Proc. 6th Int. Conf. on 'Aluminum alloys', Toyohashi, Japan, pp.793–798, 1998.

Røyset.J, Dr. Ing. Thesis, The Norwegian Institute of Technology, Trondheim, 2002.

Røyset, J., and Ryum, N., International Materials Reviews, v50, 2, pp.1-26, 2005

Røyset, J., and Ryum, N., Mater. Sci. Eng, A 396, pp.409-422, 2005b

Røyset, J., Private communication, 2005

Savitsky, E.M., Terehova, V.F., Burov, I.V., Naumakin, O.P., Proc. Fourth Conf. on Rare earth research, Phoenix, Arizona, USA, pp.409-420, 1964

Smith, C.S., Trans. Met. Soc. AIME, 175, p.15, 1948

Speight, M.V., Acta Metall, v16, p.133, 1968

Sæter, J.A., Forbord, B., Vatne, H.E., Nes, E., ICAA6, p.113, 1998

Tsyganova, I.A., Tylkina, M.A., Savitskiy, E.M., Izv.Akad. Nauk SSSR, Met.,1, pp.160-163, 1970

Tyvanchuk, A.T., Yanson, T.I., Kotur, B.Ya., Zarechnyuk, O.S., Kharakterova, M.L., Russ. Metall., 4, pp.190-192, 1988

Vatne, H.E., Furu, T., Ørsund, R., Nes, E., Acta Mater., vol44, p.4463, 1996

Vatne, H.E., Furu, T., Nes, E., ICAA6., vol44, p.1257, 1998

Villars, P., Calvert, L.D., *Pearson Handbook of Crystallographic Data for Intermetallic Phases*, ASM, Metal Park, OH, 1985

Wagner, C., Z.Elekrtochem, v65, p.581, 1961

Westengen, H., Reiso, O., Auran, L., Aluminium, 56, 12, pp.768-775, 1980

Zakharov, V.V., "Laws of the alloying of aluminium and aluminium alloys with scandium", Review of literature data, Moscow, 1994

Zakharov, V.V., Met. Sci. Heat Treat., 2, pp.61-66, 1997

Theoretical background

Yang, S.C., Higgins, G.T., Nash, P., Mats. Sci. Teck., v8, p.10, 1992

4 Experimental

4.1 Casting of alloys

4.1.1 Casting of Ø40 mm ingots

The alloys were produced by mixing appropriate amounts of Vigeland metal (99. 999% Al) and master alloys of Al-5wt%Hf, Al-10wt%Zr, Al-10wt%Si, Al-2wt%Sc and Fe pellets. The alloys were directionally solidified in order to reduce porosity and solidification contraction at the top, see Figure 7.1. A well stirred melt was poured at 760^{o}C into a cylindrical fibre tube mould (Ø 40 mm x150 mm) and cooled in the bottom by a large heat-extracting copper cylinder, see [Heiberg (2002)] for details. The method gives less pores and little shrinkage at the top of the ingot. The ratio between the weight of the copper-block and the weight of the casting is large enough (18kg / 0.5kg) to ensure a sufficiently high cooling rate. The cooling rate in the casting was measured by thermocouples 2 cm from the chill and varies between 9^{o}C/s to 5^{o}C/s, see Table 7.1. This is about the same as DC casting which has a cooling rate of about 5^{o}C/s-10^{o}C/s [Paramatmuni (2004), Lee et al. (2002)]. It should also be mentioned that no grain refiner was added during casting. The samples used in all the experiments were taken more than 2 cm from the bottom of the billet, as this region has a directionally solidified structure well suited for studies, i.e. no edge effects and a stable cooling rate.

4.1.2 Casting of Ø100 mm ingots

These alloys were produced as explained for the 40 mm ingots. However, the melt was poured at 760^{o}C into a cylindrical fibre tube mould (Ø100 mm x 200 mm, nominally) cooled at the bottom by a jet of water. The temperature was monitored by thermocouples during solidification. As a precaution a minimum of 10 mm from the top and 5 mm from the bottom of each billet were cut off and scrapped to avoid any edge effects and large differences in microstructure during subsequent thermo-mechanical processing, see Figure 4.1 and Appendix. The billets were finally cut in lengths of 150 mm.

4.1.3 Samples

Figures 4.1 and 4.2 show where the samples were taken out for further investigations. For the investigation of the Ø40 mmbillets, all samples were taken 2 cm from the bottom on all analysis. In the Ø100 mm billets, which were extruded, only the homogeneous region was used for further investigation.

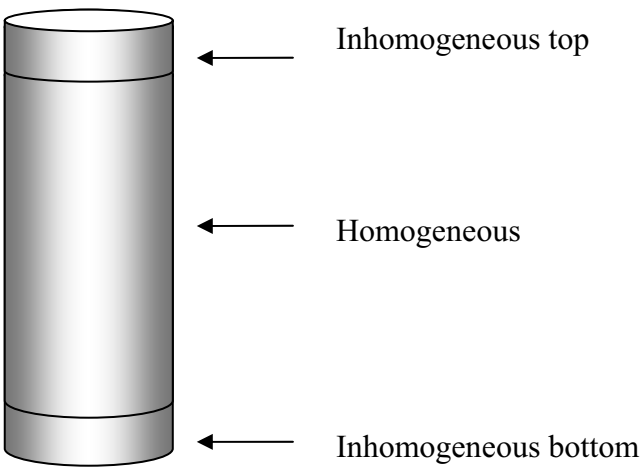

Figure 4.1 A schematic view of the billet indicating parts of the ingot with inhomogeneous structure, .i.e. at the top and at the bottom which were cut away.

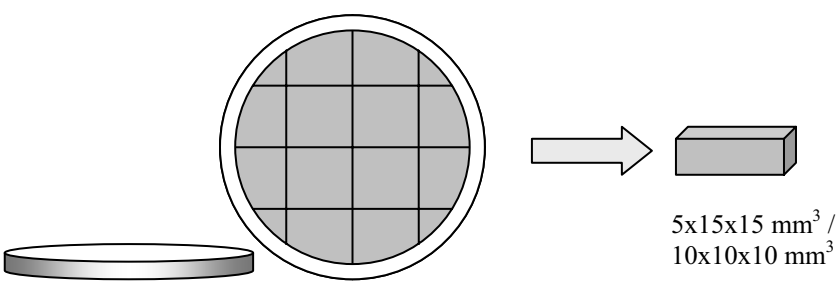

Figure 4.2 Disc cut from the billets in the homogeneous area for further investigations.

4.2 Alloy selection

Tables 4.1-4.5 show all the alloys used in these investigations. Chemical composition was measured as explained in Chapter 4.7.3.

Part A:

Table 4.1 Chemical composition of the Al-Hf alloys.

Alloy	Composition (wt% Hf)	Composition (at% Hf)
1	Al-0,17Hf	0,026
2	Al-0,77Hf	0,117
3	Al-0,82Hf	0,125
4	Al-0,95Hf	0,145

Table 4.2 Chemical composition of the Al-Hf-(Si)-(Fe) alloys.

Alloy	Composition (wt%)	Hf (wt%)	Si (wt%)	Fe (wt%)
5	Al-0,15Si	-	0,15	-
6	Al-1,0Si	-	1,0	-
7	Al-0,23Hf-0,19Si	0,23	0,19	-
8	Al-0,18Hf-1,1Si	0,18	1,1	-
9	Al-1,0Hf-0,15Si	1,0	0,15	-
10	Al-0,9Hf-1,0Si	0,9	1,0	-
11	Al-1,1Hf-0,11Fe	1,1	-	0,11
12	Al-0,95Hf-0,44Fe	0,95	-	0,44

Table 4.3 Chemical composition of the Al-Hf-(Sc)-(Zr) alloys.

Alloy	Composition	Hf (wt%)	Zr (wt%)	Sc (wt%)
13	Al-0,22Hf-0,11Zr	0,22	0,11	-
14	Al-1,0Hf-0,12Zr	1,00	0,12	-
15	Al-0,22Hf-0,15Sc	0,22	-	0,15
16	Al-1,1Hf-0,17Sc	1,10	-	0,17

Part B:

Table 4.4 Chemical composition of the Al-Hf-(Sc)-(Zr) alloys used in the Atom Probe investigations.

Alloy	Composition	Hf (wt%)	Zr (wt%)	Sc (wt%)
1	Al-0,43Hf-0,20Sc	0,43	-	0,20
2	Al-0,44Hf-0,22Sc-0,13Zr	0,44	0,13	0,22

Part C:

Table 4.5 Chemical composition of the alloys used in Part C.

Alloy	Composition	Hf	Sc	Zr	Si	Fe
1	Al-0,61Hf-0,14Si-0,15Fe	0,61	-	-	0,14	0,15
2	Al-0,46Hf-0,10Zr-0,13Si-0,19Fe	0,46	-	0,10	0,13	0,19
3	Al-0,52Hf-0,16Sc-0,16Si-0,21Fe	0,52	0,16	-	0,16	0,21
4	Al-0,51Hf-0,16Sc-0,06Zr-0,14Si-0,22Fe	0,51	0,16	0,06	0,14	0,22
5	Al-0,54Hf-0,17Sc-0,14Zr-0,16Si-0,18Fe	0,54	0,17	0,14	0,16	0,18
6	Al-0,18Sc-0,22Zr-0,16Si-0,23Fe	-	0,18	0,22	0,16	0,23

All given in wt%

4.3 Homogenisation

All alloys were homogenised in a Heraeus K750 air-circulating furnace for 5-20 hrs at 475°C. A heating rate of 50°C/hr was applied. An external reference thermocouple was used in order to monitor the temperature in the furnace during the heat treatment. The homogenisation procedure is shown in Figure 4.3.

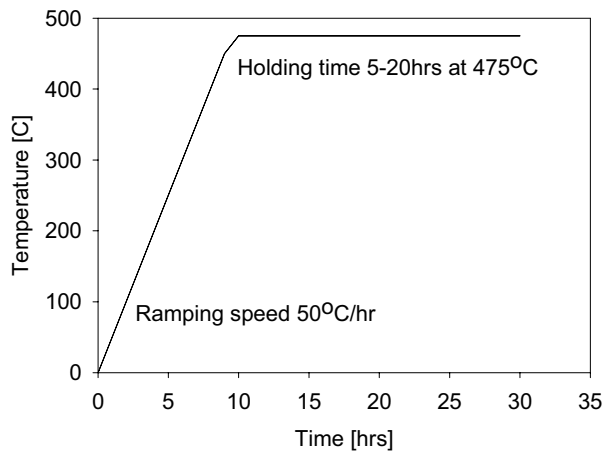

Figure 4.3 Graph exemplifying a homogenisation treatment

4.4 Cold deformation

Cold rolling in a laboratory rolling mill was performed in order to obtain a deformed material. These samples were used for subsequent investigations of annealing behaviour of the selected alloys and homogenisation conditions. Cold rolling was also used to simulate cold drawing after extrusion. The rolling have been carried out using heavy lubricated rolls and maximum roll velocity in order to obtain a microstructure similar to industrially rolled materials. Benum (1995) has previously shown that this procedure minimizes the shear zone in the surface regime of the sheet. The rolling slabs, cut from the ingots or the extruded profiles, were rotated 180° about the normal axis between each pass (as in a break down mill), and the degree of reduction at the first rolling passes was maximised to ensure a homogeneous through thickness deformation. To obtain a homogeneous deformation per pass the following equation has to be fulfilled:

$$\left(\frac{h_b}{4R_r a_r}\right)^{1/2}\left(2-a_r\right)<1 \qquad (4.1)$$

where $a_r = 1 - (h_a/h_b)$, h_a and h_b refers to the sheet thickness after and before a rolling pass, respectively. R_r is the radius of the rolls. Due to the limited force of the applied mill it has previously been reported that it is difficult to obtain a homogeneous deformation due to the small radius of the rolls (R_r=100mm) for sheet thicknesses larger than 15 mm (Furu, 1992). The temperature of the sheets was kept below 100^{o}C by applying water cooling.

4.5 Extrusion

Hot extrusion is a process in which a billet, enclosed in a container, is pushed through a shaped opening at an elevated temperature. As a result of the forming operation, the initial cross section area of the billets is reduced and a profile of solid or hollow cross section is produced.

The most important parameters in extrusion are the material properties, the forming temperature, T_{def}, the ram speed, V_{ram}, and the reduction ratio, R. All these factors will affect the ram load required to press the billet through the die. Figure 4.4 shows a typical variation of the ram load as a function of the displacement.

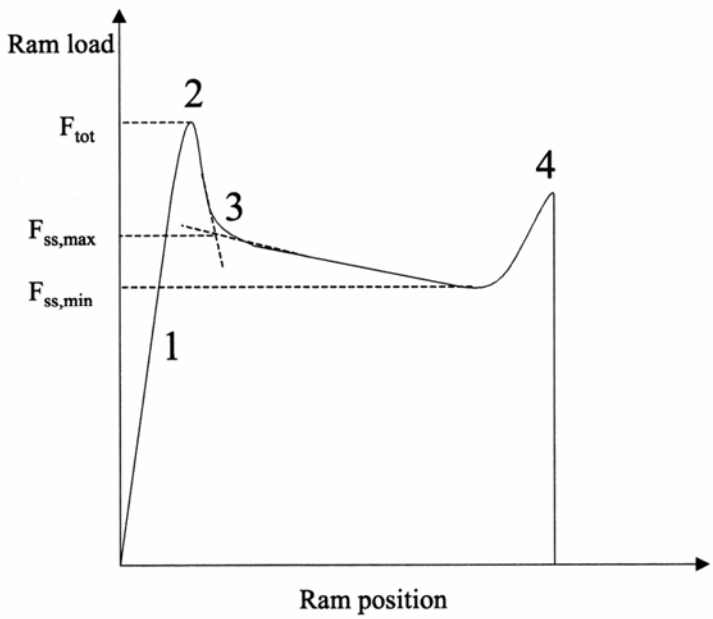

Figure 4.4 Schematic ram load versus ram displacement during direct hot extrusion.

Some relevant quantities are defined in Figure 4.4: F_{tot} is the maximum load, $F_{ss,max}$ is the maximum steady state load and $F_{ss,min}$ is the minimum steady state load. The curve can be divided into four stages. First the load increases rapidly as the billet fills the container (1). The load increases further to a peak value (2) before it drops to the maximum steady state load (3). Sheppard and Tutcher (1980) attributed this shape of the load curve to the formation of a deformation zone. They also investigated the microstructure of the billet in TEM and found that subgrain structure develops and grows "backwards" in the billet as the load passes through the peak. When the load drops and reaches the maximum steady state load (3) it was observed that a subgrain structure had developed through the entire billet. As the extrusion continues, the load decreases steadily due to reduced friction between the billet and the container wall. At the end, the

load increases (4) again due to radial material flow in the remaining billet, Laue and Stenger (1976).

The ingots used for extrusion were cut into extrusion billets of 150 mm in length, homogenised and extruded at SINTEF's 8 MN press. They were heated to the extrusion temperature (480^{o}C) within 5-6 min by an induction heater and then quickly transferred to the extrusion container. Profiles with dimensions 1.9 mm x 39.9 mm were extruded at a ram speed of 6 mm/s and water cooling was applied ~30 cm from the die outlet on the profiles. Thermocouples were used in order to monitor the profile temperature during extrusion. The ram force was also recorded continuously during extrusion, see Figure 22.7.

4.6 Annealing experiments

Annealing experiments using a slow and constant heating rate of 50ºC/h to the holding temperature were utilized to simulate commercial batch-annealing. The experiments were carried out in an air circulating furnace, enabling full control of the heating rate. For isothermal heating at high temperatures (500^{o}C-600^{o}C) salt baths were used. The thermal stability of these baths are better than +/- 2 ^{o}C and provided rapid upquenching. All samples were water quenched following annealing.

4.6.1 Characterisation of the annealing behaviour

Hardness – softening

Hardness measurements were utilized to study the softening reactions during annealing after deformation. Compared to tensile testing, this is a time effective and economical way to follow the softening reactions. Vickers hardness (VHN) was measured with a Matsuzawa DVK-1S instrument run at 1 Kgp loading, loading speed 100 μm/s and 15 s loading time. The hardness was determined as the average of at least 6 measurements, with a minimum of 3 indentations on each of the rolled surfaces.

Electrical conductivity - solute content and precipitation

High purity aluminium has an electrical conductivity of approximately 37.6 MS/m at room temperature (Kutner and Lang, 1976). The presence

of alloying elements in solid solution will, through their distortion of the atomic lattice, lower the conductivity of the material. On the other hand, if the alloying elements are in the form of semicoherent or incoherent precipitates, there is a much weaker effect on the conductivity. Hence, electrical conductivity measurements are a suitable way to obtain information about the elements in solid solution and the occurrence of precipitation reactions during annealing. Various elements in solid solution influence the conductivity to different degrees. By neglecting the temperature dependent term in the Matthiessens rule, the relationship between electrical conductivity and the solid solution content for the investigated alloys is given according to Althenpohl (1965) by:

$$\frac{1}{\kappa} = p = p_o + (p_X \times X_{ss}\,wt\%) \tag{4.2}$$

$$\frac{1}{\kappa} = 0.0267 + 0.020Sc_{ss}\% + 0.020Zr_{ss}\% + 0.032Fe_{ss}\% + 0.0068Si_{ss}\% + 0.0075Hf_{ss}\% \tag{4.3}$$

where κ is the electrical conductivity [MS/m], p is the total resistivity [μΩ*cm/wt%], p_o the resistivity of the base material (Al- 99,999wt%), p_x is the contribution from each alloying element in solid solution and Sc_{ss}%, Zr_{ss}% Fe_{ss}%, Si_{ss}% and Hf_{ss}% represent the weight percent of Sc, Zr, Fe, Si and Hf in solid solution, respectively. While reported p_x values exist for Sc, Zr, Fe and Si [Althenpol (1965), Dons et al. (1999, 2001)], the Hf value was found by experimental work (p_{Hf} ~ 0,0075), see Part A, Table 8.2. A more detailed description of solute effects is given in the literature, e.g. the review by Lok (2001).

In the present investigation the electrical conductivity was measured by a Sigmatest D2.068 at room temperature (20°C), measuring both sides in the ND direction, (see Figure 4.6) of the cold rolled or extruded specimens. Before measurements, the surface was grinded with 1200 mesh paper in order to get a smooth surface and to remove the oxide layer and possible remaining salt. The presented conductivity values are the average of 6 measurements on each sample. The minimum dimensions of the specimens were larger than 10 mm in diameter and 0.4 mm in thickness. With this experimental setup an accuracy of ±0.05 MS/m is usually achieved. It is however, important to emphasise that these measurements only give an estimate of the total solid solution content or

precipitation and it is impossible to separate the contributions from each of the various alloying elements. When calculating the amount of elements in solid solution from Eq.3, it was assumed that all of the Hf, Sc and Zr goes into solid solution (few or no Hf, Sc and Zr primary phases observed) and the Fe and Si amount were adjusted to the measurements, see Tables 8.3-8.6.

Tensile tests-strength evolution

Many material parameters can be measured by a simple tensile test, e.g yield stress, ultimate tensile strength, strain at fracture, E-modulus, anisotropy etc. In the present work the tensile specimens are only taken out parallel to the extrusion direction. An Instron 8032 servohydraulic test frame operating at 2 mm/min with a 25 mm extensometer was used for all tensile testing. The width and length of tensile specimens were 20 mm and 120 mm, respectively, see Figure 4.5. All specimens were strained until fracture occurred in accordance to the NS-EN 10 002-1 standard. An average of two stress strain curves was used to determine the parameters of the material. No large deviations were observed between any of these two parallel samples.

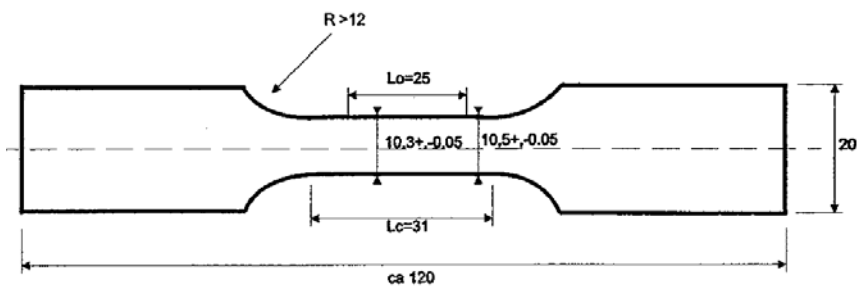

Figure 4.5 An illustration of a tensile specimen, with relevant dimensions in mm.

4.7 Microstructure characterisation

The microstructural characterisation has been carried out with the use of polarized light optical microscopy (LM), scanning electron microscopy (SEM), microprobe (Wavelength dispersive spectroscopy (WDS)), transmission electron microscopy (TEM) and field ion microscopy/atom probe (FIM/AP) In the following chapters a short introduction to these characterisation methods and the specimen preparation techniques for

each of them will be given. The specimen plane of investigation is named according to the directions given in Figure 4.6.

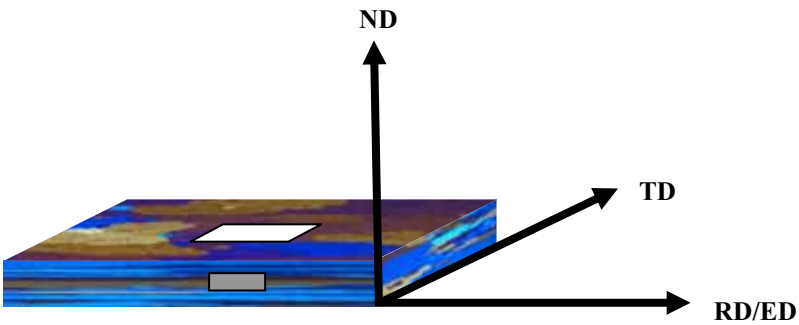

Figure 4.6 Illustration of a cold rolled or extruded specimen with the directions parallel to (RD/ED), normal to (ND) and transverse to (TD) the rolling or extrusion directions, respectively, indicated in the figure. The grey area indicates the plane where SEM-EBSD and grain size measurements by LM were performed (longitudinal transverse plane). The white area indicates the plane where grain hardness and electrical conductivity measurements and TEM imaging (normal plane) were performed.

4.7.1 Light microscopy (LM)

Compared to other techniques like SEM and TEM, the light optical microscope has a low resolution but provides a large field of view. It is also a relatively user friendly and time effective characterization tool. In the present work polarised light has been used to study deformed, partly- and fully recrystallised materials with respect to grain structure.

Specimen preparation was carried out by mechanical grinding and polishing down to 1μm. The samples were anodised at a voltage of 18V DC using an electrolyte consisting of 0,5 l of H_2O, 2,3 ml fluoboric acid and 3,5g boric acid (Bakers reagent), in order to reveal the grain structure under polarized light. Grain size measurements were then carried out using the linear intercept method, by averaging the grains measured in different directions.

4.7.2 Scanning electron microscopy (SEM)

In addition to giving a better resolution than the light optical microscope, the SEM may provide information about *e.g.* the chemical composition (Energy dispersive spectroscopy (EDS)) and the orientations of the crystals in the sample by electron back scattering diffraction (EBSD). In the present work a Hitachi S-4300SE field emission SEM (FESEM) equipped with a Schottky type field emission emitter was used to image and quantify the microstructures by EBSD. The FESEM gives excellent resolution and high beam brightness, making it suitable to study even heavily cold rolled structures with EBSD-orientation imaging mapping (OIM).

The EBSD-technique

The electron back-scatter diffraction (EBSD) technique, initially developed by Venables and Harland (1973) and further developed by *e.g.* Dingley (1984, 1988) and Hjelen (1990), has been utilized in the present investigation to characterize deformed and recrystallised structures mainly with respect to grain and subgrain sizes.

The principles of the EBSD-technique is as follows: When the electron beam hit a specimen in a single point, some of the electrons undergo elastic scattering with the atoms in the specimen, and a certain fraction of these electrons are diffracted according to Bragg's law on their way out of the specimen. Some of these back-scattered and diffracted electrons hit a phosphorus screen placed close to the specimen, creating a typical diffraction pattern that reflects the orientation of the crystal planes for that specific point. The pattern is imaged with a camera placed behind the phosphorus screen and a lead glass, and this image is transferred to a computer. The camera image may be further processed by removing the background noise due to inelastic scattered electrons. If the specimen is tilted ~70º then a larger fraction of back-scattered electrons escape the specimen and consequently a stronger signal is achieved.

The orientation of a specific grain or subgrain can be obtained from the EBSD-patterns by indexing of the displayed patterns. When running the indexing in an automated mode, the EBSD-pattern is detected automatically from the recorded image on the monitor, and a software package calculates the orientation of this position. Thousands of orientations can be recorded in this manner, and an orientation map

(OIM-map or EBSD-map) of the specimen is obtained. The orientation map may include information on crystal orientation and grain boundary character.

The TSL software, has been used to analyse the EBSD-patterns as well as for post processing of the data in the present work. EBSD has been used to measure subgrain sizes and grain sizes of the materials by the linear intercept method. Subgrain boundaries have been defined as being misoriented by 1.5º-15º, and high angle grain boundaries by misorientations >15º. A problem both with respect to the subgrain size and misorientation measurements is that boundary misorientations below 1.5º are excluded. This lower limit is selected, however, to avoid the orientation noise.

Specimen preparation for EBSD were performed by grinding the specimens mechanically down to 2400 Mesh followed by mechanical polishing at 3 μm and 1 μm. Electro polishing was then applied to remove the plastic deformation caused by the mechanical grinding and polishing, *i.e.* to reveal a flat and strain-free surface. The electro polishing setup was: -35ºC, 12 V for 120 s, in an electrolyte consisting of two parts methanol (CH_3OH) and one part nitric acid (HNO_3). The operating parameters for the FESEM and EBSD system have been summarized in Table 4.6.

Table 4.6 Normal setup for FESEM and software during EBSD-mapping.

EBSD software setup	
Software	TSL
Detector	Nordif Digital
Map size	50x80 μm
Detector binning	4x4
Step size	0.2 μm
Hough resolution	160
Subgrain B's	1.5º-15º
High angle GB's	15º>

FESEM-EBSD setup	
Microscope	Hitachi S-4300SE
Acc. voltage	20 kV
Emission current	2.0-2.5 nA
Working distance	22 mm

4.7.3 Wavelength dispersive spectroscopy (WDS)

A JEOL JXA-8900M microprobe equipped with WDS was used to determine the Hf, Sc, Zr, Fe and Si content of the alloys and to measure compositions across grains. Monte Carlo simulations determined an interaction volume of 2.14 mm in the actual materials. Thus a 2 mm probe spacing was used to ensure contiguous readings across the grain. All elemental profiles measured were first calibrated using known standards. There is currently no Al-Sc standard alloy available. Instead a pure Sc reference was used to calibrate the ZAF corrections (Atomic number, absorbsion and fluorescence) for WDS beforehand. The average of ten measurements was used to determine the compositional content of each alloy. The WDS was operated at 10keV and collected 10 seconds of peak then 10 seconds of background for quantitative analysis with a 50μm defocused beam for the compositional analyses.

4.7.4 Transmission electron microscopy (TEM)

A Jeol 2010 operated at 200keV was used for all the TEM work. TEM samples were prepared by electro thinning in 75% methanol / 25% nitric acid in a Struers Tenupol. A temperature of -25^{o}C and a voltage of 15V were used. EDS (Energy Dispersive Spectrometry) was used in order to investigate the chemical composition of the dispersoids. During the analyses a focused nano-beam (spot size 5-10 nm) was placed directly on the dispersoids. Analyses of the surrounding matrix were also performed in order to eliminate the matrix contribution to the dispersoid spectra.

A Gatan parallel EELS (Electron Energy Loss Spectroscopy) was used in order to measure the thickness of the TEM-foils. The thickness is needed for subsequent calcultations of dispersoid number densities and volume fractions and can be measured due to the fact that the inelastic scattering increases as the specimen thickness increases. Using an energy loss spectrum (see Figure 4.7), the thickness *t* can be calculated from the equation

$$t = \lambda \cdot \ln\left(\frac{I_T}{I_0}\right) \qquad (4.3)$$

where λ is the mean free path, I_0 is the intensity of zero-loss-peak (ZLP) and I_T is the total intensity of low-loss spectrum (<50eV). The zero loss peak (ZLP) is usually the most dominant feature of the spectrum and consists primarily of electrons that have completely retained the original beam energy. It is followed by plasmon peaks, whose number increases with t. Plasmons are longitudinal wave-like oscillations of weakly bound electrons. These oscillations are readily damped, typically having a lifetime of approximately 10^{-15} seconds.

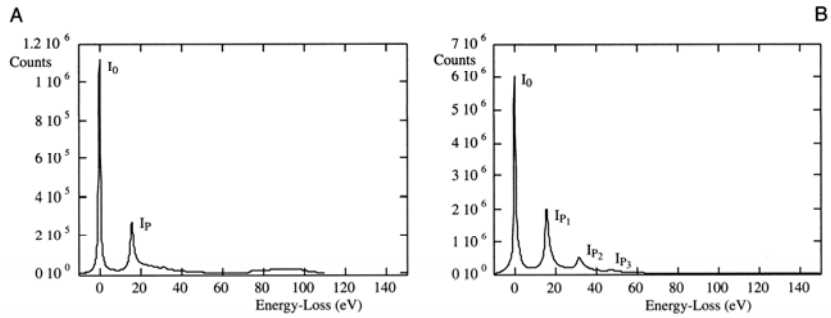

Figure 4.7 Graphs illustrating typical EELS spectra with plasmon peaks for two different thicknesses where the spectrum in B corresponds to a larger thickness than in A. (Williams and Carter (1996)).

Dispersoid measurements.

The dispersoid sizes, number densities and volume fractions were subsequently determined from dark field images analysed by the computer programs Adobe PhotoShop and ImageTool. Minimum 500-1000 dispersoids were measured/counted in each sample. In alloys where a heterogeneous dispersoid distribution was observed, maximum number densities were calculated.

Furthermore, it is also important to be aware of the source of errors which can appear during dispersoid volume fraction measurements; (i) error introduced with measuring foil thickness, (ii) small particles not resolved at the magnification used, (iii) overlapping particles and (iv) truncation errors when particles are at the foil surface.

4.7.5 Field Ion Microscopy and Atom Probe

Field Ion Microscopy (FIM) was introduced in 1951 by Erwin Müller, who had previously invented the Field Emission Microscope (FEM) in 1936. The field ion microscope is a type of microscope that can be used to image the arrangement of atoms at the surface of a sharp metal tip. In FIM, a sharp metal tip is produced and placed in a vacuum chamber, which is backfilled with an imaging gas such as helium or neon. The tip is cooled to cryogenic temperatures (<50 K). A positive voltage of 5000 to 10 000 volts is applied to the tip. Gas atoms adsorbed on the tip are ionized by the strong electric field in the vicinity of the tip (thus, "field ionization"), becoming positively charged and being repelled from the tip. The curvature of the surface near the tip causes a natural magnification – ions are repelled in a direction roughly perpendicular to the surface (a "point projection" effect). A detector is placed so as to collect these repelled ions; the image formed from all the collected ions can be of sufficient resolution to image individual atoms on the tip surface.

In 1967, Müller developed the first Atom Probe as a combination of a field ion microscope with a time-of-flight mass spectrometer. The atom probe is a point projection microscope capable of resolving the chemical identity and position of individual atoms in 3D with atomic resolution in the z direction and sub nanometer lateral resolution. The analytical information is obtained by counting, identifying and spatially locating individual atoms. As in FIM, a sharp tip is made and placed in vacuum at cryogenic temperature (50-80 K). A Positive pulsed voltage is applied, causing individual atoms at the surface of the tip to ionize and be repelled from the tip electrostatically. A fast timing circuit is used to measure the time taken between the pulse and the impact of the ion on a detector, thus allowing the mass-to-charge ratio of the ion to be calculated, and thus the element (or elements) of the ion. From the collection of many of these atoms, a 3D-volume of the sample can be made with relative position accuracy of less than one atomic spacing, from a probe size in the range of 1 to 5 nm. The basis of the 3DAP is shown on Figure 4.8. In this system, one or more evaporated ions hit the channel plate detector, giving time-of-flight information. The impact generates a flash of light on a phosphor screen. This light image is then detected with a CCD camera (charge-coupled device), leading to accurate position signals for each impact.

Three dimensional Atom Probe (3DAP) analyses in this research were carried out on an Energy Compensated Optical Tomographic Atom Probe (ECOTAP), developed in the University of Rouen [Bémont et al. 2003]. 0.3 x 0.3 x 20 mm^3 blanks were cut from ingots and prepared into needles by standard electropolishing in 10% perchloric acid (70%) in 2-butoxyethanol at 15 V at room temperature. Analyses were performed at 10^{-8} Pa, with a tip temperature of 80 K, a pulse fraction of 19% and a pulse repetition rate of 1.7 kHz. Data analyses were conducted using the software developed in the University of Rouen. Field Ion Microscopy (FIM) observations were performed in the vacuum chamber of the 3DAP at 20K under a 10^{-3}Pa pressure of He.

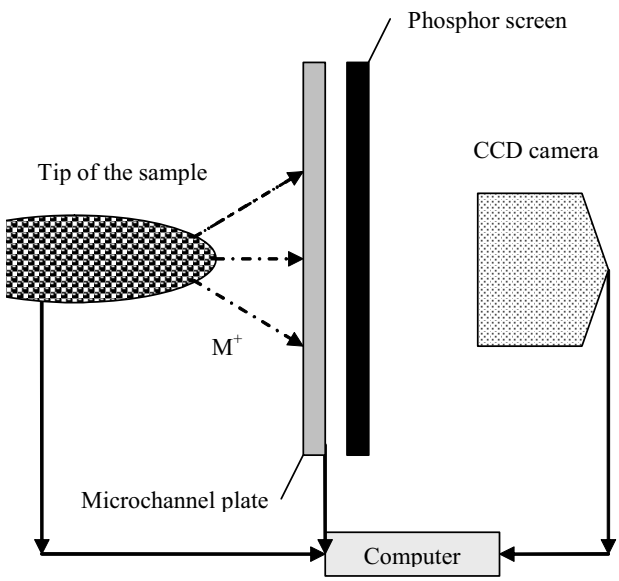

Figure 4.8 A schematic view of the principle in Atom probe.

5 References

Althenpohl, D., *Aluminium and Aluminiumlegierungen*, Springer-Verlag, p. 526, 1965

Bémont, E., Bostel, A., Bouet, M., Da Costa, G., Chambreland, S., Deconihout, B., Hono, K., Ultramicroscopy, 95, p.231, 2003

Benum, S., Dr. Ing. Thesis, The Norwegian Univ. of Sci. and Tech., Trondheim, 1995

Dingley, D. J., Scanning Electron Microscopy, 2, p. 569, 1984

Dingley, D. J., ICOTOM 8 (eds. Kallend and Gottstein), Warrendale, p. 187, 1988

Dons,A.L., Jensen,E.K., Langsrud,Y., Trømborg, E., Brusethaug, S., Metall. Trans. A, Vol. 30A, p.2135, 1999

Dons, A.L,, Journal of Light Metals, Vol. 1, p.133, 2001

Furu, T., Dr. Ing. Thesis, The Norwegian Institute of Technology, Trondheim, 1992

Heiberg, G., Dr. Ing. Thesis, The Norwegian Institute of Technology, Trondheim, 2002.

Hjelen, J., Dr. Scient. Thesis, The Norwegian Institute of Physics, Trondheim, 1990

Kutner, F., Lang, G., Aluminium, 52, p. 322, 1976

Laue, K. and Stenger, H., Extrusion: process, machinery, tooling, ASM, Metals Park, Ohio, 1976

Lee, P.D., Atwood, R.C., Dashwood, R.J., Nagaumi, H., Materials Science and Engineering, A328, pp.213-222, 2002

Lok, Z. J., *High Temperature Plastic Deformation and Related Solute Effects in Aluminium Based Alloys*, The Netherlands Inst. Met. Res., Delft, 2001

Paramatmuni, R.K., Chang, K-M., Kang, B.S., Liu, X., Materials Science and Engineering, A 379, pp.293–301, 2004

Sheppard, T. and Tutcher, M.G., Met. Sci., p.579, 1980

Venables, J. A., Harland, C. J., Phil. Mag., 27, p.1193, 1973

Williams, D.B., Barry Carter, C., *"Transmission Electron Microscopy"*, Plenum Press, New York, pp.653-685, 1996

Part A: Investigation of aluminium-hafnium alloys with additions of silicon, iron, scandium and zirconium.

Part A

6 Introduction Part A

In order to obtain the best possible recrystallisation resistance, it is beneficial to cast alloys which may give the highest possible level of elements like Hf, Zr and Sc in a supersaturated solid solution. During homogenisation these elements will precipitate as dispersoids, which in turn will stabilise the material during subsequent high temperature exposure. In practice the highest possible level of supersaturation is obtained by adding amounts slightly below the maximum solubility of the given elements in aluminium. This solubility limit should not be exceeded, as primary particles can have detrimental effects on the recrystallisation resistance.

Another unwanted microstructural feature related to high contents of for instance Zr is the formation of large columnar grains [McCartney (1989)], which may have unfavourable effects on the mechanical properties. It has been shown that Zr-additions above a critical level will lead to such grains in aluminium [Jones (1976)], and Hf/Sc may possibly have a similar effect. The critical levels are also expected to be influenced by other alloying additions due to altered phase stabilities (shift of lines/phase boundaries in the phase diagrams). The objective of the work presented in Part A has therefore been:

- To identify adequate levels of Zr, Sc, Fe and Si in Al-Hf-(Zr)-(Sc)-(Fe)-(Si)-alloys with respect to obtaining a cast structure with a high supersaturation of Hf, Zr and Sc and without columnar grains.
- To find an appropriate homogenisation procedure which optimize the desired precipitation behaviour.
- To make alloys with optimum recrystallisation resistance after cold rolling and annealing.

Accordingly, Part A has been divided into three main chapters. The chapter on cast structures (Chapter 8) presents systematic studies of adding different elements in turn and, in various amounts, to Al-Hf, and is consequently divided into three different sub-chapters:

- Binary Al-Hf-alloys, Chapter 8.1.
- Additions of Si and Fe to Al-Hf-alloys, Chapter 8.2.
- Additions of Sc and Zr to Al-Hf-alloys, Chapter 8.3.

In Chapters 9 and 10 the effect of different types of annealing as well as homogenisation of the alloys are discussed. These chapters also present cold rolling experiments and investigations of the recrystallisation behaviour of a selection of alloys.

The results obtained during this work presented in Part A served as basis for the production of Al-Hf alloys with various contents of Zr, Sc, Fe and Si which were investigated with respect to recrystallisation resistance during extrusion and post-extrusion annealing. The results of these investigations are presented in Part C.

7 Experimental

Casting: The alloys were made as explained in Chapter 4.1 The compositions were chosen to be lower than 1,2wt% Hf (c.f Figure 2.1) due to solubility limits. Table 7.1 show the cooling rate during solidification.

Table 7.1 Cooling rate at the bottom and the top of the casting billets for the Al-Hf alloys

Alloy (wt%)	Colling rate 2cm from chill	Colling rate 12cm from chill
1.Al-0,17Hf	9C/s	2C/s
2.Al-0,77Hf	5C/s	1C/s
3.Al-0,82Hf	6C/s	1C/s
4.Al-0,95Hf	7C/s	1C/s

Measuring point at the top is 12cm from the chill and measuring point for the bottom is 2cm from the chill.

Investigated alloys: the chemical compositions of the investigated alloys are given in Tables 7.2-7.4. WDS (Wavelength Dispersive Spectrometry) was used to determine the chemical composition. The alloys were also analysed by means of the line scan method with a continuous line for 100 μm. These results are presented in Figures 8.3-8.6. The alloys were analysed with respect to Si, Fe, Sc, Zr and Hf content. The chemical composition for the as-cast alloys has also been compared with the composition of alloys heated for 2 days at 550^{o}C (with the intention to even out the concentration gradients). For further details see Chapter 4.

Table 7.2 Chemical composition of the Al-Hf alloys.

Alloy	Composition (wt% Hf)	Composition (at% Hf)
1	Al-0,17Hf	0,026
2	Al-0,77Hf	0,117
3	Al-0,82Hf	0,125
4	Al-0,95Hf	0,145

Table 7.3 Chemical composition of the Al-Hf-(Si)-(Fe) alloys.

Alloy	Composition (wt%)	Hf (wt%)	Si (wt%)	Fe (wt%)
5	Al-0,15Si	-	0,15	-
6	Al-1,0Si	-	1,0	-
7	Al-0,23Hf-0,19Si	0,23	0,19	-
8	Al-0,18Hf-1,1Si	0,18	1,1	-
9	Al-1,0Hf-0,15Si	1,0	0,15	-
10	Al-0,9Hf-1,0Si	0,9	1,0	-
11	Al-1,1Hf-0,11Fe	1,1	-	0,11
12	Al-0,95Hf-0,44Fe	0,95	-	0,44

Table 7.4 Chemical composition of the Al-Hf-(Sc)-(Zr) alloys.

Alloy	Composition	Hf (wt%)	Zr (wt%)	Sc (wt%)
13	Al-0,22Hf-0,11Zr	0,22	0,11	-
14	Al-1,0Hf-0,12Zr	1,00	0,12	-
15	Al-0,22Hf-0,15Sc	0,22	-	0,15
16	Al-1,1Hf-0,17Sc	1,10	-	0,17

Macroetched samples of the directionally solidified Al-Hf alloys are shown in Figure 7.1. It is important to notice that the amount of cellular/equiaxed structure at the top of the castings increases with increasing Hf content. This is an effect of the higher enrichment of Hf in front of the solidification front, i.e. a higher degree of constitutional undercooling which in turn increases the probability of nucleating new grains. Another effect contributing to equiaxed growth is the progressive decrease in cooling rate towards the top of the ingot. However, the top of the ingot was not used in the investigations.

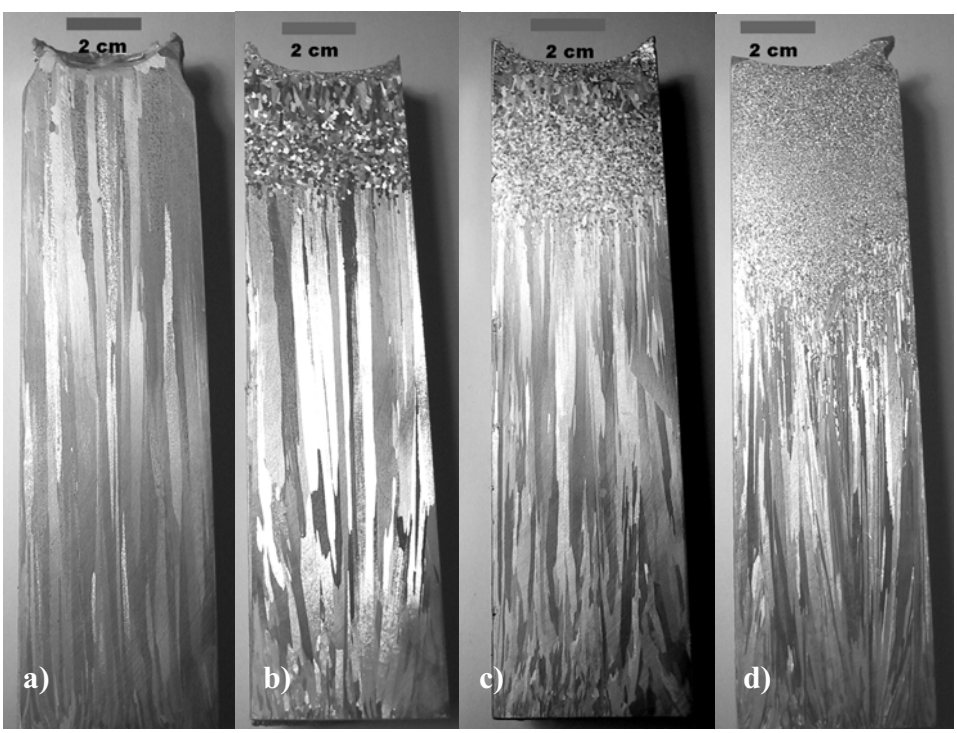

Figure 7.1 Macro etches of the as cast Al-Hf alloys, with directionally solidified grains at the bottom and with some equiaxed grains at the top of alloys b-d. The samples are cut vertically and etched with “Tuckers”. a) Al-0,17Hf, b) Al-0,77Hf, c) Al-0,82Hf, d) Al-0,95Hf.

Investigations of the cast structures: The cast structures were investigated by polarised light in an optical microscope. The grain size was measured with the line intercept method as explained in Chapter 4. The grain size was found to decrease with increasing alloying content, which is shown in Table 8.1. Furthermore, large variations in the grain sizes, which made it difficult to get good measurements and statistics, were observed. FESEM was used in order to study the presence of primary particles in the various alloys.

Hardness and conductivity: Vickers Hardness measurements were carried out in order to follow the softening reaction taking place during homogenisation and annealing after cold rolling (cf. Chapter 4.6.1).

Homogenisation: In order to find an adequate homogenisation temperature the alloys were first heated from room-temperature to 600˚C in an air-circulating furnace, continuous annealing, to investigate precipitation potential. From the results obtained the alloys were homogenised for 20hr at 475^{o}C, using a heating rate of 50^{o}C/hr to the holding temperature, before being quenched in cold water (~20˚C) (cf. Chapter 4.3).

Cold rolling and annealing: After homogenisation, some of the alloys were cold rolled 90% to a thickness of approximately 1.1 mm. In order to investigate the structural stability, i.e. the recrystallisation resistance, samples were cut from the cold rolled material and annealed (from RT) in an air-circulating furnace using a heating rate of 50ºC/hr. The samples were removed from the furnace at temperatures between 100ºC and 600ºC and subsequently quenched in water. This is referred to as continuous annealing later in the thesis (cf. Chapters 4.4 and 4.6).

TEM (Transmission Electron Microscope): The dispersoids were investigated by TEM. For further details see Chapter 4.7.4.

8 Casting of Al-Hf alloys with Si, Fe, Sc and Zr

8.1 Binary Al-Hf

Only a few publications exist in the literature dealing with cast structures of Aluminium-Hafnium alloys [Hori (1980), Norman (1991)]. However, in order to fully understand the formation and distribution of dispersoids in these alloys, it is important to understand the as cast microstructure. As already mentioned in the introduction to this chapter, one of the objectives of this work is to investigate effects of alloying additions on the cast structures. Both Hf-, Si-, Fe-, Sc- and Zr-contents were varied (Tables 7.2-7.4). The cast structures of the various alloys are presented below.

8.1.1 Cast structures in Al-Hf alloys

Morphology and grain size: Figures 8.1-8.2 shows that a morphology change is obtained when increasing the Hf-content in ND-direction. While an equiaxed structure is observed in Al-0,17Hf (Figure 8.1), the structure is somewhat different in Al-0.95Hf, where island grains and tendencies to the feather shaped pattern typical for twinned columnar grains (TCGs) are observed (Figure 8.2). In addition to the morphology change, a gradual refinement of the grain structure is observed when increasing the Hf-content. Table 8.1 shows that the grain size decreases from 917 μm to 475 μm when the Hf-content increases from 0.17wt% to 0.95wt%. The exception is the Al-0,82Hf alloy, which in fact displays a slight increase in grain size compared to Al-0.77Hf. However, this observation is probably due to the large variation in grain size (broad size distribution) as well as poor statistics (relatively few grains were measured for this condition).

The above results are in agreement with other investigations [Hori et al. (1980)], which have shown that the concentration of Hf in aluminium has to be higher than approximately ~3wt%Hf before obtaining any substantial grain refinement. At such Hf-contents, which in fact are considerably higher than the corresponding Sc-levels (~0.55wt%) needed to obtain considerable grain refinement in Al-Sc alloys [Norman (1998),

Røyset (2002)], primary Al_3Hf-particles form and act as nucleation sites for α-Al [Hori (1980), Norman (1991)]. However, at the Hf-levels investigated here, primary Al_3Hf-particles were, as expected, not observed. Only Al-0,95Hf contained a few primary Al_3Hf particles, but the number density of these particles were too low to give any significant grain refinement. These results indicate that practically all the added Hf enters in solid solution in the alloys investigated here.

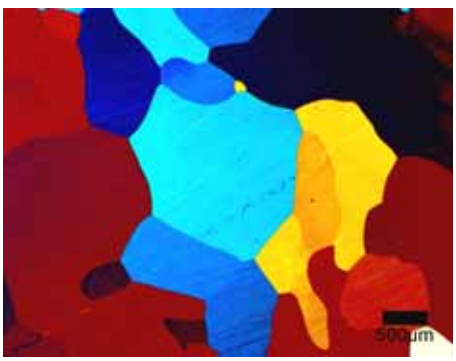

Figure 8.1 Anodised sample showing the equiaxed grain structure in Al-0,17Hf.

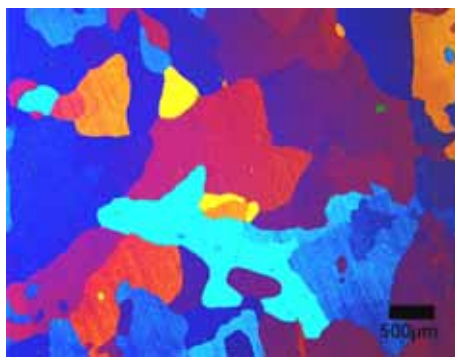

Figure 8.2 Anodised sample showing the grain structure in Al-0,95Hf

Table 8.1 Grain size measurements of the as cast alloys.

Alloy (wt%)	Grain size	Max size	Min size	Grains measured
Al-0,17Hf	917µm	1967µm	353µm	68
Al-0,77Hf	574µm	1645µm	335µm	115
Al-0,82Hf	628µm	1704µm	277µm	73
Al-0,95Hf	475µm	1679µm	218µm	111

The effect of Hf in solid solution on the conductivity: As almost all Hf is in solid solution in the present variants, the effect of Hf on the conductivity could be quantified, cf. Eq. 4.2 in Chapter 4.6.1. By using this equation p_{Hf} was found to be approximately 0.75 µΩ*cm/wt%, see Table 8.2. This value has subsequently been used to calculate the amount of Hf in solid solution in the Al-Hf alloys containing Si, Fe, Sc and Zr. It should be mentioned that different values have been reported used in the literature.

Table 8.2 Calculated p(Hf) values from conductivity measurements.

Alloy	Conductivity	Resistivity	p(Hf) calculated
Al-0,17Hf	35,81	2,79	0,71
Al-0,77Hf	30,74	3,25	0,75
Al-0,82Hf	30,54	3,27	0,73
Al-0,95Hf	29,15	3,43	0,80

p_o value used; 2,67 [Althenpol (1965)]. See Eq 4.2

8.1.2 Microsegregations in Al-Hf alloys

Segregation of alloying elements is expected to affect the dispersoid distribution after homogenisation, and line scans were consequently performed in the microprobe to investigate this aspect. The as cast segregation pattern is closely related to whether planar front-, cellular- or dendritic solidification takes place. Alloys with high purity solidifies with a planar front (no re-distribution of solute), and Figure 8.3 shows that this probably has been the case for Al-0.17Hf as no signs of cells or dendrites were detected. However, this is changed when increasing the Hf-content as shown for Al-0.82Hf alloy, see Figure 8.4.

In accordance with these observations, the segregation in Al-0.17Hf was relatively small, see Figure 8.5. On the other hand, relatively large concentration gradients, i.e. higher degrees of microsegregation, were observed in the Al-0,82Hf, see concentration profiles in Figure 8.6. Measurements were performed on as cast samples and samples annealed for two days at 550^{o}C. As expected from the peritectic solidification, the highest Hf-contents were found in the centre of the cells. The distance between the concentration maxima of the Al-0,82Hf specimen was about 20μm, which corresponds well to the cell size. No significant differences were observed between as cast samples and annealed.

Cell-structures like the ones observed here have also been found by Norman (1991) in Al-0,34Hf and Al-1,77Hf alloys, but in his case the cells were significantly smaller than the ones observed here. This can probably be related to the fact that Norman used a faster solidification rate.

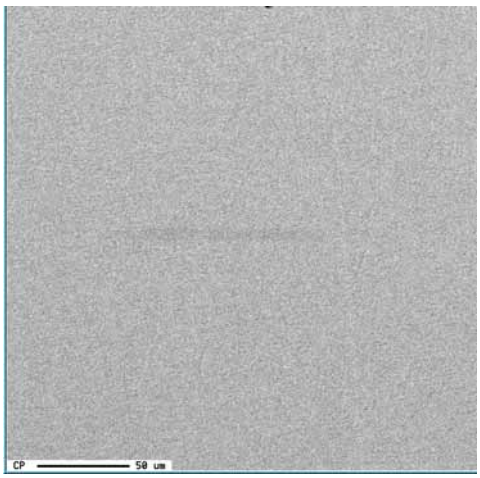

Figure 8.3 BE image of the scanned area taken in WDS from cross-section of Al-0,17Hf annealed at 550°C for 2 days (See also figure 8.5).

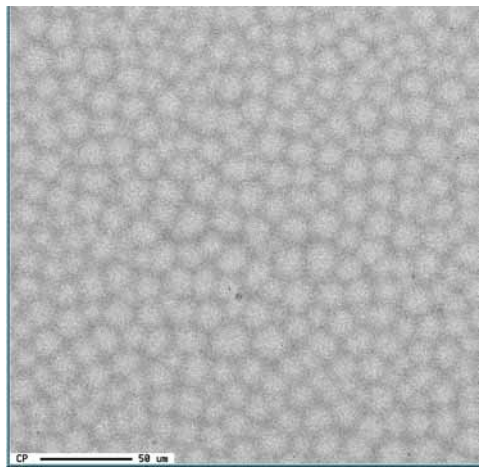

Figure 8.4 BE image from the scanned area taken in WDS from cross-section of Al-0,82Hf annealed at 550°C for 2 days (See also figure 8.6).

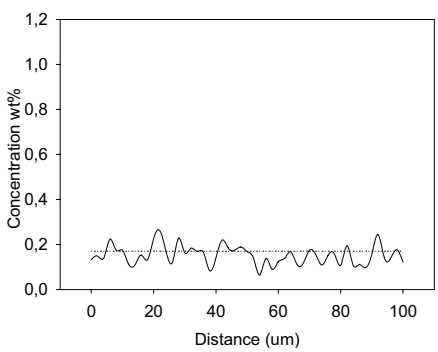

Figure 8.5 Chemical composition (wt% Hf) along a line-scan in Al-0,17Hf. Note small and random variations in the Hf concentration.

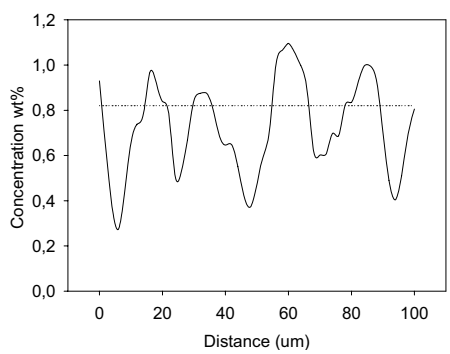

Figure 8.6 Chemical composition (wt% Hf) along a line-scan in Al-0,82Hf. Repeated concentration maxima for every ~20µm can be observed for the Hf concentration.

To summarise, based on the previous findings binary Al-Hf alloys with two different levels were chosen for further investigations; Al-(~0,20) wt%Hf and Al-(~1,0)wt%Hf. The alloy with low Hf content shows no cellular structure while the high Hf level alloy does show a cellular structure. The effect of a cellular structure upon precipitation should be subjected to further investigations.

The next step is to investigate to which extent additions of Si and Fe can or will affect the cast structure of alloys with the actual chosen levels of Hf. This aspect is discussed in chapter 8.2.

8.2 Addition of Si and Fe to Al-Hf

Based on the results in Chapter 8.1, the main objective of the present investigations was to study the effect of adding Si and Fe on the characteristics and properties of the as cast material, and later the effect on the precipitation behaviour and on the recrystallisation resistance, see Chapters 9 and 10. The alloys used are presented in Table 7.3.

In the Al-Zr system, similar dispersoids as in Al-Hf systems form, i.e. Al_3Zr. It has been found that these alloys should have Si-contents below a certain value in order to avoid the formation of coarse AlZrSi-particles, as these lead to a poorer recrystallisation resistance [Reiso et al. (1980)]. Si-additions below this value have actually turned out to promote precipitation. When it comes to iron, the low solubility of iron in aluminium imply that most of it is precipitated as so-called constituent phases i.e. Fe primarily forms phases with Al and the different alloying elements. These particles my also have an effect on the recrystallisation resistance.

All commercial alloys contain different amounts of silicon and iron, and the elements can in some cases deteriorate or improve the properties in the alloy. Typical values in 3xxx alloys are: 0,7wt%Fe, 0,5wt%Si (AA3103), in 6xxx: 0,1-0,3wt%Fe, 0,3-0,6wt%Si (AA6060) and in 7xxx 0,2wt% Fe, 0,15Siwt%Si (AA7175) [ASM Speciality Handbook (1994)].

8.2.1 Cast structures in Al-Hf-(Si)-(Fe) alloys

Morphology and conductivity: Micrographs of the anodised samples illustrating the grain structures in these alloys are shown in Figures 8.7-8.10 in ND-direction.

The alloys with low Si content, Al-0,23Hf-0,19Si and Al-1,0Hf-0,15Si, have little eutectic Al-Si phases after casting. However, even the alloys with high Si content, Al-0,18Hf-1,1Si and Al-0,9Hf-1,0Si, do not show more Si-eutectic/particles inside the grains or on the grain boundaries. Nevertheless, the grain size is significantly smaller, see Figure 8.10. There are only very few primary Hf particles in the Al-0,9Hf-1,0Si and in the Al-1,0Hf-0,15Si alloys after casting. Conductivity measurements have also confirmed that most of the elements are in solid solution, see Table 8.3-8.5. Both Al-Si and Al-Hf-Si have a dendritic structure inside the grains, while the binary Al-Hf alloys do not show any dendritic structure for levels below 0,95wt%Hf. This observation indicates that Si has a strong effect on the microstructure during solidification.

The Al-Hf-Fe casting showed an equiaxed dendritic structure, with large variations in grain size. The Al-0,95Hf-0,44Fe alloy has grains with a more tooth shaped structure than the low Fe content alloy Al-1,0Hf-0,11Fe.

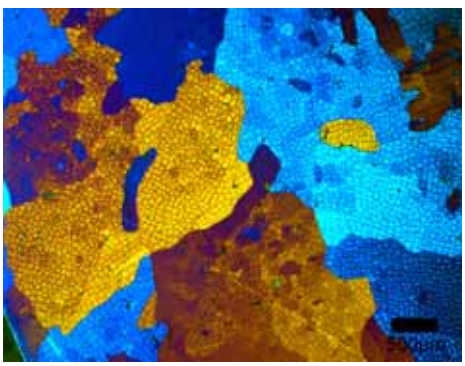

Figure 8.7 Anodised Al-0,23Hf-0,19Si sample as cast, showing equiaxed grains with a dendritic structure inside the grains.

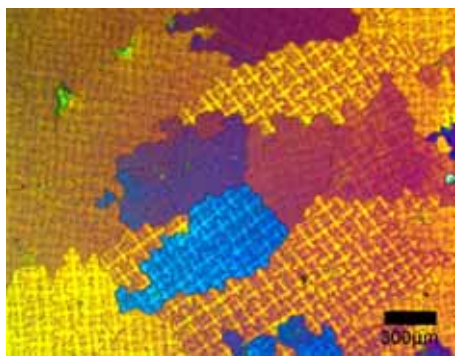

Figure 8.8 Anodised Al-0,18Hf-1,1Si sample as cast, showing equiaxed grains with a dendritic structure inside the grains.

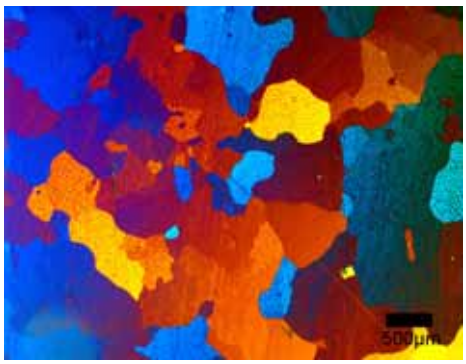

Figure 8.9 Anodised Al-1,0Hf-0,15Si sample, showing equiaxed grains.

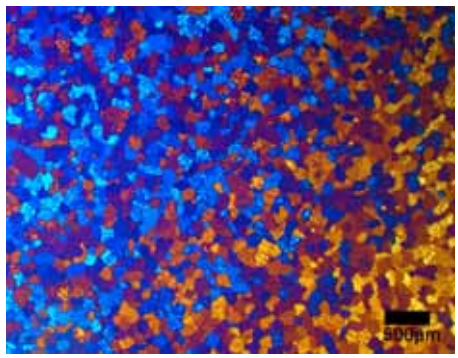

Figure 8.10 Anodised Al-0,9Hf-1,0Si sample showing equiaxed grains.

Table 8.3 Calculated amounts of elements in solid solution from conductivity measurements of the Al-Si alloys.

Alloy	Conductivity	Measured Resistivity	ss(Si)	Calculated Resistivity
Al-0,15Si	35,71	2,80	0,15	2,77
Al-1,0Si	31,84	3,14	0,60	3,08

ss: amount in wt% of the element in solid solution, see Eq 4.2 and 4.3.

Table 8.4 Calculated amounts of elements in solid solution from conductivity measurements of the Al-Hf-Si alloys.

Alloy	Conductivity	Measured Resistivity	ss(Hf)	ss(Si)	Calculated Resistivity
Al-0,23Hf-0,19Si	33,5	2,99	0,23	0,19	2,97
Al-0,18Hf-1,1Si	30,42	3,29	0,18	0,70	3,28
Al-1,0Hf-0,15Si	28,17	3,55	1,0	0,15	3,52
Al-0,9Hf-1,0Si	25,47	3,93	0,9	0,85	3,92

ss: amount in wt% of the element in solid solution, see Eq 4.2 and 4.3.

Table 8.5 Calculated amounts of elements in solid solution from conductivity measurements of the Al-Hf-Fe alloys.

Alloy	Conductivity	Measured Resistivity	ss(Hf)	ss(Fe)	Calculated Resistivity
Al-1,0Hf-0,11Fe	28,11	3,56	1,0	0,04	3,55
Al-0,95Hf-0,44Fe	28,30	3,53	0,95	0,05	3,54

ss: amount in wt% of the element in solid solution, see Eq 4.2 and 4.3.

From calculations by the solidification model ALSTRUC, a maximum solubility of 0,6wt% Si in Al-Si alloys is found [Dons et al.(1999), Dons (2001)]. Table 8.4 indicates that Hf and Si in combination increase the solubility of Si, since calculations show that actually ~0,85wt% Si can be dissolved. The solubility of Fe in Al is also increased from 0,02wt% (according to ALSTRUC) to 0,05wt% with addition of Hf, see Table 8.5. In the calculations it is assumed that all the Hf goes into solid solution, due to no or few primary Hf particles.

To summarise the investigations in Chapter 8.2, the addition of Si to the Al-Hf alloys gives a variation in grain size and morphology dependent on the amount of Si. When 0,20wt% is added, all Si is in solid solution, but when the Si level is increased, not all of it is dissolved after casting. Fe seems not to have any significant effect on the structure after casting. The next step is to investigate the effect of other elements like Sc and Zr, on the cast structure. This is discussed in Chapter 8.3.

8.3 Addition of Sc and Zr to Al-Hf

One of the objectives of this investigation was to study how the various additions of Sc and Zr influenced the as-cast microstructure of the Al-Hf alloys. The results and levels found in Chapter 8.1 was the basis for these investigations.

All elements in these alloys, Hf, Sc and Zr, form Al_3X-dispersoids (X=Hf, Sc, Zr) that potentially increase the recrystallisation resistance during high temperature annealing. However, one of the major drawbacks of using these elements is that they may lead to columnar grain structures as already mentioned. This may in turn affect the recrystallisation properties.

8.3.1 Cast structures in Al-Hf-(Sc)-(Zr) alloys

Figures 8.11-8.14 show that highly different microstructures, in ND direction, were obtained in these alloys. In the Al-0,22Hf-0,11Zr and Al-0,22Hf-0,15Sc alloys, i.e. the variants with a low Hf-content, a fairly equiaxed structure was observed. However, feather crystals or twinned

columnar grains (TCGs) were observed in the Al-1,0Hf-0,12Zr and Al-1,1Hf-0,17Sc alloys, i.e the high Hf-content alloys (see Figures. 8.15-8.16). TCGs are often termed feather crystals because of the feather shaped pattern observed on macro-etched sections, this is closer explained in Chapter 2.3.2.

Since little is known about TCGs and how they may affect the properties and behaviour of the alloy during further processing, alloys with TCGs are considered to be unwanted. Based on this consideration, casting experiments were performed to determine the amount of Hf which could be added before TCG formed. Three different alloys were made; Al-0,5wt%Hf-0,15Zr, Al-0,6wt%Hf-0,15Zr and Al-0,7wt%Hf-0,15Zr. No observations of TCGs were made in any of these alloys, so it was decided to keep the Hf level below 0,7wt% in alloys for further investigations. It is likely that a transition from an equiaxed structure to a structure containing TCGs exists for Al-Hf-Sc as well, but this has not yet been investigated.

TCGs have often been found to form in cases where the grain refinement has been poor [McCartney (1989)]. As no grain refiner was used during casting of the alloys, this is a likely reason for the TCG formation also for the present alloys. In the Al-1,0Hf-0,12Zr and Al-1,1Hf-0,17Sc alloys large amounts of primary particles were observed, while few of these were observed in the variants with a lower Hf-content. It is possible that the formation of TCGs in these alloys can be related to the presence of these particles, but a more thorough investigation is needed before a clear conclusion can be made.

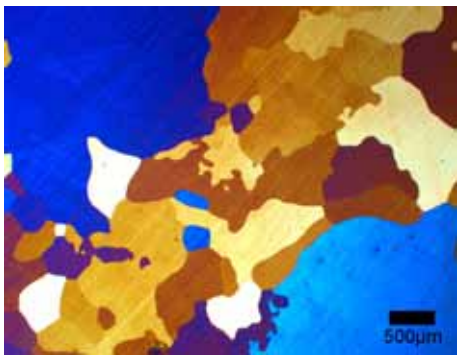

Figure 8.11 Anodised sample from the Al-0,22Hf-0,11Zr alloy, showing an equiaxed structure.

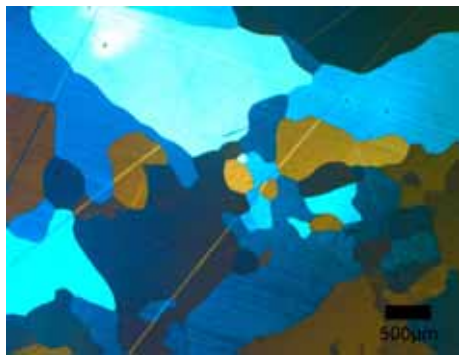

Figure 8.12 Anodised sample from the Al-0,22Hf-0,15Sc alloy, showing an equiaxed structure.

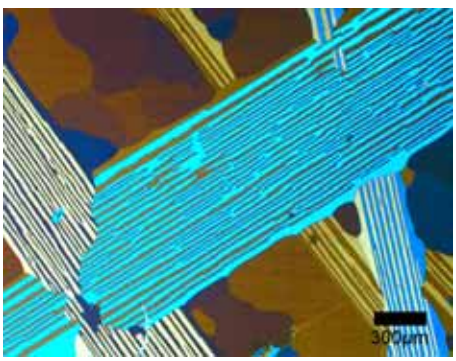

Figure 8.13 Anodised sample from the Al-1,1Hf-0,17Sc alloy, showing TCGs

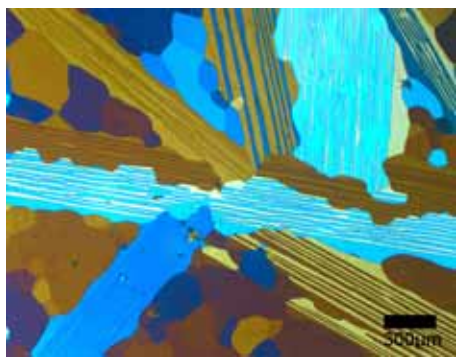

Figure 8.14 Anodised sample from the Al-1,0Hf-0,12Zr alloy, showing TCGs.

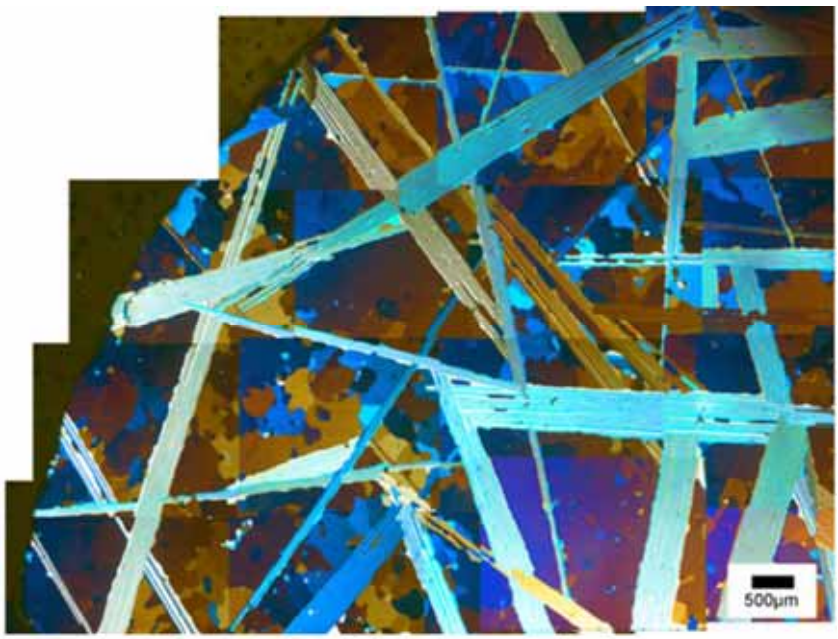

Figure 8.15 The Al-1,1Hf-0,17Sc alloy showing feather grains (TCG).

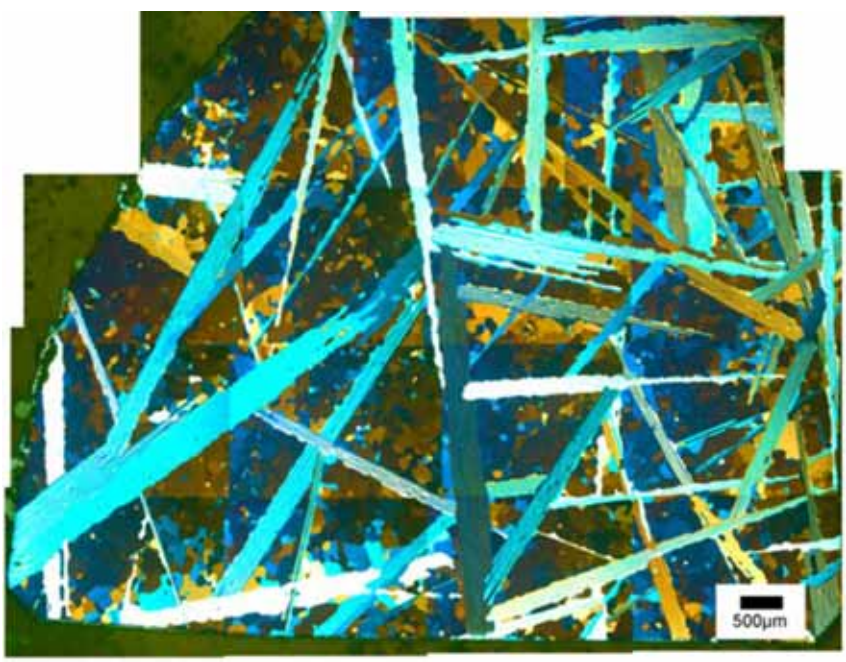

Figure 8.16 The Al-1,0Hf-0,12Zr alloy showing feather grains (TCG).

Table 8.6 gives the measured and calculated values of resistivity in the alloys, and from these results it seems that all the alloying elements go into solid solution. However, some primary particles were still observed during the investigations.

Table 8.6 Calculated amounts of elements in solid solution from conductivity measurements in Al-Hf-(Sc)-(Zr) alloys.

Alloy	**Conduc-tivity**	**Resis-tivity**	**ss(Hf)**	**Ss(Sc)**	**ss(Zr)**	**Calculated resistivity**
Al-0,22Hf-0,15Sc	31,20	3,21	0,22	0,15	-	3,14
Al-1,1Hf-0,17Sc	25,20	3,97	1,10	0,17	-	3,84
Al-0,22Hf-0,11Zr	32,54	3,07	0,22	-	0,11	3,06
Al-1,0Hf-0,12Zr	27,32	3,66	1,00	-	0,12	3,66

ss: amount in wt% of the element in solid solution, see Eq 4.2 and 4.3.

To summarise the results in chapter 8.3; the amount of alloying elements, Hf, Sc and Zr, must be carefully chosen to avoid TCGs. When these elements are used in combination it has been found that with a level of Hf less than 0,7wt% in Al-Hf-Zr alloys, TCGs are avoided.

9 Homogenisation investigations

As mentioned earlier, the literature shows that a heating rate of 50°C/hr up to temperatures around 450-475°C has been found suitable for these types of alloys. However, adequate holding times can vary for different alloys. In the present work, the Al-Hf-alloys given in Tables 7.2-7.4 have been investigated by annealing experiments in order to:

(i) Identify the types of dispersoids that form in these systems
(ii) Investigate how certain alloying additions influence the distribution of dispersoids
(iii) Obtain/confirm an adequate homogenisation treatment for these types of alloys

9.1 Binary Al-Hf alloys

Two different heat treatments were applied; (i) slow heating from room temperature to 550°C in order to investigate when precipitation occurs and to find an optimum homogenisation temperature (*9.1.1 Continuous annealing*), (ii) slow heating to the optimum homogenisation temperature in order to find a suitable holding time (*9.1.2 Slow heating followed by isothermal annealing*).

9.1.1 Continuous annealing

During the slow heating (50°C/hr) from room temperature, samples were removed at 50°C-intervals between 100°C and 550°C. 50°C/hr was used because this heating rate has turned out to be beneficial with respect to precipitation of Al_3Zr and Al_3Sc. Westengen et al. (1980) and Forbord et al. (2004a), have both shown that higher heating rates lead to lower Al_3Zr-densities or no dispersoid formation at all.

Conductivity and hardness results during annealing can be seen in Figures 9.1-9.2. These figures show that the conductivity is constant in the whole temperature interval, i.e. little or no precipitation takes place in the alloys. It should be mentioned, though, that coherent dispersoids will not give as

much response on the conductivity measurements as incoherent and large particles, as mentioned earlier in Chapter 4.6.1. However, both the hardness measurements and the investigations in TEM/FEG-SEM confirmed the low degree of precipitation. The hardness was found to be fairly constant between room temperature and 550^{o}C, while no or few dispersoids were detected in TEM. These results indicate that Hf-containing alloys may need other alloying elements like Si and Fe in order to increase the driving force and kinetics of Al_3Hf-precipitation [Hori et al. (1981)]. The presence of other alloying elements is in fact also a requirement for precipitation of Al_3Zr which in Zr-containing alloys has been shown by Reiso et al. (1980) and Forbord et al. (2004b).

Ryum (1975) investigated an Al-1,78wt%Hf alloy and he found continuous and discontinuous precipitation of Al_3Hf dispersoids after annealing of 50hr at 450^{o}C. But he also observed Fe and Al_3Hf particles, which can support the fact that Hf needs the presence of other elements to enhance the precipitation for this type of heat treatments. Norman et al. (1992) and Hori et al. (1980) also found Al_3Hf dispersoids, but Norman used longer annealing times at 400^{o}C.

In other works continuous and discontinuous precipitation has been observed, e.g. Norman (1991). In the present investigations, however, no discontinuous precipitation was observed. However, the low number of continuous precipitated dispersoids indicates that the driving force for precipitation is relatively low in this alloy. Murray et al. (1998) have redrawn data from investigations done by Rath et al.(1960), and according to their diagram the driving force for precipitation will be low at the temperatures and compositions used in the present investigation. Norman et al. also found continuous dispersoids in an Al-0,3wt%Hf alloy and discontinuous dispersoids only in an Al-1,08wt%Hf alloy. These observations seem to indicate that discontinuous precipitation occurs in alloys with a high Hf content.

Part A

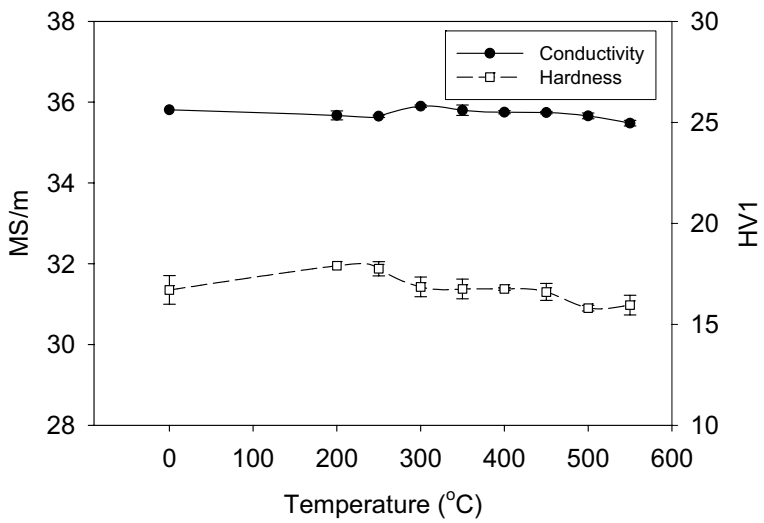

Figure 9.1 Continuous annealing of Al-0,17Hf, showing conductivity and microhardness at various temperatures.

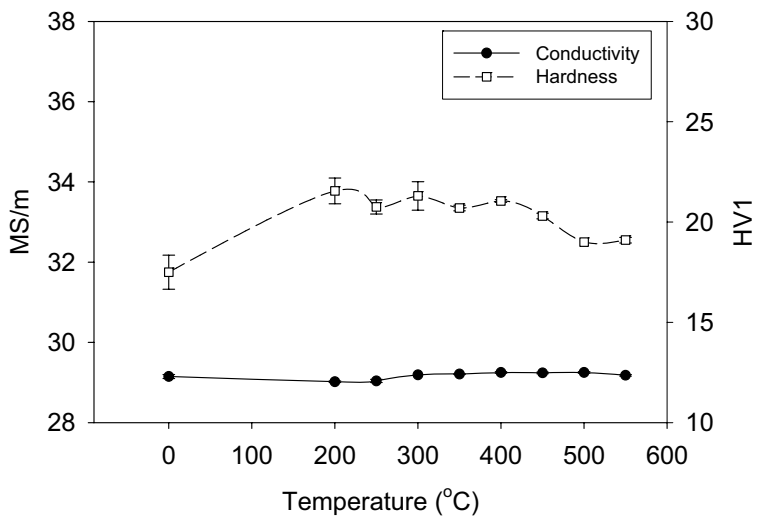

Figure 9.2 Continuous annealing of Al-0,95Hf, showing conductivity and microhardness at various temperatures.

9.1.2 Slow heating followed by isothermal annealing

During the slow heating (50°C/hr) from room temperature, samples were taken out at different times between 0 and 168hrs at 475°C. The objective was to study the effect of holding time at a chosen temperature on the different Al-Hf alloys.

During the investigation in TEM and FEG-SEM very few, if any, Al_3Hf-dispersoids were found even after annealing for 168hrs. Furthermore, the conductivity is almost constant, i.e. the small strengthening observed in Al-0,95Hf may possibly be due to natural variations (cf. Figures 9.3 and 9.4).

Because almost no particles were observed in these alloys, it is difficult to do any measurements that can give a characterisation of the particles.

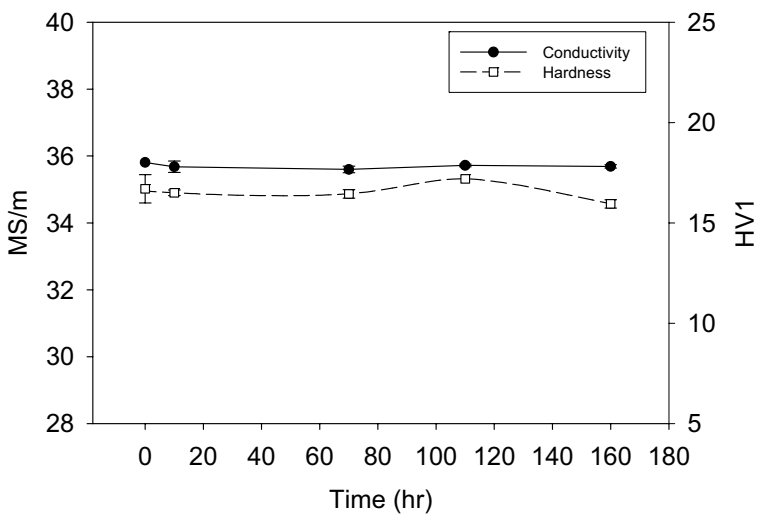

Figure 9.3 Isothermal annealing of Al-0,17Hf showing conductivity and microhardness at various holding times.

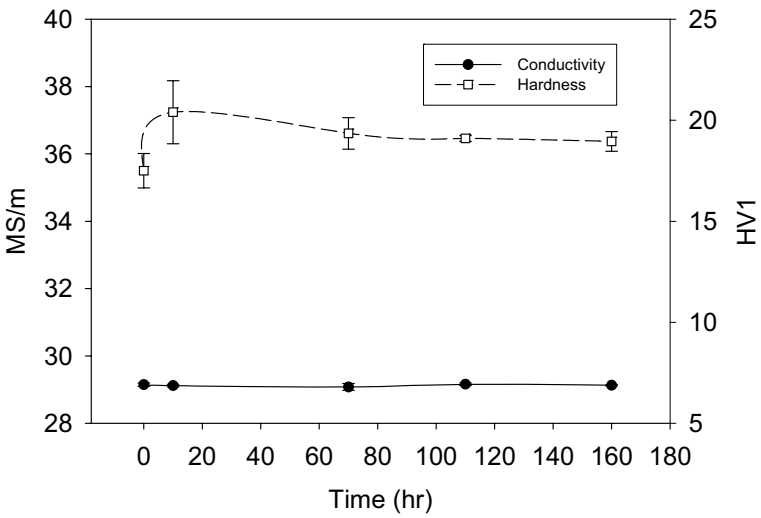

Figure 9.4 Isothermal annealing of Al-0,95Hf showing conductivity and microhardness at various holding times.

To summarise the results from this chapter; investigations of the binary Hf-alloys showed that no or little precipitation occurs during annealing. From these observations it is not possible to find an adequate homogenisation temperature and/or a useful holding time. Consequently, it is necessary to consider the other alloys with additions of e.g. Si and Fe where precipitation is enhanced to investigate this aspect further, see Chapter 9.2.

9.2 Al-Hf alloys with additions of Si and Fe

Two different heat treatments were applied; (i) slow heating from room temperature to 600°C in order to investigate when precipitation occurs and to find a optimum homogenisation time and temperature (*9.2.1 Continuous annealing*) (ii) homogenisation simulations of some alloys to investigate types of dispersoids formed and whether the time and temperatures used were suitable (*9.2.2 Homogenisation*).

9.2.1 Continuous annealing

From the continuous annealing of binary Al-Si alloys it is demonstrated that precipitation occurs around 300-350°C, as seen in Figure 9.5 and 9.6. The precipitates are Si particles. In the alloys containing ~0,2Hf and Si, it is clear that precipitation of Si is the dominating reaction as seen in Figure 9.7 and 9.8. However, when increasing the Hf level to ~1wt%, the Si peak is more suppressed, see Figures 9.9-9.10. The reason for a lower conductivity peak in the alloys with high Hf content may be the formation of more AlHfSi particles.

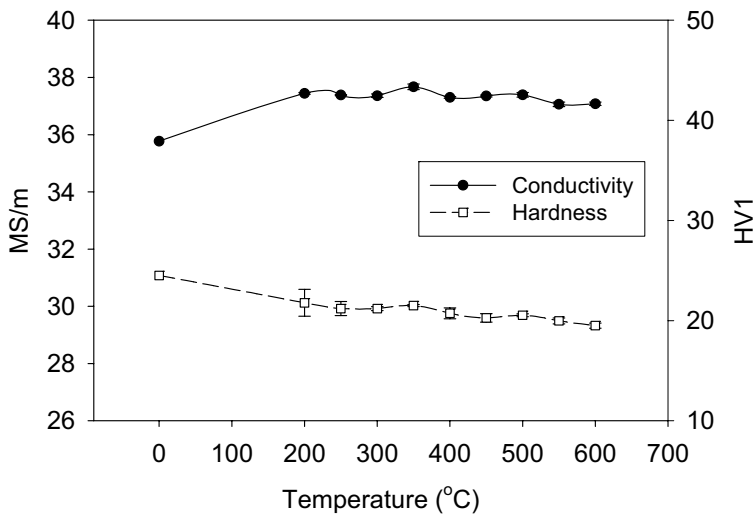

Figure 9.5 Continuous annealing of Al-0,15Si showing conductivity and micro hardness at various temperatures.

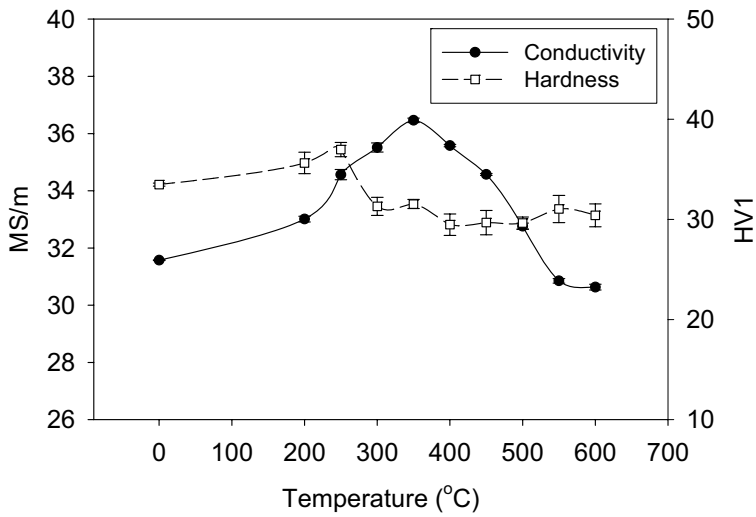

Figure 9.6 Continuous annealing of Al-1,0Si showing conductivity and microhardness at various temperatures.

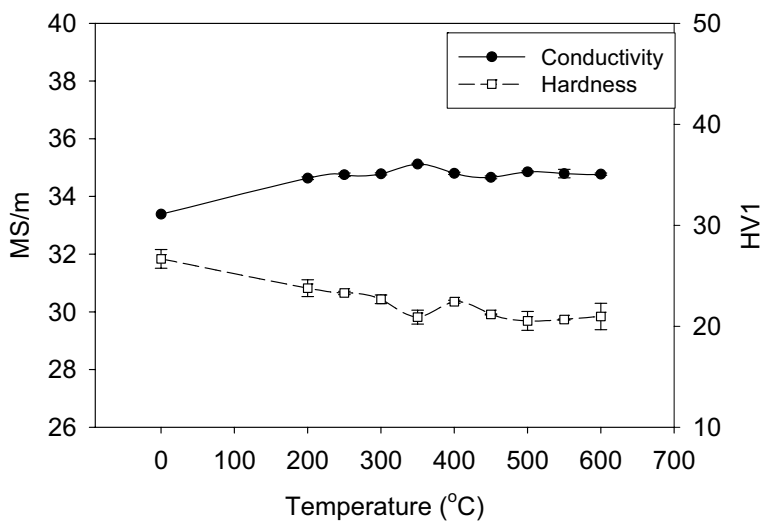

Figure 9.7 Continuous annealing of Al-0,2Hf-0,15Si showing conductivity and microhardness at various temperatures.

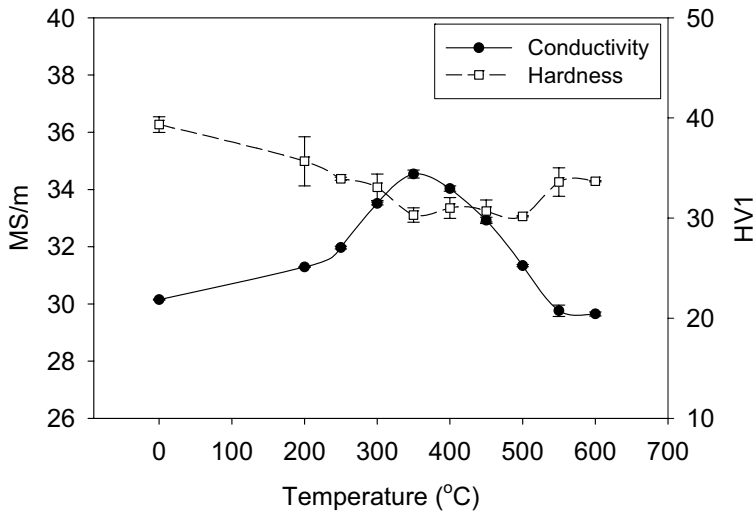

Figure 9.8 Continuous annealing of Al-0,2Hf-1,0Si showing conductivity and microhardness at various temperatures.

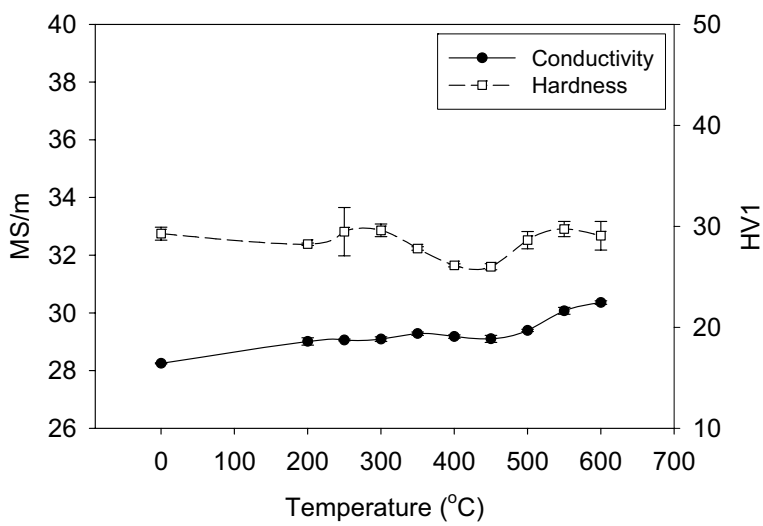

Figure 9.9 Continuous annealing of Al-1,0Hf-0,15Si showing conductivity and microhardness at various temperatures.

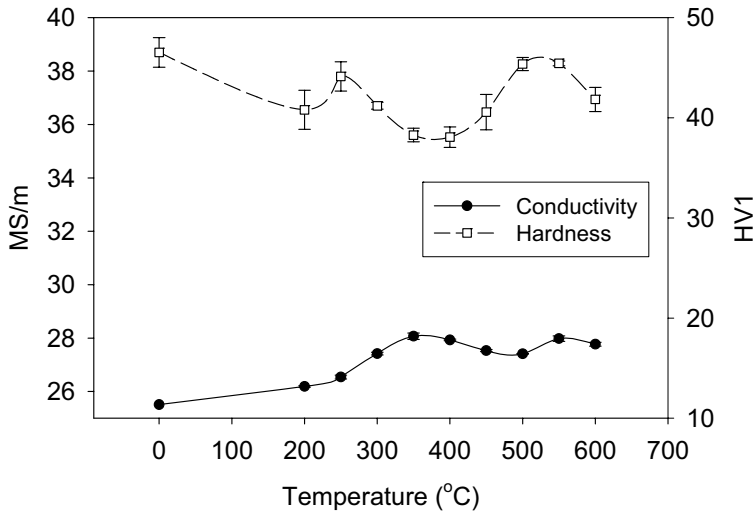

Figure 9.10 Continuous annealing of Al-0,9Hf-1,0Si showing conductivity and microhardness at various temperatures.

In the Al-Hf-Fe alloys spherical Al-Fe particles were found by SEM. The particles were positioned on the boundaries in the cell-structure. In Figure 9.11, binary Al-Hf alloys are compared with ternary Al-Hf-Fe alloys. This figure shows that Fe can enhance the precipitation, but the amount of Fe; 0,11wt% or 0,44wt%, does not influence the precipitation to any large extent. From Figure 9.11 only small variations in the Al-Hf-Fe curves can be seen, i.e. no or very little precipitation.

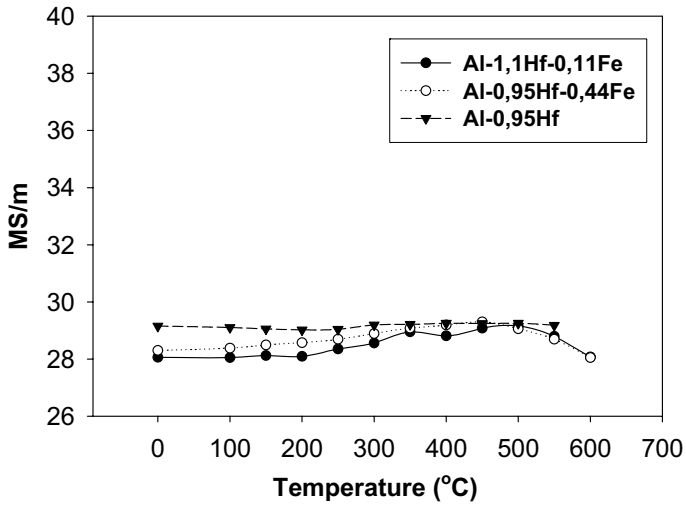

Figure 9.11 Continuous annealing of Al-Hf-Fe showing conductivity at various temperatures.

9.2.2 Homogenisation of the alloys

The homogenisation time was chosen to be 20 hrs since Si seems to precipitate early, while Hf still needs time to diffuse and form dispersoids. Some alloys where ramped 50°C/hr and held at 475°C for 20hrs as a homogenisation procedure. This time and temperature was chosen based on experience with these types of alloys and results from other investigations [Westengen et al. (1980), Riddle et al. (2002)]

TEM pictures from the homogenised condition illustrate the microstructures. Figures 9.12-9.15 show the Al_3Hf dispersoids and the AlHfSi particles which form in the matrix. The distribution of dispersoids is heterogeneous. With increasing Si level the AlHfSi particles increase in number and size. It is worth noticing that the magnification is different in the different figures.

In the Al-Hf-Si alloys continuous precipitation of Al_3Hf occurs. These precipitates are fully coherent with the matrix and have a spherical shape.

The average radius after homogenisation is approximately 15 nm, see Figures 9.12. This observation indicates that the Si-addition increases the driving force for precipitation, even though the higher Hf-content in this alloy may also contribute to more precipitation. It should also be noted that the dispersoids are heterogeneously distributed, see Figure 9.13.

Relatively coarse and inhomogeneous AlHfSi particles with more elongated shapes also form in this alloy, see Figure 9.13. A negative consequence of the formation of AlHfSi particles is that less Hf will be available for the formation of the small, coherent and spherical Al_3Hf dispersoids, which more efficiently may prevent recrystallisation from taking place. Hori et al. (1981) have shown that an increasing Si content will lead to more AlHfSi-formation and the Si-content should therefore not be too high. However, the results clearly indicate that some Si is necessary in order to promote continuous precipitation of spherical Al_3Hf-dispersoids during homogenisation. These results are in accordance with observations in Al-Zr-alloys. Westengen et al. (1980) annealed an Al-0,2Zr alloy and an Al-0,2Zr-0,12Si alloy isothermally at 350^{o}C. While the hardening response was similar for both alloys, maximum hardness was obtained far earlier in the Si-containing alloy, i.e the Si-addition increased the precipitation rate of the metastable and coherent Al_3Zr-dispersoids. Still, the amount of Al_3Hf dispersoids is possibly too low as far as it concerns the recrystallisation resistance at high temperatures, see also Chapter 10.1. As a consequence it was decided that Sc and Zr which may further enhance the precipitation should be added to the Al-Hf alloys. This is further discussed in Chapter 9.3.

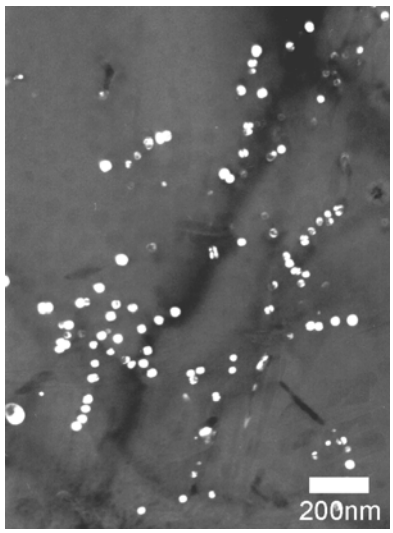

Figure 9.12 Dark field TEM-image showing Al_3Hf dispersoids in homogenised Al-1,0Hf-0,15Si.

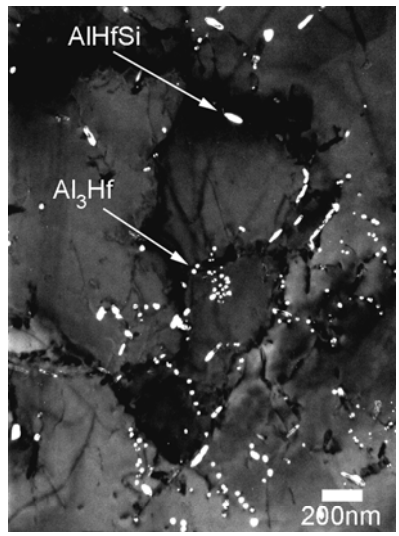

Figure 9.13 Dark field TEM-image showing Al_3Hf dispersoids and AlHfSi particles in homogenised Al-1,0Hf – 0,15Si

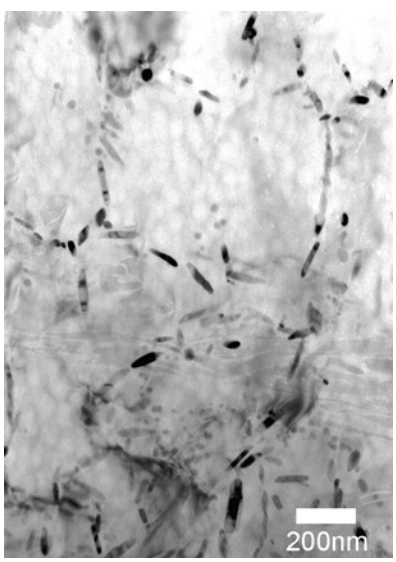

Figure 9.14 Bright field TEM-image showing AlHfSi particles and some Al_3Hf dispersoids seen faintly in the background in homogenised Al-1,0Hf –0,15Si.

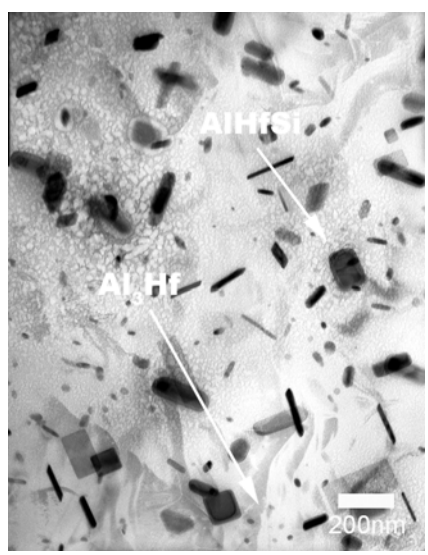

Figure 9.15 Bright field TEM-image showing AlHfSi phases and some Al_3Hf dispersoids seen faintly in the background in homogenised Al-0,9Hf –1,0Si.

9.3 Al-Hf with additions of Sc and Zr

The Al-Hf alloys with additions of Sc and Zr were subjected to slow heating rate (50°C/hr) from room temperature to 600°C in order to investigate when precipitation occurs and to find an adequate homogenisation procedure for these alloys (*9.3.1 Continuous annealing*).

9.3.1 Continuous annealing

Figures 9.16, 9.19 and 9.20 shows that precipitation in alloys containing Sc starts at ~250°C, and the formation of these particles is accompanied by a significant increase in strength which reaches a maximum at ~350°C. However, a maximum conductivity was obtained at 450-500°C. A homogenisation temperature of 475°C was therefore considered to be adequate for later investigations. In the alloys containing only Hf and Zr no clear hardness or conductivity peak was observed, which indicate that Sc controls the early precipitation stage (see also Part B).

In the Al-Hf-Zr-alloys the changes in both hardness and conductivity were relatively small (Figures 9.17 and 9.18). This is in accordance with the TEM-observations, which have shown that few and relatively coarse Al_3(Hf,Zr)-dispersoids formed in the Al-0,22Hf-0,11Zr alloy, while a heterogeneous distribution of these particles was found in the Al-1,0Hf-0,12Zr alloy. This observation explains the small hardness increase in this alloy compared to Al-0,22Hf-0,11Zr. However, the dispersoid number and density in the Al-1,0Hf-0,12Zr alloy was far less than what was observed in the Al-0,22Hf-0,15Sc and Al-1,1Hf-0,17Sc alloys. The slight increase in Al-1,0Hf-0,12Zr took place between 400°C and 550°C, and in order to compare directly with the Al-Hf-Sc-variants, 475°C was chosen as the homogenisation temperature also for further investigations of the Al-Hf-Zr-alloys.

Part A

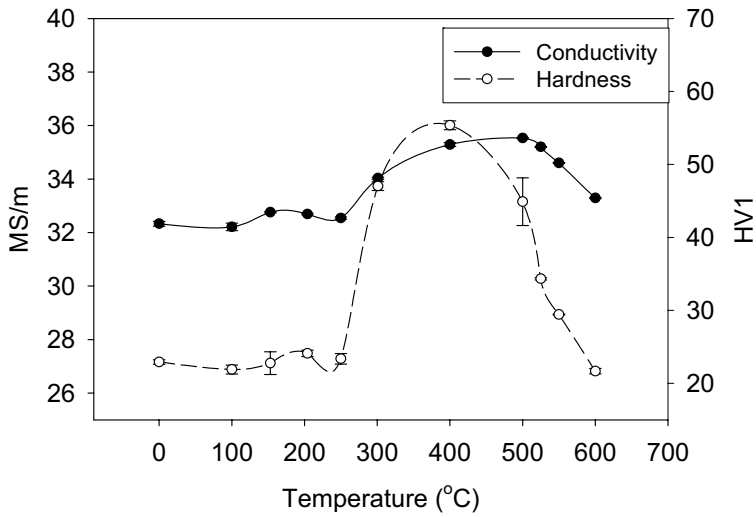

Figure 9.16 Continuous annealing of Al-0,2Sc-0,15Zr showing conductivity and microhardness at various temperatures.

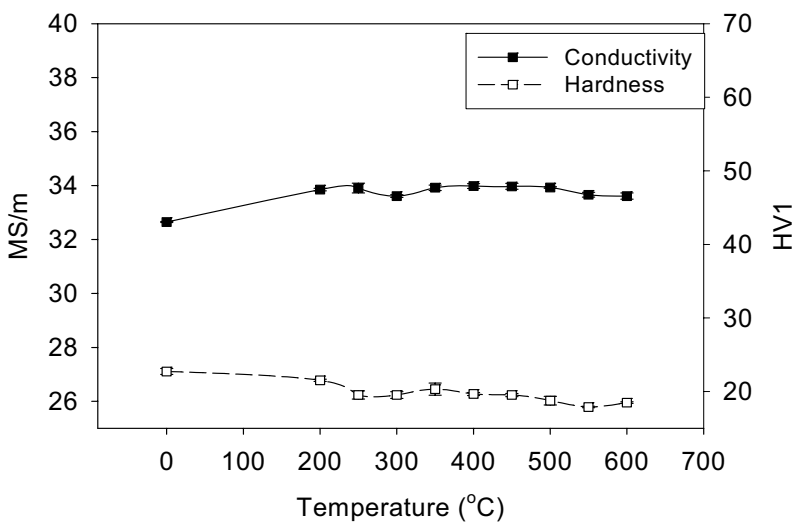

Figure 9.17 Continuous annealing of Al-0,22Hf-0,11Zr showing conductivity and microhardness at various temperatures.

Part A

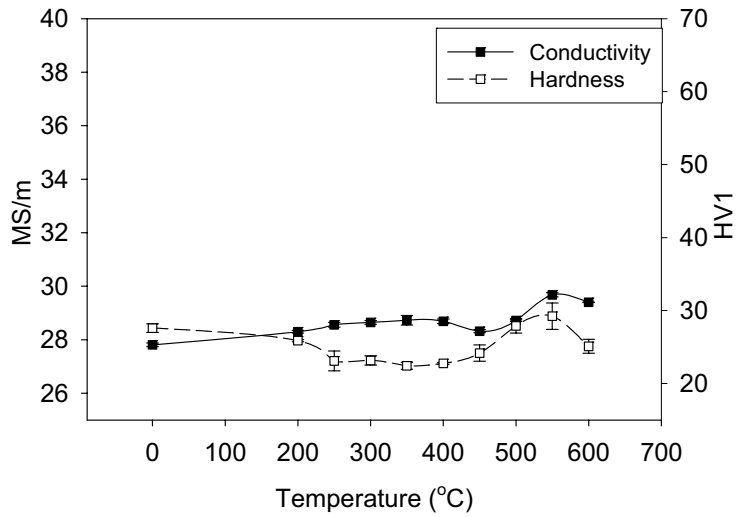

Figure 9.18 Continuous annealing of Al-1,0Hf-0,12Zr showing conductivity and microhardness at various temperatures.

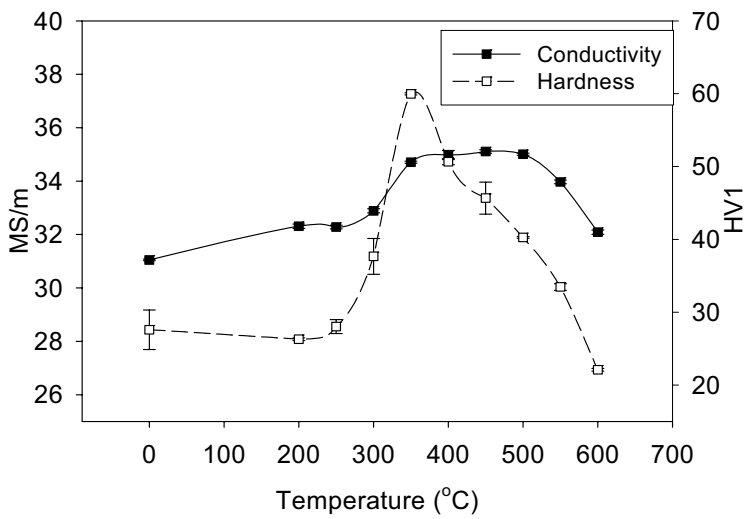

Figure 9.19 Continuous annealing of Al-0,22Hf-0,15Sc showing conductivity and microhardness at various temperatures.

Part A

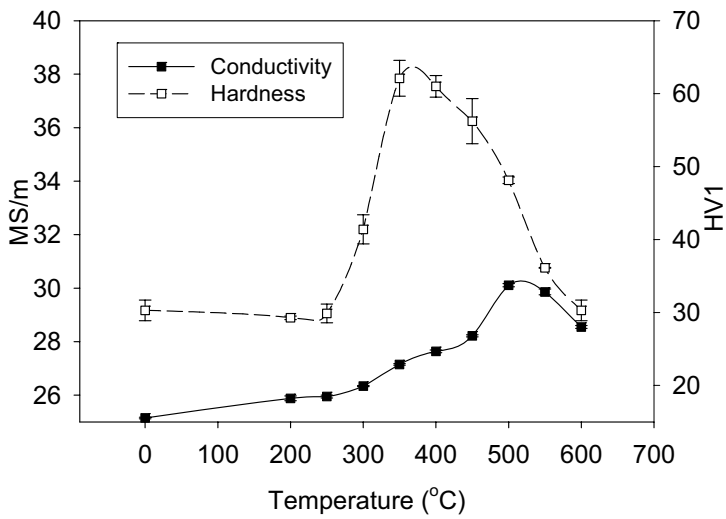

Figure 9.20 Continuous annealing of Al-1,1Hf-0,17Sc showing conductivity and micro hardness at various temperatures.

10 Cold rolling and annealing

Deformed, “pancake”-shaped grains with a subgrain structure and a high interior dislocation density form during cold-rolling. The stored energy in such deformation structures provides the driving force for recrystallisation during subsequent heat treatment, see Chapter 2. As recrystallisation is connected with a considerable loss in strength, dispersoid-forming elements are added to aluminium alloys in order to inhibit this process [Reiso (1980), Humphreys and Hatherly (1995), Riddle et al. (2002)].

The objective of the work presented in this chapter was to investigate the recrystallisation resistance of the alloys considered in this thesis after homogenisation (50^{o}C/hr up to 475^{o}C and held for 20hrs) and cold rolling. This was done in order to determine an adequate chemical composition of alloys for further processing and investigations. The binary Al-Hf alloys are not investigated to a greater extend here since they already showed poor precipitation potential as discussed in the previous chapters.

10.1 Al-Hf alloys with additions of Si and Fe

Cold rolling followed by annealing
The samples were cold rolled down to 90% and heated at a heating rate of 50^{o}C/hr up to 600^{o}C as explained in the experimental part (Chapter 4). Samples taken out of the furnace at different temperatures and quenched in water were then subjected to hardness measurements and metallographic investigations.

Softening after cold rolling
Hardness curves of cold rolled and annealed material are given in Figures 10.1 and 10.2 for the four alloys selected for these investigations. The distinct drop in the strength is associated with recrystallisation. In Figure 10.1 results for Al-0,2Hf-0,15Si and Al-0,2Hf-1,0Si are plotted. The high Si containing alloy is fully recrystallised at 300^{o}C, while the low Si containing alloy started to recrystallise at 300^{o}C but was totally recrystallised first at 350^{o}C. In Figure 10.2, results for the Al-1,0Hf-0,15Si and Al-0,9Hf-1,0Si are plotted. The alloy with the highest Si level

is fully recrystallised at 350°C, while the other alloy stay unrecrystallised up to 450°C. Figure 10.3 gives a summary of the annealing experiments for different alloys. As we can see, binary Al-Si alloys recrystallise at 300°C, while binary Al-0,95Hf recrystallises at 400°C. All Al-Hf-Si alloys recrystallise at 350°C, except the Al-1,0Hf-0,15Si alloy which stays unrecrystallised up to 450°C, as mentioned earlier.

These observations can be related both to the number density/volume fraction as well as the distribution of dispersoids, i.e. the f/r-ratio at various locations in the alloys. This is described in the Introduction (Chapter 2), which shows that the Zener-drag and consequently the recrystallisation resistance becomes larger when the f/r-ratio increases. In the Al-Hf-Si alloys, the density of continuously precipitated dispersoids is much higher than in the binary Al-Hf alloys. As a consequence, the former alloys display a better recrystallisation resistance. As observed, Si does increase the driving force for precipitation , however, a heterogeneous distribution of spherical Al_3Hf-dispersoids is obtained in the Al-Hf-Si alloys. These observations confirm that several regions in the alloy with low dispersoid densities (low f/r), combined with the presence of large incoherent AlHfSi-particles still makes the Al-Hf-Si-alloys prone to recrystallisation.

Even though some Si is required to enhance the formation of continuously precipitated Al_3Hf-dispersoids, the results also indicate that the Si-content should not exceed a certain level as relatively coarse AlHfSi particles may form at the expense of Al_3Hf. This is clearly shown in the Al-Hf-Si alloy with a high Si content which recrystallises even at a lower temperature than a binary Al-Hf alloy, indicating that much of the Hf is tied up in AlHfSi particles instead of Al_3Hf dispersoids. As already mentioned these results are summarised in Figure 10.3.

Addition of Fe to the Al-Hf alloys seems to have only a slight effect on the precipitation reaction in the alloys, see Figure 10.4. It was observed that Fe goes into Al-Fe and Al-Hf-Fe particles in these alloys after solidification. In Al-Hf-Si alloys, increased amounts of Si seem to imply a higher consumption of Hf in form of AlHfSi particles. A corresponding effect is not observed for the Al-Hf-Fe alloys. Fe does not induce the same consumption of Hf as in the Si containing alloys. In fact, it does not seem that an increase in the Fe content from 0,11 to 0,44wt%, influence

the precipitation and thereby recrystallisation resistance to any significant extent.

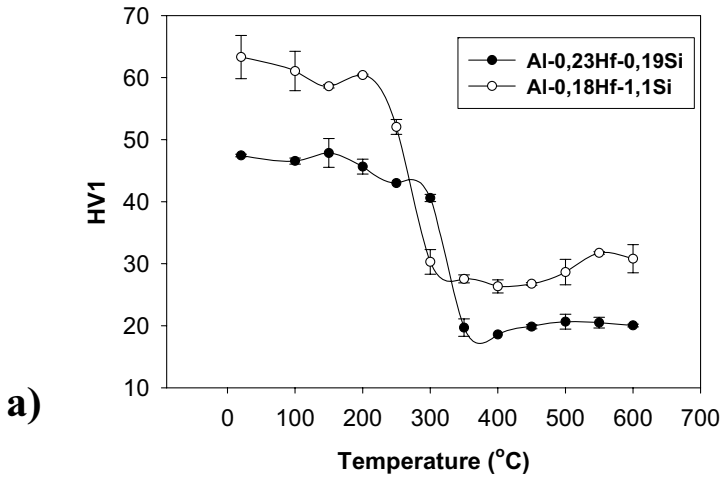

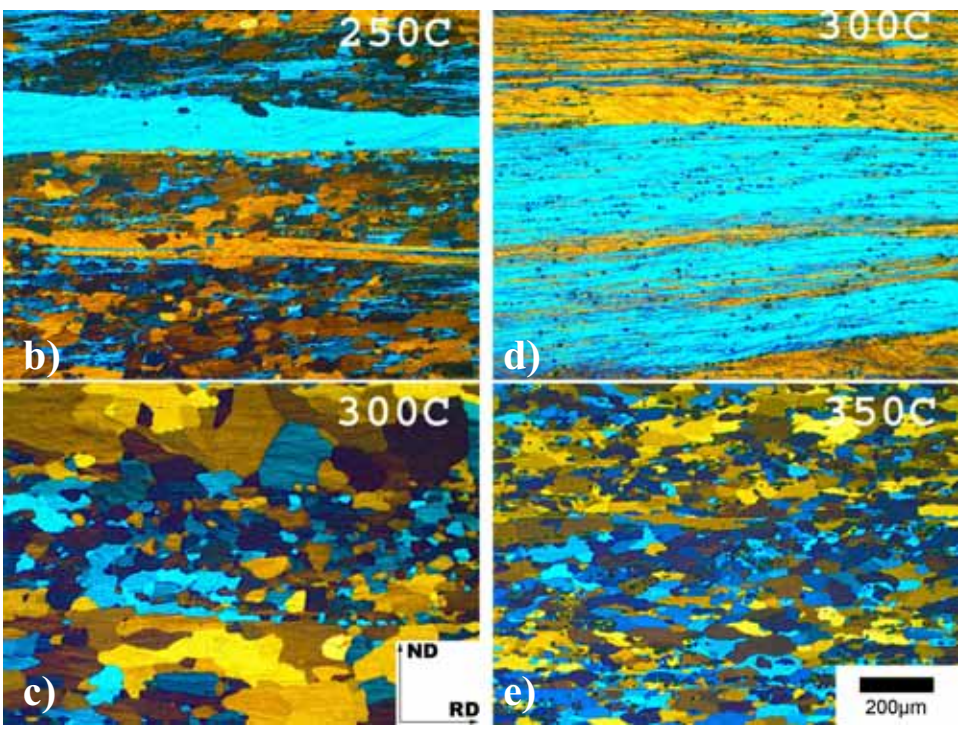

Figure 10.1 a) Softening curves after cold rolling and annealing. b and c) shows Al-0,18Hf-1,1Si, partly recrystallised at 250°C and recrystallised at 300°C. d and e) shows Al-0,23Hf-0,19Si, unrecrystallised at 300°C and recrystallised at 350°C.

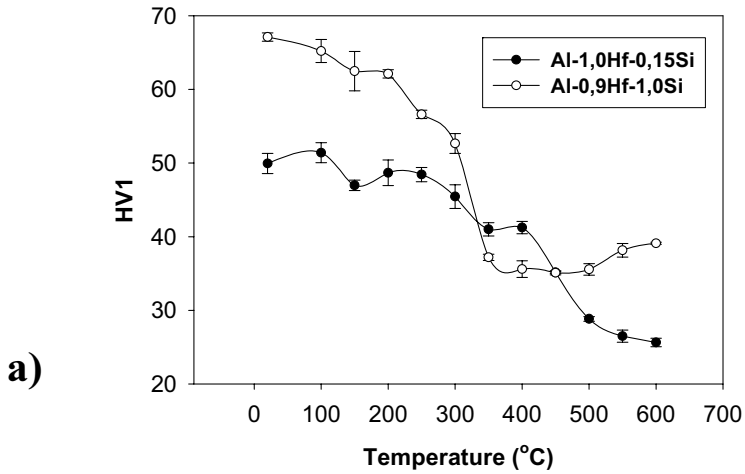

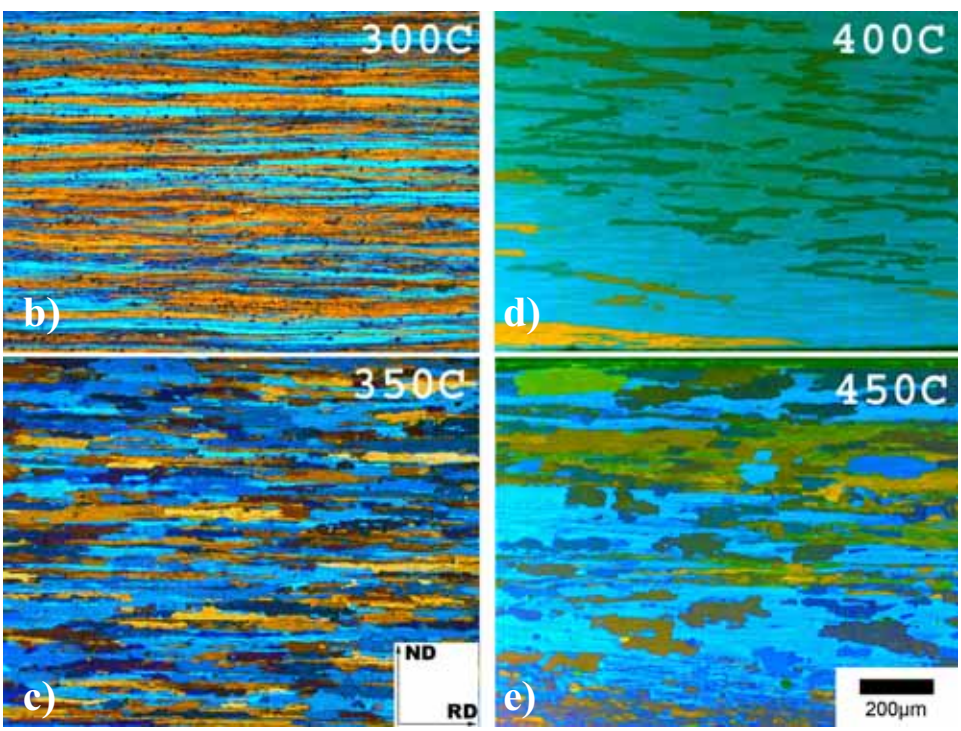

Figure 10.2 a) Softening curves after cold rolling and annealing. b and c) shows Al-0,9Hf-1,0Si, unrecrystallised at 300°C and partly recrystallised at 350°C d and e) shows Al-1,0Hf-0,15Si, unrecrystallised at 400°C and partly recrystallised at 450°C.

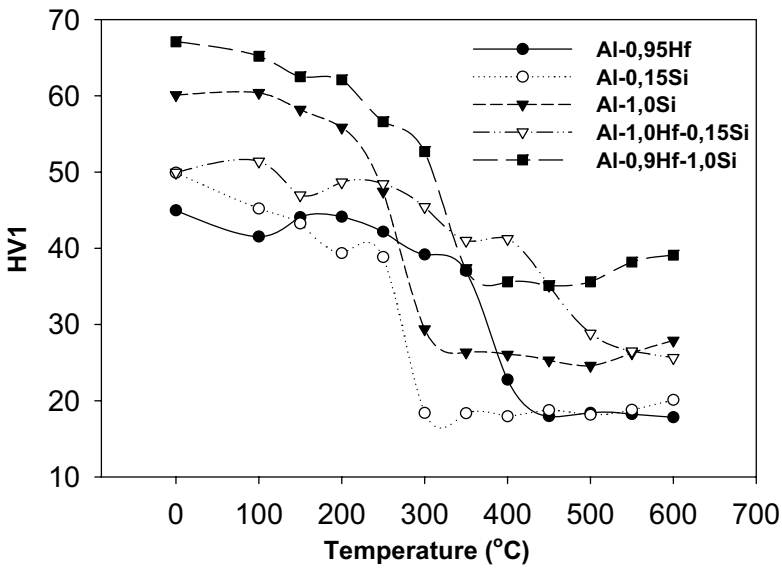

Figure 10.3 Softening curves of cold rolled Al-Hf, Al-Si and Al-Hf-Si alloy

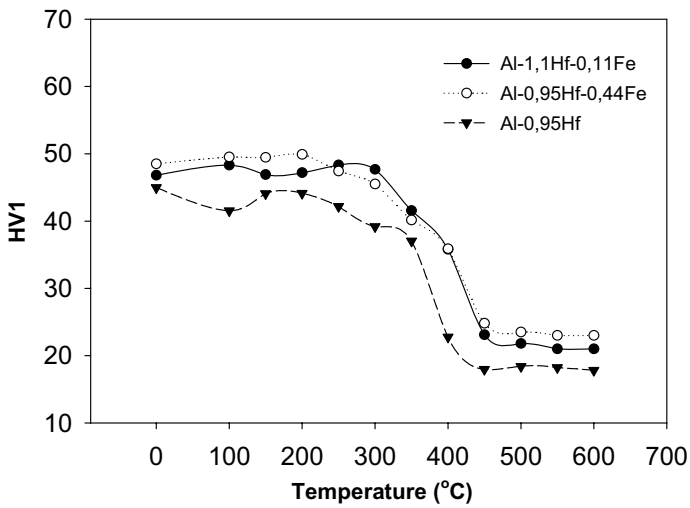

Figure 10.4 Softening curves of cold rolled Al-Hf and Al-Hf-Fe

10.2 Al-Hf alloys with additions of Sc and Zr

Cold rolling followed by annealing
Samples of Al-Hf-Sc-Zr alloys (see Table 7.4) were cold rolled down to 90% and annealed. The objective was again to determine how good the recrystallisation resistance was in each of the actual alloys, similar to the investigations discussed in Chapter 10.1

Softening after cold rolling
Figure 10.5 shows the softening curves for the Al-Hf-Zr alloys. These curves show that while the Al-0,2Hf-0,11Zr alloy only resists recrystallisation up to 400^{o}C, the Al-1,0Hf-0,12Zr alloy was able to resist recrystallisation up to 500^{o}C. The higher recrystallisation resistance can be attributed to the higher Hf content, which leads to the formation of more coherent Al_3(Hf,Zr) dispersoids, see also Chapter 9.3.

As expected from previous investigations [Riddle et al. (2002), Forbord et al. (2004a)], a higher recrystallisation resistance is obtained when Sc is used instead of Zr or in combination with Hf/Zr (Figure 10.6). Moreover, as demonstrated also for the other alloys a higher Hf-content seem beneficial with respect to the recrystallisation resistance. The first signs of recrystallisation were observed at 550^{o}C for the Al-0,22Hf-0,15Sc alloy and at 600^{o}C for the Al-1,1Hf-0,17Sc alloy (Figure 10.6). The high recrystallisation resistance of these variants can be attributed to the dense and homogeneous distribution of small Al_3(Hf,Sc)-dispersoids before annealing (r~12nm).

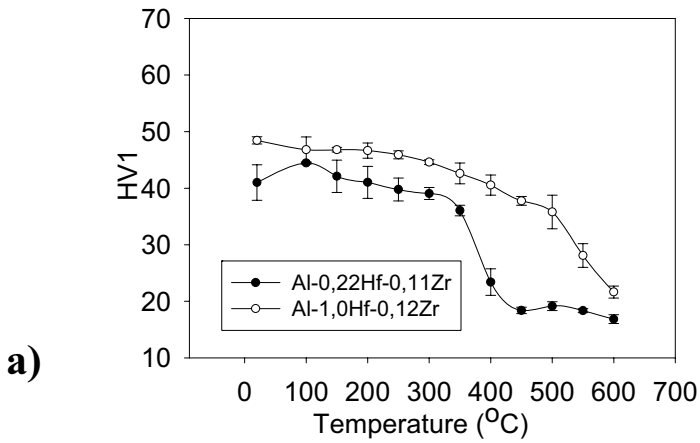

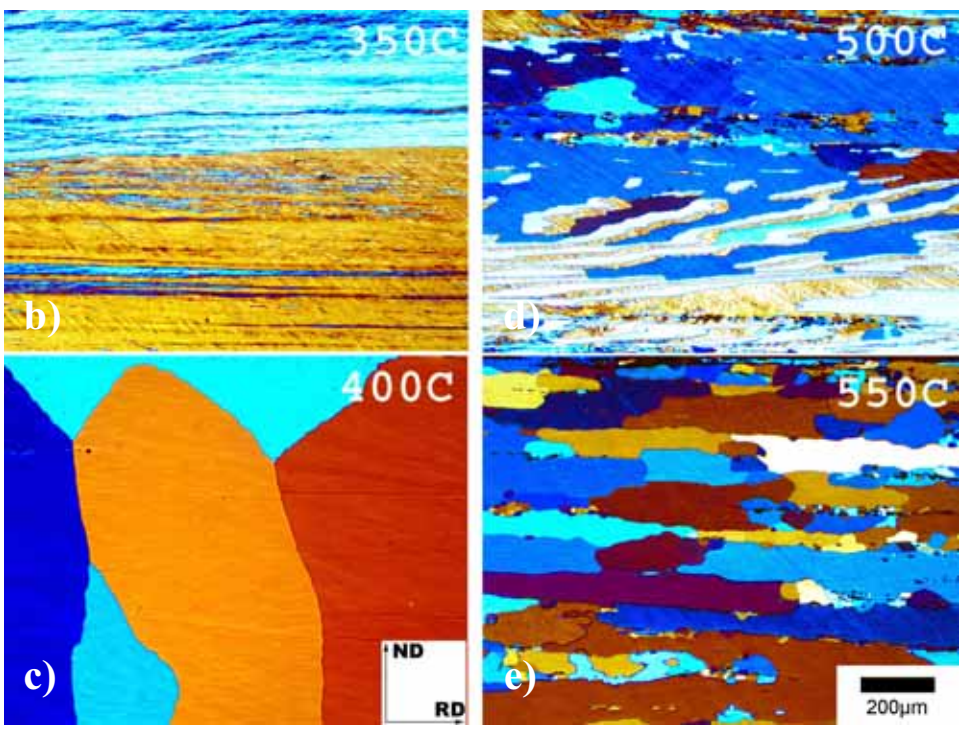

Figure 10.5 a) Softening curves after cold rolling and annealing. b and c) shows Al-0,22Hf-0,11Zr, unrecrystallised at 350°C and recrystallised at 400°C. d and e) show Al-1,0Hf-0,12Zr, unrecrystallised at 500°C and recrystallised at 550°C.

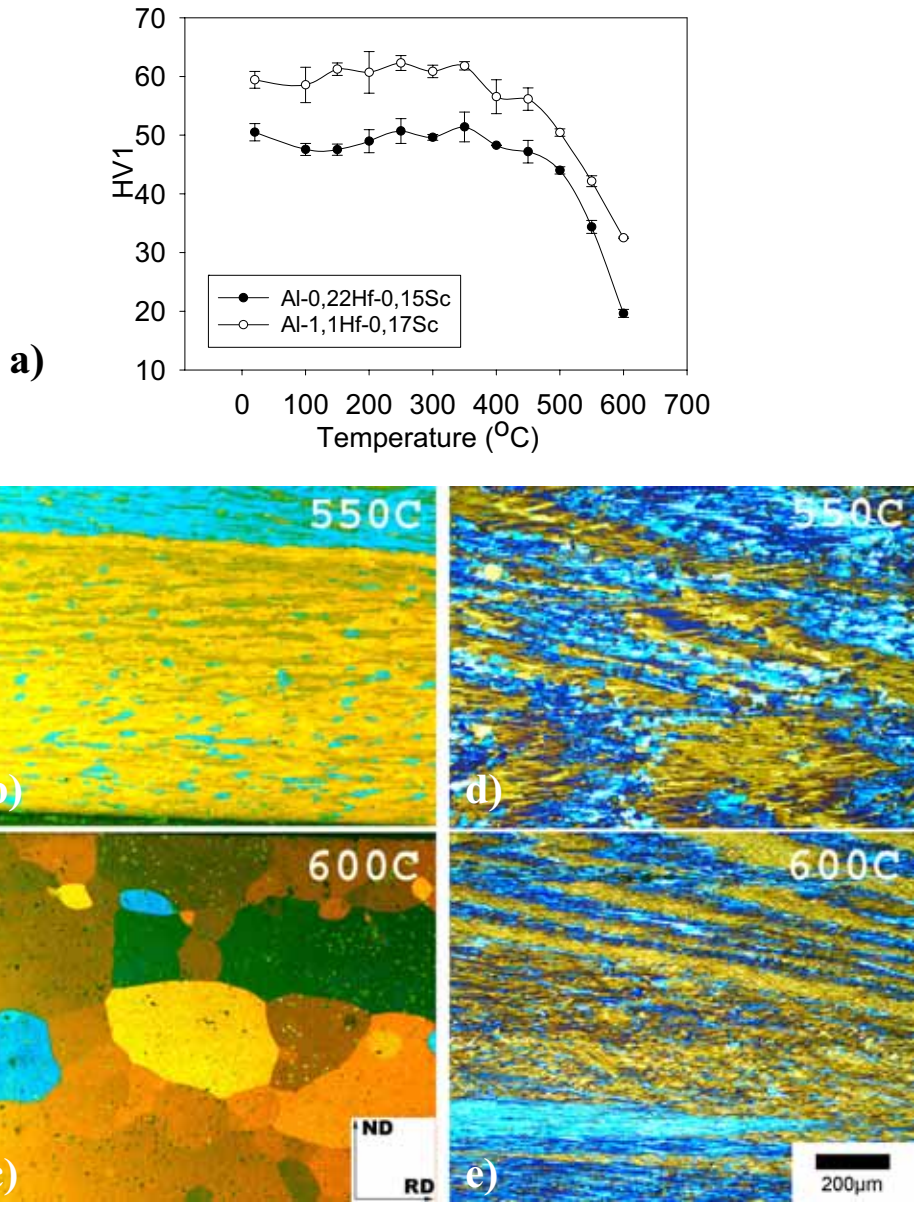

Figure 10.6 a) Softening curves after cold rolling and annealing. b and c) shows Al-0,22Hf-0,15Sc, unrecrystallised at 550°C and recrystallised at 600°C. d and e) show Al-1,1Hf-0,2Sc, unrecrystallised at 550°C and not or partly recrystallised at 600°C.

11 Summary

The addition of hafnium, scandium and zirconium in different combinations in Al-alloys has up to now not been well understood. In order to identify adequate levels of these elements with respect to obtaining the best possible recrystallisation resistance, during the pre-investigations (Part A) some questions have been answered, and from these results extrudable alloys of suitable composition are suggested as a basis for further investigations (see Part C).

11.1 Casting

Al-Hf alloys with directional solidification and a cooling rate about 10^{o}C/s form a cellular structure inside the grains. These cells have a high Hf content in the centre.

When a high Hf content (1,1wt%) is combined with additions of Sc and/or Zr, TCGs are formed. As the properties of alloys with these structures are not well known, these alloys are not considered to be suitable for further investigations. Investigations showed that in Al-Hf-Zr alloys, the Hf content should be less than about 0,7wt% to avoid TCGs. It is also important that the amount of Hf should be above 0,2wt% to improve the recrystallisation properties, as discussed below.

11.2 Homogenisation

Four different binary alloys with Hf content in the range from 0,17wt% to 0,95wt% were produced. These alloys showed poor precipitation properties. Nevertheless, most precipitation seemed to occur in the alloys with the highest content of Hf, although this was difficult to measure as the statistics were poor (very few dispersoids). It seems to be necessary to add other elements like Si and Fe to enhance the precipitation in the binary alloys.

It was found that addition of Si enhances the precipitation of Al_3Hf. However, if the content of Si was above 0,20wt% Si, the recrystallisation

resistance decreased. Also, a high Hf content gave more precipitation of Al_3Hf dispersoids in the Si containing alloys. With higher Si contents more of these AlHfSi containing particles were formed, thus reducing the amount of Hf available to precipitate the more effective and coherent Al_3Hf dispersoids for retarding recrystallisation. These observations seem to suggest that the Si level should be kept reasonably low (<0,2wt% Si).

With addition of Fe, the temperature to which the material withstood recrystallisation was increased about 50°C, but the amount (0,11-0,44wt%) did not seem to play an important role. The added Fe-levels gave almost no increase in hardness or changes in the conductivity.

Homogeneous and dense dispersoid distributions were obtained in the Al-Hf-Sc-alloys. In the Al-Hf-Zr-variants, however, few relatively coarse and heterogeneously distributed dispersoids were obtained.

In order to be able to compare the different alloys, the homogenisation procedure should in principle be the same for all the alloys chosen for extrusion. The holding temperature should be longer for the Al-Hf and the Al-Hf-Zr alloys, since the diffusion and consequently the precipitation is much slower in these alloys. Ramping is also important (50°C/hr) so the slow diffusing elements like Hf and Zr get time to form the appropriate dispersoids, $Al_3(Sc,Zr)$ or $Al_3(Sc,Hf)$. From other investigations 50°C/hr is found to be adequate, as mentioned earlier (Chapter 2). A slower ramping could perhaps be beneficial; however, from an industrial point of view this would increase the costs. On the other hand, if the ramping is too fast large cubic dispersoids with a heterogeneously distribution do form, see Figure 11.1.

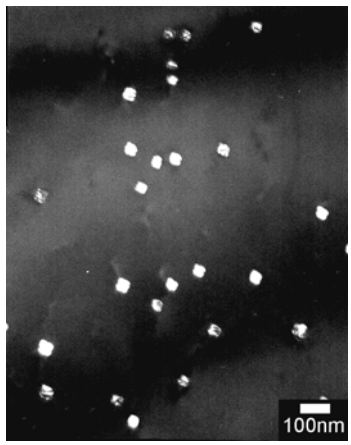

Figure 11.1 Al-Hf-Sc Flash annealed in salt bath at 450°C for 10min.

The holding temperature during homogenisation was set to 475°C, which has been found to work well in other investigations [Westengen et al (1980) Riddle et al. (2002), Forbord et al. (2004)]. If the temperature is lower, the diffusion will be slower and the time needed for homogenisation must be increased. If the temperature is higher, the diffusion will go too fast, forming large dispersoids. The highest conductivity in many of the alloys was found to be between 450-500°C.

The homogenisation process is further investigated by atom probe, see Part B. Nevertheless, optimising the heat treatments was not the main objective of this investigation.

11.3 Cold rolling and annealing

Cold rolling of the alloys, followed by annealing, showed that a high Si content lowered the recrystallisation resistance if it exceeded 0,20wt%. The Fe content did not indicate such a limit for the Fe levels considered here. In the Al-Hf-Zr alloys it was necessary with a high Hf level to get good recrystallisation resistance. Though, in the Al-Hf-Sc alloys it seems that the Hf levels did not have the same influence as in the Al-Hf-Zr system. In the alloys studied here, a possible negative effect from the TCGs seems to be overshadowed by the positive effect from the dispersoids. Nevertheless, since little is known about the effect of TCG,

these microstructure features are unwanted in alloys used for further studies in this investigation.

11.4 Alloys for extrusion

From the investigations described in this part, it is possible to draw some conclusions with respect to adequate amounts of different alloying elements. The Hf content should be in the range 0,40-0,60wt% in alloys for further investigations to avoid TCGs, but still with a high enough level to get reasonable precipitation. A suitable Sc level is in the range 0,15-0,20wt%. It has been found that alloys containing 0,2wt%Sc display good properties, however, the Sc level should not be too high for economical reasons. The Zr level should bee held around ~0,15wt%, since investigations in the past have shown good precipitation potential at this level and this is also a common level in industrial Al-Zr alloys. Suitable Si and Fe levels are approximately 0,15wt% and 0,20wt% respectively. This is common levels in industrial alloys and the Si content is not too high to give any problems in combinations with Hf.

Suggested compositions (wt%) of alloys for further investigations by extrusion and post extrusion annealing described in Part C are:

Al-(0,40-0,6)Hf-(0,15-0,20)Sc-0,15Zr-0,15Si-0,20Fe

12 References

Althenpol, D., *Aluminium and Aluminiumlegierungen*, Springer-Verlag, p.526, 1965

ASM Speciality Handbook, „*Aluminium and Aluminium alloys"* Third printing (ISBN: 0-87170-496-x), 1994

Dons, A.L., Jensen, E.K., Langsrud, Y., Trømborg, E., Brusethaug, S., Metall. Trans. A, Vol. 30A, p.2135, 1999

Dons, A.L., Journal of Light Metals, Vol. 1, p.133, 2001

Fink, W.L., and Willey, L.A., Trans. Met.Soc. AIME, 133, p.69, 1939

Forbord, B., Hallem, H., Ryum, N., Marthinsen, K., Materials Science and Engineering A, Volumes 387-389, pp. 936-939, 2004a

Forbord, B., Hallem, H., Marthinsen, K., ICAA-9, Brisbane, Australia,, pp.1179-1185, 2004b

Hori, S., Furushiro, N., Fujitani, W., Vol 30, No11, pp.617-625, 1980

Hori, S., Furushiro, N., Fujitani, W., Vol 31, No10, pp.649-654, 1981

Humpherys, F.J., and Hartherly, M., *Recrystallisation and related annealing phenomena*, Pergamon Press, Oxford, 1995.

Jones, G.P., and Pearson, J., Metallurgical Transactions B, Vol.7B, p.223, 1976

McCartney, D.G., Grain refining of aluminium and its alloys using innoculant, Int.Mat.Review., Vol. 34, No. 5, pp.247-260, 1989

Murray, J.L., McAlister, A.J., Kahan, D.J., Journal of Phase Equilibria Vol. 19, No 4, pp.376-379, 1998

Norman, A.F., and Tsakiropolous, P., Internat. J. Rapid Solidification, Vol 6, pp.185-213, 1991

Part A

Norman, A.F., and Tsakiropolous, P., Internat. J. Rapid Solidification, Vol 7, pp.109-126, 1992

Norman, A.F., Prangnell, P.B., McEwen, R.S., Acta mater, Vol 46, No. 16, pp.5715-5732, 1998.

Rath, B.R., Mohantry, G.P., Mondolfo, L.F., J. Inst. Metals, 89, p. 248, 1960

Reiso, O., Westengen, H., Auran, L., Årdal og Sunndal Verk a.s, Sunndalsøra, Aluminium, p.186-188, 1980

Riddle, Y.W., Hallem, H., Ryum, N., Mats.Sci.Forum, Vols.396-402, pp.563-568, 2002

Røyset, J., Dr. Ing. Thesis, The Norwegian Institute of Technology, Trondheim, 2002.

Ryum, N., Journal of Material Science, 10, pp.2075-2081, 1975

Westengen, H., Reiso, O., Auran, L., Sunndalsøra, Aluminium, pp.768-775, 1980

Part A

Part B : Precipitation kinetics in Al-Hf-Sc-(Zr) alloys studied by TEM and Atom Probe.

Part B

13 Introduction Part B

Recrystallisation and strength loss may be prevented by the presence of small dispersoids, which exert a retarding force (Zener drag) on migrating subgrain/grain boundaries [Zener/Smith (1948)]. The dispersoids are most effective when they are homogeneously distributed, coherent with the Al-matrix and present at high *f/r*-ratios. In other words: as explained in the introduction a high volume fraction, *f*, of small dispersoids homogeneously distributed in the material is favourable [Humphreys and Hatherly (1995), Jones (1979)]. It is also important that the dispersoids are thermally stable, i.e. coarsen slowly.

Additions of Sc or Zr have led to a substantially improved recrystallisation resistance in many aluminium alloys [Rostova (2000), Forbord et al. (2004a-b), Hallem et al. (2004a), Robson et al. (2003)]. These elements form coherent Al_3X-$L1_2$ compounds (X = Hf, Sc or Zr) [Drits et al.(1984), Desch et al. (1991)] with the Al matrix when added separately to Al. Single additions of these elements do not, however, lead to the optimum micro-structure, as for instance Zr-additions lead to heterogeneous Al_3Zr-distributions upon annealing [Forbord et al. (2004a), Nes (1972)]. Although a more homogeneous distribution of Al_3Sc dispersoids usually are obtained when Sc is added, the high diffusivity of Sc implies that the dispersoids may coarsen relatively fast [Hyland (1992), Marquis (2001)]. Combined additions of Sc and Zr, on the other hand, lead to a high number density of homogeneously distributed $Al_3(Sc,Zr)$-dispersoids which coarsen slowly, thus enabling the alloy to maintain strength at high temperatures [Riddle (2000), Davydov (1996), Zakharov (1997)]. However, even though only small additions are required due to their low solubilities in Al [Toropova (1998)], the cost in particular of Sc, has limited the industrial use of these alloying elements.

The precipitation reaction in Al-Zr-Sc alloys has recently been investigated in great detail by means of three-dimensional atom probe (3DAP) field ion microscope (FIM) [Forbord et al. (2004c), Lefebvre et al. (2005)]. In Part B of the present work the results obtained in the Al-Sc-Zr-system will be compared with the precipitation of dispersoids in Al-Hf-Sc and Al-Hf-Sc-Zr. As mentioned several times Hf is a relatively unexplored element which shows many similarities to Zr, [Hallem (2004a-b)]. The aim of the present work has been to study to which extend additions of Hf alter the nucleation kinetics and coarsening of

dispersoids in these alloys. Following Lefebvre et al. (2005), a non-isothermal approach has been applied in order to accurately describe the effect of diffusion on nucleation and the various stages of dispersoid formation. Both atom probe (AP) and transmission electron microscopy (TEM) investigations have been carried out in order to study early clustering, structural information and dispersoid size distributions and volume fractions.

14 Experimental

The Al-Sc-Zr, Al-Sc-Hf and Al-Hf-Sc-Zr alloys in Table 14.1, were made as explained in Chapter 4.1. The annealing was performed with a heating rate of 50ºC/h, and specimens were removed from the forced air circulation furnace when the temperature, T_1, reached 290°C, 350°C and 475°C, respectively. The material was then water-quenched in order to "freeze" the structure for subsequent AP- and TEM-investigations for which the techniques and experimental details are explained in Chapters 4.7.4 and 4.7.5 Two samples were also held at 475ºC for 15-20 hours in order to open for studies of the "fully developed" dispersoids.

It is important to notice that there are only two different Hf-containing alloys, Al-Hf-Sc and Al-Hf-Sc-Zr, which are compared with the Al-Sc-Zr alloys. Due to the cost of these types of investigations it was not possible to investigate all the alloys in all the different conditions. The alloys and in which condition they have been investigated, are given in Table 14.1. It is hoped that this gives a representative picture on the precipitation and coarsening behaviour in these alloys and possible differences between them.

Table 14.1 Composition of alloys and the different annealing times and temperatures used for AP and TEM investigations

Chapter	Alloys (Wt%)	Heat treatment 50°C/hr to:	Comments
Clustering	Al-0,43Hf-0,20Sc	290°C	Effect of Hf and Zr in Al-Sc alloys
Clustering	Al-0,15Sc-0,15Zr	290°C	
Precipitation	Al-0,44Hf-0,22Sc-0,13Zr	350°C	Effect of Hf in Al-Sc-Zr alloys
Precipitation	Al-0,15Sc-0,15Zr	350°C	
Precipitation	Al-0,44Hf-0,22Sc-0,13Zr	475°C	
Precipitation	Al-0,15Sc-0,15Zr	475°C	
Coarsening	Al-0,44Hf-0,22Sc-0,13Zr	475°C (20hrs)	Effect of Hf in Al-Sc-Zr alloys
Coarsening	Al-0,15Sc-0,08Zr	475°C (15hrs)	

15 Precipitation during homogenisation

Figures 15.1-15.2 show the evolution in hardness and conductivity during homogenisation of an Al-0,21wt%Sc-0,11wt%Zr alloy and an Al-0,44w%Hf-0,22wt%Sc-0,13wt%Zr alloy, respectively. In both alloys a substantial increase in hardness and conductivity was observed when a temperature of ~250°C was reached, indicating that this is the temperature where dispersoid formation begins. It should also be noted that peak hardness is obtained at a similar temperature, T=350˚C. An interesting observation is that the Hf-containing alloy softens more gradually than the Al-Sc-Zr alloy during the isothermal annealing at 475°C. While the strength drops ~15 VHN in Al-Sc-Zr during the first 5 hours at 475°C (Figure 15.1), 15 hours of annealing is required to obtain a similar degree of softening in Al-Hf-Sc-Zr (Figure 15.2).

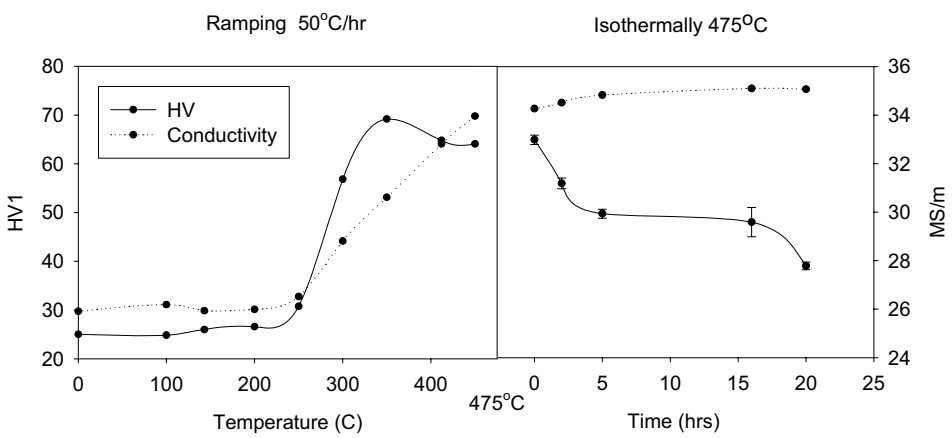

Figure 15.1 Evolution in hardness and conductivity during homogenisation of an Al-0.21wt%Sc-0.11wt%Zr alloy. The figures show the evolution during heating to the homogenisation temperature, T_{hom}=475˚C (left) and subsequent holding at T_{hom} (right).

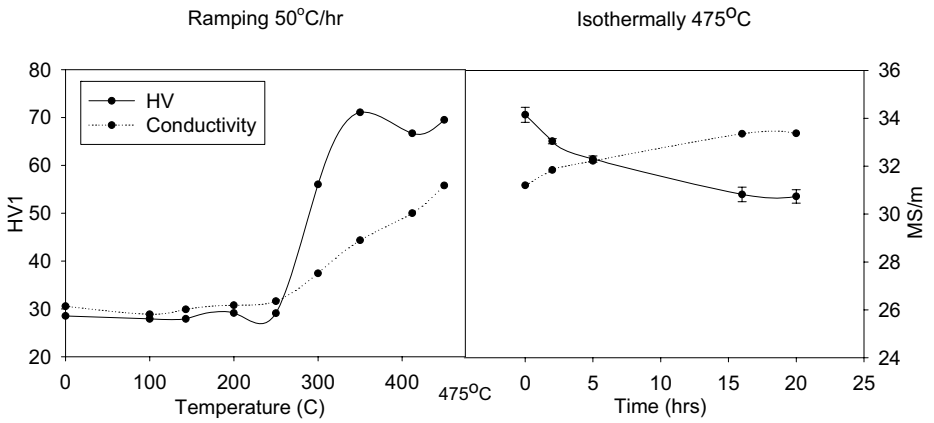

Figure 15.2. Evolution in hardness and conductivity during homogenisation of an Al-0.44wt%Hf-0.22wt%Sc-0.13wt%Zr alloy. The figures show the evolution during heating to the homogenisation temperature, T_{hom}=475˚C (left) and subsequent holding at T_{hom} (right).

16 Precipitation kinetics of dispersoids

In this section, the precipitation kinetics of dispersoids in Al-Hf-Sc and Al-Hf-Sc-Zr will be summarised and compared with the previously reported results for Al_3(Sc,Zr)-formation in Al-Sc-Zr-alloys [Forbord et al.(2004c) and Lefebvre et al. (2005)]. The section will be divided into three parts; clustering, precipitation and coarsening/growth.

Clustering: The hardness and conductivity curves in Figures.15.1-15.2 revealed that precipitation began at approximately 250˚C. In order to be sure of observing the earliest stages of dispersoid formation/clustering by Atom Probe and TEM, a slightly higher temperature, 290°C, was selected. In order to investigate the clustering of Sc, Zr and Hf a cluster identification routine has been applied [Heinrich (2003), Vaumousse (2003)], see Lefebvre et al (2005) for details. By first looking at the results obtained for Al-Sc-Zr by Lefebvre et al. (2005)(Figure 16.1), the reconstructed 3D-volume clearly shows a Sc-rich cluster marked within the circle. No clustering of Zr was observed.

Similar results were obtained in the Al-Hf-Sc alloy. The Field Ion Micrograph in Figure 16.2, reveals small and slightly larger bright spots corresponding to Hf or Sc atoms or clusters, respectively. However, FIM cannot provide details about the composition of the clusters. The

reconstructed 3-D volume in Figure 16.3, on the other hand, reveals that it is actually Sc-clustering also in Al-Hf-Sc at 290°C. These clusters were found to have a radius of 1-2 nm. Similar to the absence of Zr-rich clusters in Al-Sc-Zr, no Hf-clusters were identified by the 3D-volume in Al-Hf-Sc.

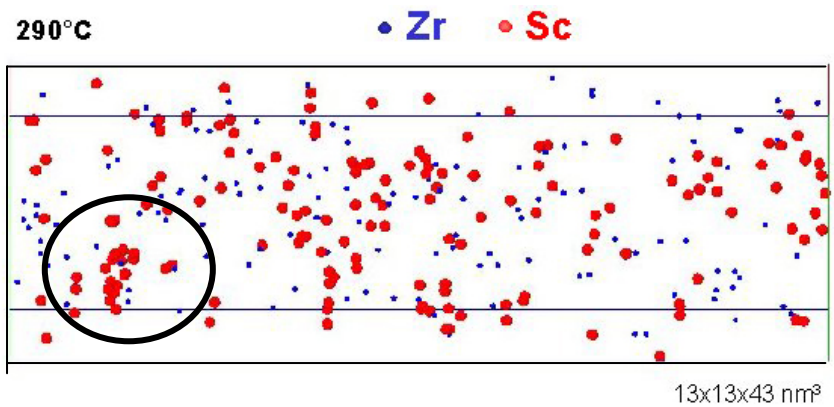

Figure 16.1 Reconstructed 3D-volume in an Al-Sc-Zr alloy with dimensions 13x13x43 nm^3. The circle marks a region with a cluster. Red and blue spheres denote individual Sc- and Zr-atoms, respectively [Lefebvre et al. (2005)].

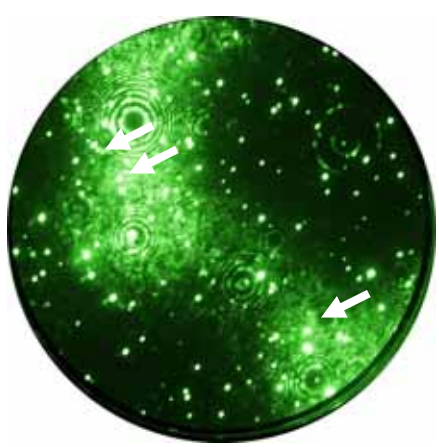

Figure 16.2 Field Ion Microscopy micrograph of an Al-Hf-Sc sample. The small and slightly larger bright spots correspond to Hf/ Sc-atoms or clusters, respectively.

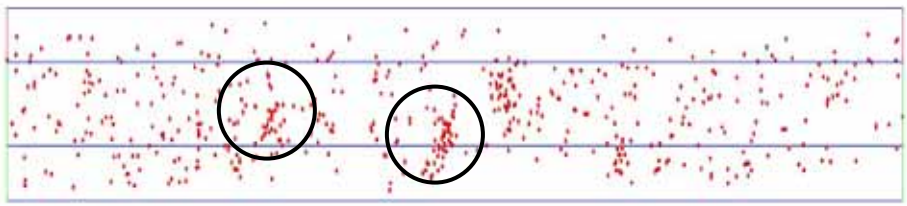

Figure 16.3 Reconstructed 3D-volume in an Al-Sc-Hf alloy with dimensions 11x11x120 nm^3. The circles mark regions with initial clustering. Red spheres denote individual Sc-atoms.

Dispersoids at peak hardness, T=350˚C: The hardness curves in Figures 15.1-15.2 reveal that peak hardness was obtained in both Al-Sc-Zr and Al-Hf-Sc-Zr when 350^{o}C was reached. This temperature was therefore interesting with respect to investigation of the dispersoids. The presence of superlattice reflections in the TEM-micrographs in Figures 16.4-16.5, both for the Al-Hf-Sc-Zr and the Al-Sc-Zr-alloys, clearly demonstrate that the dispersoids at this stage have developed the $L1_2$ structure typical for stable Al_3Sc- and metastable Al_3Hf- and Al_3Zr-phases. Figure 16.6, which shows a reconstructed 3D-volume of Al-Sc-Zr [Lefebvre et al. (2005)], reveals that virtually no Zr is present in the dispersoids, i.e. the dispersoids can almost be considered as "pure" Al_3Sc-phases. Figure 16.7 shows that a similar result was obtained in Al-Hf-Sc-Zr in the present work .

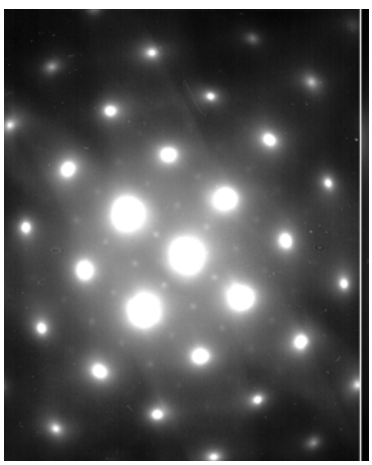

Figure 16.4 Diffraction micrographs of Al-Hf-Sc-Zr. The superlattice spots from the dispersoids can be seen between the relatively large spots from the matrix.

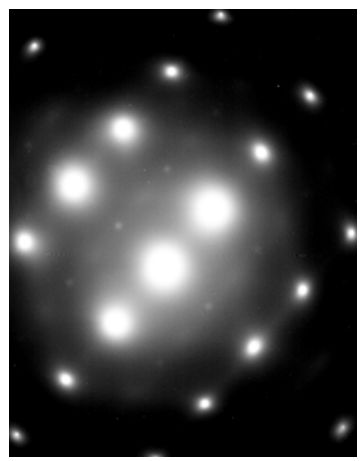

Figure 16.5 Diffraction micrographs of Al-Sc-Zr. The superlattice spots from the dispersoids can be seen between the relatively large spots from the matrix.

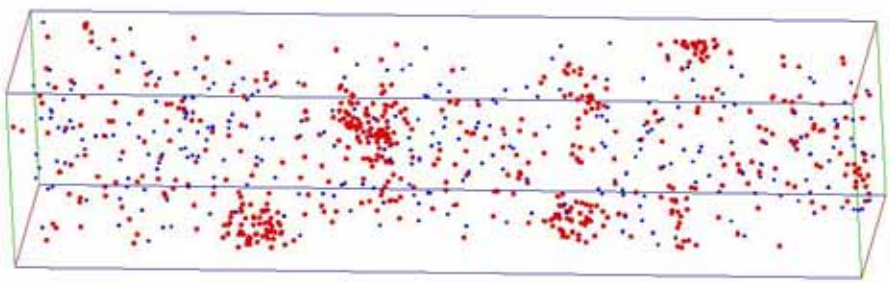

Figure 16.6 Rebuilt 3D volume with dimension 15x15x55 nm^3 in an Al-Sc-Zr alloy showing Sc-rich clusters at 350°C. Red and blue spheres denote individual Sc- and Zr-atoms, respectively. Zr is found randomly in the matrix. [Lefebvre et al. (2005)].

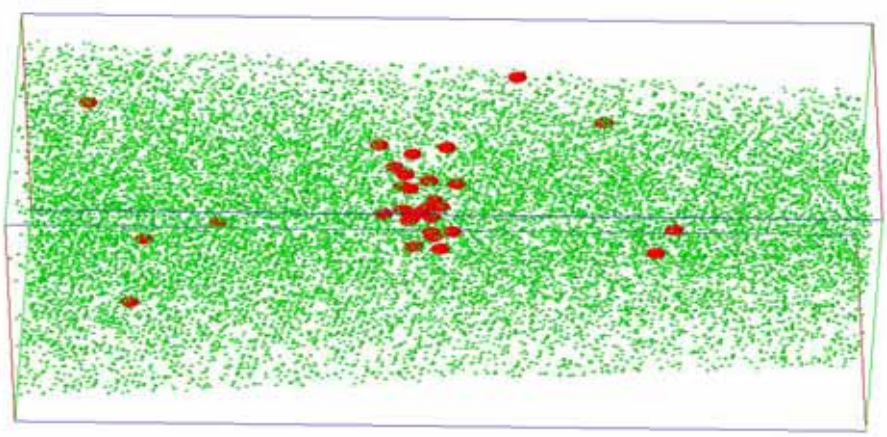

Figure 16.7 Rebuilt 3D volume with dimension 7x7x17 nm^3 in an Al-Hf-Sc-Zr alloy showing Sc-rich clusters at 350°C. Red and green spheres denote individual Sc- and Al-atoms, respectively. Atomic planes can also be seen. Zr and Hf were distributed randomly in the matrix and are consequently not shown in the figure.

Dispersoids at T=475˚C: Figures 16.8-16.9 show 3D-volumes, from the Al-Sc-Zr and the Al-Hf-Sc-Zr alloys, respectively, at 475°C. These figures reveal that at this stage, both Hf and the Zr have begun to diffuse towards the matrix-dispersoid interfaces. Typical composition profiles through selected dispersoids that are given in Figures 16.10-16.11, reveal a Sc-rich core surrounded by a shell containing Sc and Zr or Sc, Hf and Zr, respectively. Once again superlattice reflections corresponding to the

$L1_2$ structure of the dispersoids could be seen in between the spots from the matrix in the diffraction micrographs (Figures. 16.12-16.13).

Dispersoid sizes, number densities and volume fractions in Al-Hf-Sc-Zr is shown in Table 16.1. Along with the dark field TEM-micrograph in Figure. 16.13, the measurements show a high number density of dispersoids with an average size of 2,7 nm radius. The (f/r)-ratio was measured to be $0{,}9E10^{-3}$ nm^{-1}.

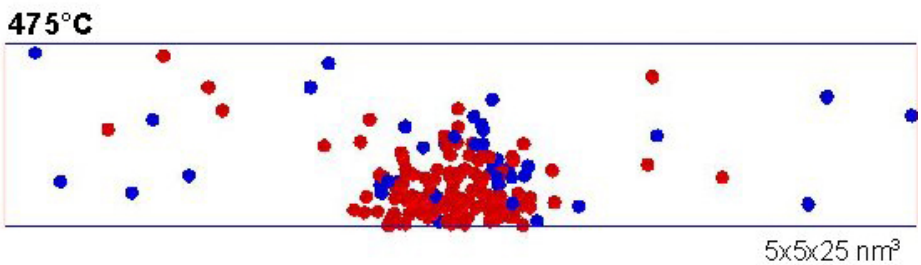

Figure 16.8 Rebuilt 3D volume with dimensions 5x5x25 nm^3 in an Al-0,15Sc-0,15Zr alloy at 475°C. Red and blue spheres denote Sc- and Hf-atoms, respectively [Lefebvre et al. (2005)].

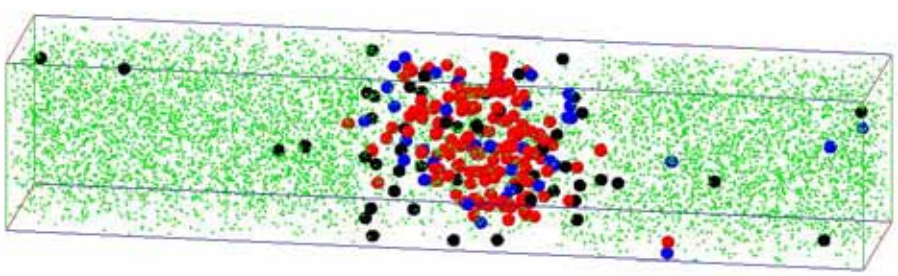

Figure 16.9 Rebuilt 3D volume with dimension 4x4x20 nm^3 in the Al-Hf-Sc-Zr alloy showing a dispersoid. Red, black, blue and green spheres denote Sc-, Hf-, Zr- and Al-atoms, respectively.

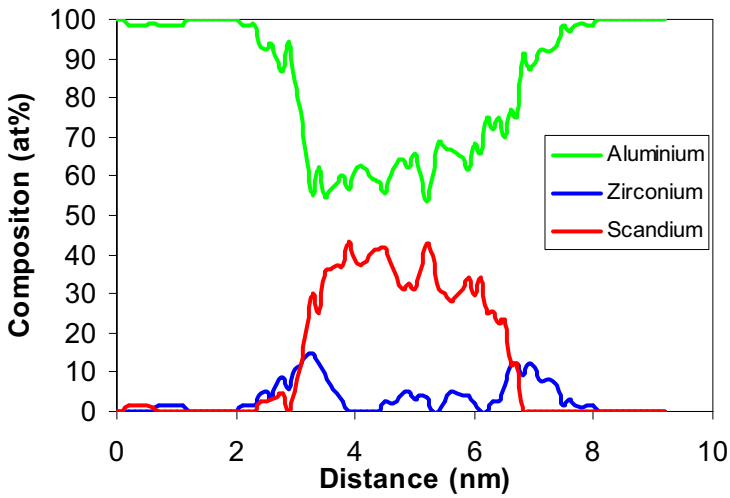

Figure 16.10 Chemical composition through a dispersoid in Al-Sc-Zr found by Atom Probe, clearly demonstrating that the dispersoids consist of a Sc-rich core surrounded by a Zr-containing shell [Lefebvre et al. (2005)].

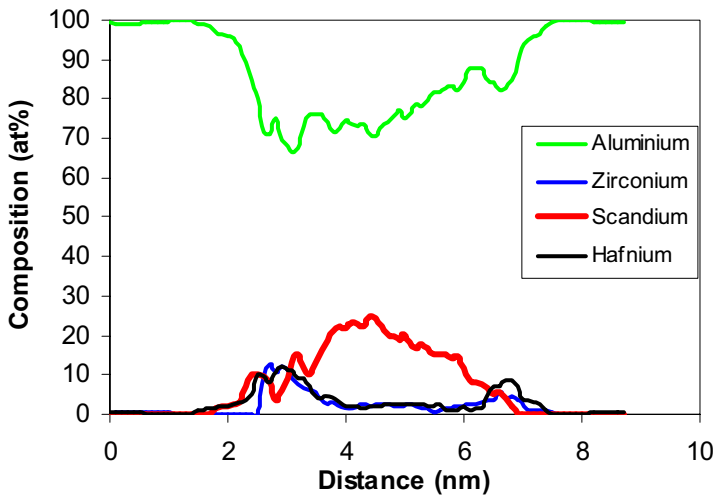

Figure 16.11 Chemical composition through a dispersoid in Al-Hf-Sc-Zr found by Atom Probe, clearly demonstrating that the dispersoids also for this alloy consist of a Sc-rich core, and in this case surrounded by a Zr- and Hf-contaning shell .

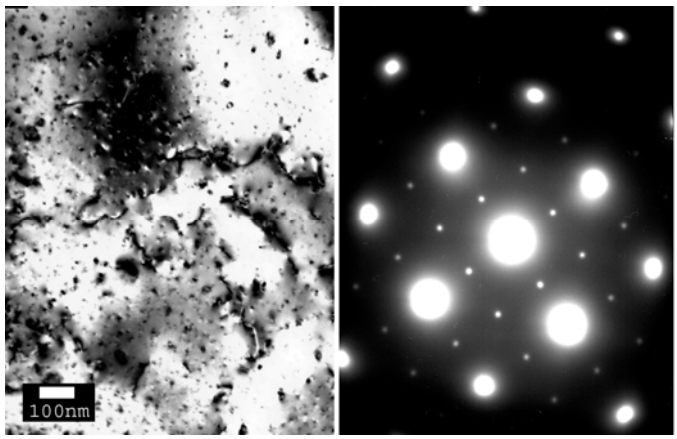

Figure 16.12 Bright field TEM-micrograph (left) and a corresponding diffraction pattern (right) showing superlattice reflections of $Al_3(Sc,Zr)$ at 475°C.

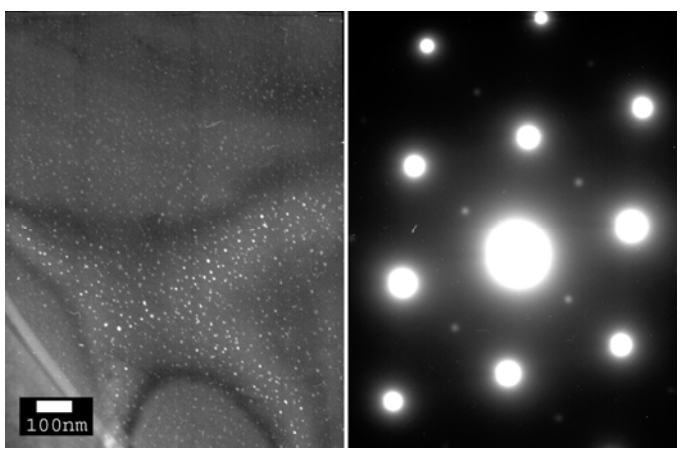

Figure 16.13 Dark field TEM-micrograph (left) and a corresponding diffraction pattern showing superlattice reflections (right) of $Al_3(Hf,Sc,Zr)$ at 475°C.

Table 16.1 Dispersoid data at 475°C

Alloy	Dispersoid radius [nm]	Number density [m^{-3}]	Volume-fraction f_v	(f/r) [nm^{-1}]
Al-Hf-Sc-Zr	2,7	$2{,}9E10^{22}$	$2{,}39E10^{-3}$	$0{,}9E10^{-3}$

No measurements obtained in the Al-Sc-Zr alloy.

Dispersoids during annealing at 475°C: During the isothermal annealing at 475°C, the Al-Sc-Zr- and Al-Hf-Sc-Zr-alloys behaved slightly different (Figures.15.1-15.2). While a drop in hardness was observed in the Al-Sc-Zr-alloy, Al-Hf-Sc-Zr softened more gradually. The explanation for this difference in behaviour can be found by studying the conductivity and dispersoid measurements.

From Tables 16.2 and 16.3 we notice that the number density of dispersoids, *N*, is 2.5 times higher in the Al-Hf-Sc-Zr alloy, and the average radius of the $L1_2$-structured dispersiods, *r*, is significantly smaller than in Al-Sc-Zr (Figures. 16.14-16.15 and Tables 16.2-16.3). This is consistent with an increase in conductivity found for this alloy which indicates additional precipitation, and which most likely reduces the rate of softening. In Al-Sc-Zr, on the other hand the conductivity was fairly constant during annealing at 475ºC. This latter result indicates that the change in dispersoid distribution in the Al-Sc-Zr alloy was solely due to coarsening. This assumption was confirmed by the measurements of the volume fraction, *f*, which was found to remain constant at 475ºC (Tables 16.2-16.3).

Furthermore, the atom probe studies of the individual dispersoids show that the diffusion of Zr and Hf to the matrix/dispersoid-interface continues during the annealing at 475ºC. The results obtained by Lefebvre et al. (2005) are given in Figures 16.16-16.17, which show a reconstructed 3D-volume and the composition profile through a relatively large dispersoid in Al-Sc-Zr after 15 hours annealing. Once again an Al_3Sc-core with diameter ~5 nm surrounded by a Zr-containing shell was found. An almost similar result was obtained for the Hf-containing alloy after 20 hours annealing, see Figures. 16.18-16.19. The diameter of the Sc-rich core was again found to be ~5 nm, but in this case Hf was found in addition to Zr in the surrounding shell, i.e. both Hf and Zr diffuses to the dispersoid/matrix-interface. The reasons for this will be discussed in more detail later.

Table 16.2 Dispersoid data at 475°C for 5 hrs.

Alloy	Dispersoid radius [nm]	Number density [m^{-3}]	Volume-fraction f_v	(f/r) [nm^{-1}]
Al-Hf-Sc-Zr	6,0	$2{,}19E10^{22}$	$1{,}98E10^{-2}$	$3{,}3E10^{-3}$
Al-Sc-Zr	8,5	$8{,}35E10^{21}$	$2{,}15E10^{-2}$	$2{,}5E10^{-3}$

Table 16.3 Dispersoid data at 475°C for 20hrs.

Alloy	Dispersoid radius [nm]	Number density [m^{-3}]	Volume-fraction f_v	(f/r) [nm^{-1}]
Al-Hf-Sc-Zr	9,3	1,82E10^{22}	6,02E10^{-2}	6,5E10^{-3}
Al-Sc-Zr	11,9	3,04E10^{21}	2,15E10^{-2}	1,8E10^{-3}

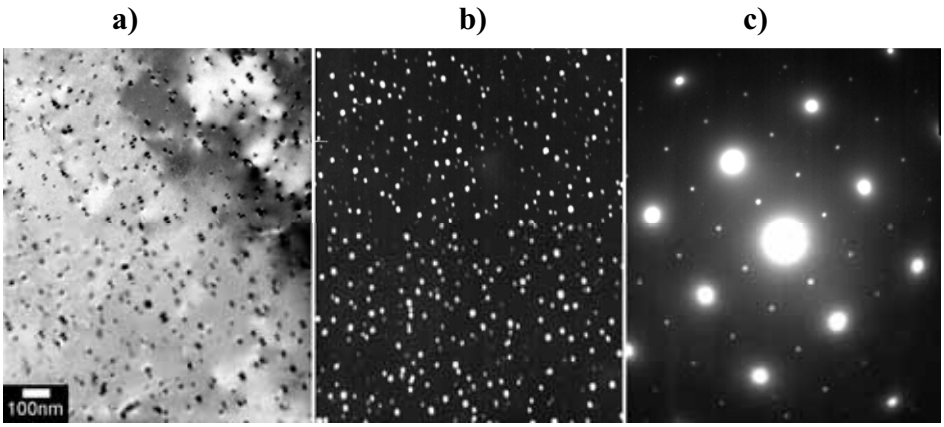

Figure 16.14 Al-Hf-Sc-Zr annealed for 20hr at 475°C (a) BF image of the dispersoids (b) DF image of the dispersoids (c) Diffraction image showing an ordered $L1_2$ structure.

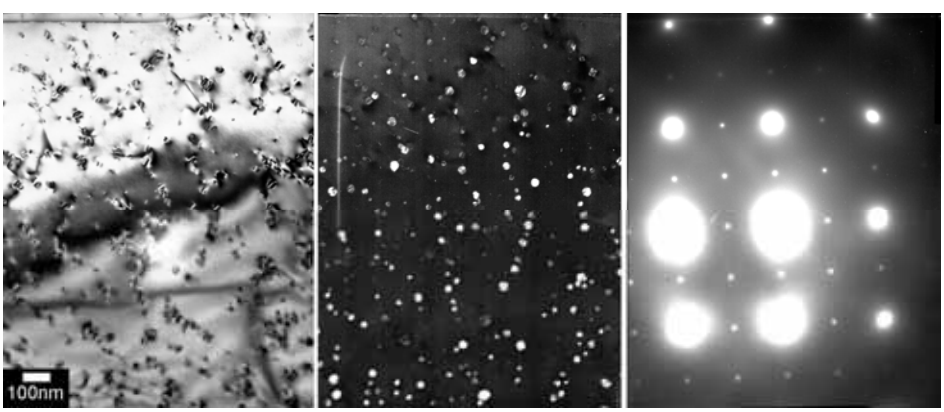

Figure 16.15 Al-Sc-Zr annealed for 20hr at 475°C (a) BF image of the dispersoids (b) DF image of the dispersoids (c) Diffraction image showing an ordered $L1_2$ structure.

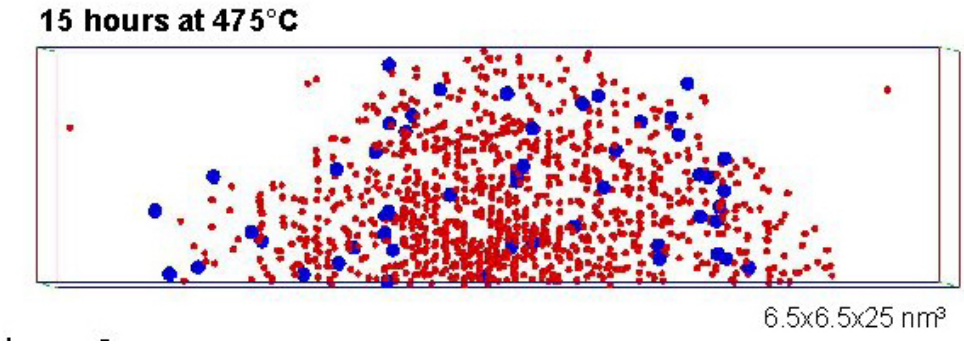

Figure 16.16 3D volume with dimensions 6.5x6.5x25 nm^3 in an Al-0,15Sc-0,08Zr showing the upper half of a spherical dispersoid. Red and blue spheres indicate Sc- and Zr-atoms, respectively [Lefebvre et al. (2005)].

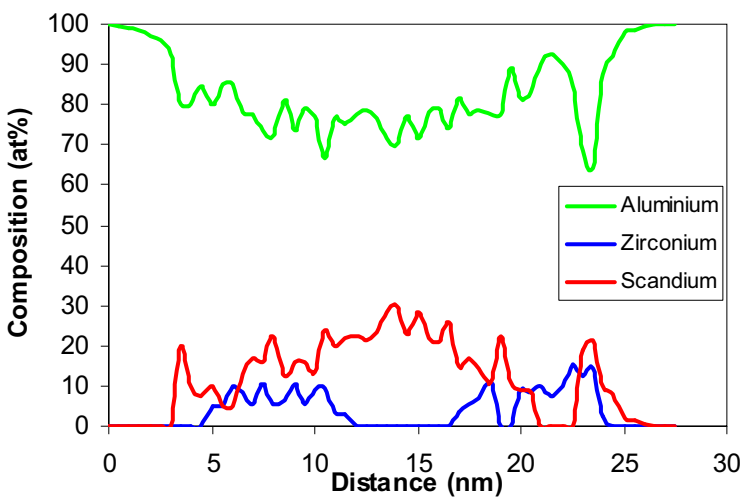

Figure 16.17 Chemical composition established by Atom Probe data through the Al_3(Sc,Zr)-dispersoid in Figure 16.16[Lefebvre et al. (2005)].

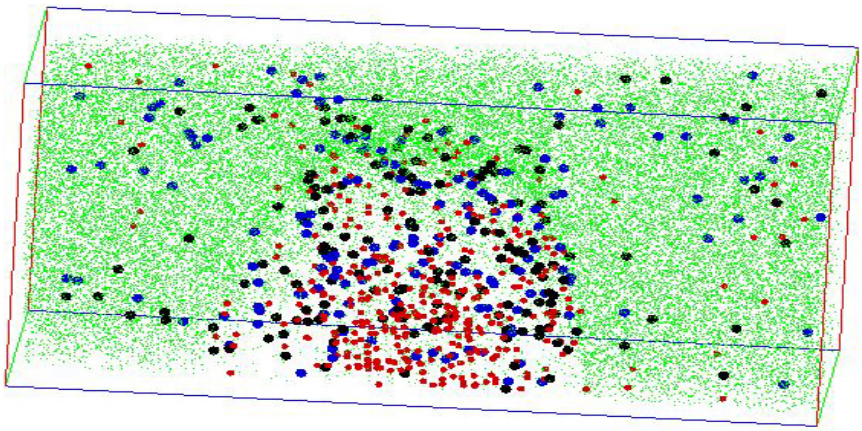

Figure 16.18 Rebuilt 3D volume with dimensions 10x10x20 nm^3 in an Al-Hf-Sc-Zr alloy heat treated for 20hr at 475°C. Red, blue, black and green spheres denote Sc-, Hf-, Zr- and Al-atoms, respectively.

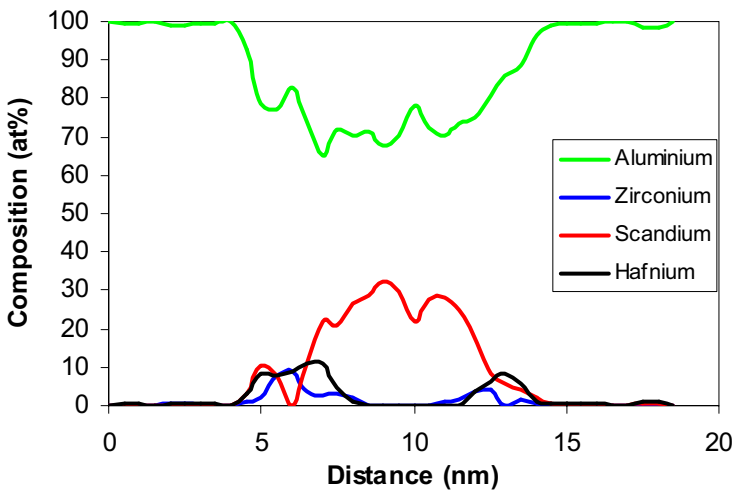

Figure 16.19 Chemical composition established by Atom Probe-data through an Al(Sc,Hf,Zr)-dispersoid in the Al-Hf-Sc-Zr-alloy. The results illustrate that the dispersoids consist of a Sc-rich core, surrounded by an outer shell containing both Hf and Zr.

17 Discussion

17.1 Diffusion of Hf, Sc and Zr – a theoretical approach

As mentioned in the experimental chapter, the alloys were annealed from room temperature, $T_o=20^oC=293K$, to the homogenisation temperature, $T_1=475^oC=748K$, by a heating rate $a=50^oC/hr=1{,}389x10^{-2}K/s$. This non-isothermal heat-treatment makes it necessary to take the time dependence of diffusion coefficients into account. Following Lefebvre et al. (2005), the mean square displacement ($\bar{l}^2$) of solute element X during a time t is given by:

$$\bar{l}^2 = \alpha\left(D^x \cdot t\right) \tag{17.1}$$

where constant α is 6, 4 and 2 for 3D, 2D or 1D diffusion, respectively, and for a small time dt this relationship can be written:

$$d\bar{l}_x^2 = \alpha\left(D^x \cdot dt\right) \tag{17.2}$$

where D^x is the diffusion coefficient of a given solute element X at infinite dilution. D^x is assumed to be constant during dt. The temperature, T, during the 50ºC/h heating ramp can be expressed by the following linear relationship:

$$T = T_o + a\,t \tag{17.3}$$

which in turn can be inserted in the expression for D^x:

$$D^x(t) = D_o^x \cdot e^{\frac{-Q^x}{R(T_o+at)}} \tag{17.4}$$

where Q^x is the activation energy for diffusion of a given element X, while R=8.314 J/K·mol is the universal gas constant. Q^X- and D_o^X-values as reported in the literature can be seen in Table 17.1. By inserting Eq.17.4 into Eq.17.2, the mean square displacement of solute elements

can be found by integration from time, $t_o=0$ (beginning of annealing), to time, t_1, i.e. when the homogenisation temperature, $T_1=475^oC$, is reached:

$$\bar{l}_x^2 = \alpha \int_{t_o}^{t_1} D^x(t) \cdot dt = \alpha \int_{t_o}^{t_1} D_o^x \cdot e^{\frac{-Q^x}{R(T+at)}} \qquad (17.5)$$

By numerically solving equation (17.5), the diffusion lengths of both Sc, Hf and Zr during heating to the homogenisation temperature were found, and the results are plotted in Figure 17.1. These calculations shows that for the given heat treatment procedure only Sc-diffusion will be active in the temperature range 250-350°C. Long range diffusion of Zr or Hf, on the other hand, will not take place to a large extent until 400°C is reached. If α is set to 6 (3D diffusion) the diffusion will start ~50°C earlier than for the general consideration (α=1). In the following, these calculations will be used to explain the effects of the various elements on dispersoid formation.

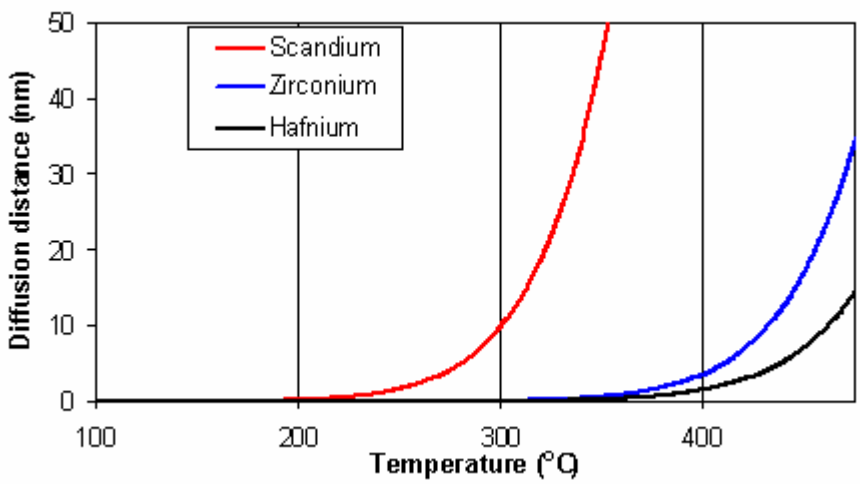

Figure 17.1 Diffusion distances for Sc, Zr and Hf as a function of temperature. The results illustrate that Sc-diffusion is activated at a temperature of ~250°C, while no significant diffusion of Zr and Hf takes place until 400°C is reached.

Table 17.1 D_0 and Q for Sc, Zr and Hf.

Element	$D_o(m^2/s)$	Q(kJ/mol)
$Sc_{(1)}$	$5{,}31 \times 10^{-4}$	173
$Zr_{(2)}$	$7{,}28 \times 10^{-2}$	242
$Hf_{(3)}$	$1{,}07 \times 10^{-2}$	241

(1)Fujikawa (1997), (2) Marumo (1973), (3) Minamino (1987)

17.2 Precipitation kinetics of dispersoids

Clustering/early precipitation: Figures 15.1-15.2 show that precipitation begins at a temperature of ~250^{o}C as both the hardness and conductivity increases significantly at this temperature. Peak hardness was reached at 350ºC for both Al-Sc-Zr and Al-Hf-Sc-Zr and the APFIM-investigations revealed that the strength increase was caused by the formation of a dense distribution of Sc-rich clusters in the α-Al matrix. Very few, if any, Zr- or Hf-atoms were found in these clusters.

These observations are in agreement with the diffusion calculations, as only Sc is able to diffuse below 350°C (see Figure 17.1). Zr- and Hf-diffusion are activated at temperatures above 350ºC, and Zr/Hf will consequently not affect the Sc-clustering. At temperatures below 350ºC, Sc has a relative high diffusion rate and high driving force for nucleation of Sc-rich clusters/dispersoids (see Figure 2.3 in Chapter 2).

The TEM-investigations of the material annealed at 350°C did not allow a clear identification of solute rich dispersoids in the Al matrix. However, diffraction patterns revealed the existence of weak superlattice reflections of the $L1_2$ structure for both alloys, see Figures 16.4 and 16.5. Calculations from the 3D-volume (AP) revealed that the dispersoids/clusters had a stoichiometry close to Al_3Sc with a diameter of ~2.2 nm, see Figures 16.6-16.7

17.2.1 Precipitation of dispersoids at 475^{o}C

The dispersoids grow further as the temperature increases from 350^{o}C to 475˚C. TEM investigations revealed that the average radius of the dispersoids was 2,7nm at 475^{o}C, see Table 16.1.

A very interesting observation is that Hf and/or Zr preferentially segregates to Al_3Sc/matrix interfaces as soon as diffusion of these elements are activated (Figures 16.8-16.11). It has been shown that Zr exhibits a certain solubility in the Al_3Sc-$L1_2$ structure [Toropova (1990), Harada (2002)], and may substitute some of the Sc by occupying the same sub-lattice. As the lattice parameters of the α-Al and Al_3Sc-$L1_2$ structures is 0.4049 nm and 0.4103 nm, respectively [Villars (1985)], the misfit, δ,

between their respective lattices is about 1,3%. The observation of an Ashby-Brown (Coffee bean contrast) contrast in Figure 16.12 indicates that the dispersoids are likely to be coherent with the matrix at the end of the heating ramp, as this contrast is a result of the strain field of the matrix lattice around the dispersoid. The diffraction pattern (SAD) shown in Figure 16.12-16.13, exhibits typical superlattice reflections of the $L1_2$ structure, suggesting that dispersoids are chemically ordered. This observation is consistent with the fact that no relaxation of interface strain is supposed to occur as long as the Al_3Sc-$L1_2$ dispersoids are smaller than 16 nm in radius [Marquis (2001)].

The elastic deformation of the crystal lattice in the vicinity of Al_3Sc dispersoids may significantly influence the diffusion of solute elements in the matrix. Since the average volume available per lattice site close to the dispersoid is different to that in the matrix, the dispersoid exerts a force on solute atoms diffusing in the matrix. This force, designated as $\vec{F}_W^S$, derives from the elastic interaction potential between the interface and solute atoms S in the matrix, and it implies a modified diffusion rate for solute atoms close to the Al_3Sc dispersoids as given by the following expression:

$$\vec{J}_S = -D_S \vec{\nabla} n_S + n_S \cdot \frac{D_S \vec{F}_W^S}{k_B T} \qquad (17.6)$$

where D_S is the diffusion coefficient of the element (Hf or Zr) and n_S is the amount of Hf/Zr atoms per unit volume (cf. Lefebvre et al. (2005)). Since both Hf, Zr (and Sc) atoms have atomic radius larger than Al (see Table 17.2), $\vec{F}_W^S$ will be an attractive force, and as a consequence the presence of the Al_3Sc dispersoids, who will exert an attractive force on Hf- and/or Zr atoms diffusing in their vicinity. It is noticeable that Sc atoms remaining in the matrix are submitted to the same phenomenon, see Table 17.2.

Table 17.2 Atomic radius of some elements [Flinn and Trojan (1975)].

Elements	**Atomic radius (nm)**
Aluminium	0,143
Hafnium	0,159
Scandium	0,160
Zirconium	0,158

It has been reported that the partial substitution of Hf and/or Zr to Sc in the particles leads to a decrease in misfit between the Al and Al_3X (δ) [Harada (2002)], which results in a lower interface energy for the Al_3(Sc,Zr) and Al_3(Hf,Sc,Zr) dispersoids. These observations indicate that it is energetically favourable for Hf and Zr to segregate to the matrix-Al_3Sc dispersoid interfaces as the interfacial energy will then be lowest. It is therefore unlikely that the concentration gradients within the dispersoids will disappear. This also explains why no Hf and Zr-atoms are observed in the core of the particles.

17.2.2 Coarsening/growth

During the isothermal annealing the conductivity increases slightly in Al-Hf-Sc-Zr, see Figure 15.2 This observation is in accordance with the considerable increase in dispersoid volume fraction, *f*, during annealing at 475ºC , see Tables 16.1-16.3. A higher volume fraction normally indicates additional precipitation, but since no "pure" Al_3Zr or Al_3Hf-phases were detected in TEM, a more likely explanation is that the relatively slowly diffusing Hf - and Zr -atoms (and also some Sc) still remaining in the matrix, continue to segregate to the Al_3Sc/matrix-interfaces. Such segregation was also observed during the atom probe investigations, see Figures 16.18 and 16.19 which show an Al_3Sc-core with diameter ~5 nm, surrounded by a progressively thicker Hf -, Sc - and Zr -containing "shell". The dispersoid measurements also indicate this type of coarsening instead of additional dispersoid formation, as the average radius, *r*, and the number density, *N*, were found to increase and significantly decrease, respectively, despite the increase in *f* (Table 16.1-16.3). It is also important to notice that the hardness stabilises for the Al-Hf-Sc-Zr alloy, while the Al-Sc-Zr alloy displays a drop in hardness at 15hrs annealing time at 475°C (see figure 15.1-15.2). Observations in TEM show that the dispersoid size is reduced when Hf is added to these alloys and this may indicate that Hf slows down the dispersoid coarsening. A possible explanation for the slower coarsening, may be that the Hf- addition lowers the Sc-solubility at 475°C, thus preventing Sc from re-entering solid solution. This will in turn ensure a higher recrystallisation resistance in the Al-Hf-Sc-Zr-alloy compared to Al-Sc-Zr.

In order to summarise the duplex structure of dispersoids formed after the complete heat treatment (i.e. heating ramp followed by 15-20 hours isothermal annealing at 475°C) can be explained by combination of diffusion and thermodynamically effects. At 475°C, the growth of dispersoids occurs through the diffusion of Sc, Hf and Zr (and Al in the opposite direction), as it is thermodynamical favourable for these element to segregate to the Al_3Sc/matrix-interfaces. This diffusion results in the formation of a stable Al_3(Hf,Sc,Zr)- or Al_3(Sc,Zr)-compound around the former Al_3Sc particles. However, it has not been possible to provide evidence for a $L1_2$ order in the Hf/Zr rich shell.

18 Conclusions

The various stages of dispersoid formation in Al-Hf-Sc and Al-Hf-Sc-Zr have been studied by quenching samples during homogenisation, and the findings have been compared to recent corresponding results for an Al-Sc-Zr alloy. The general conclusion is that the effect of adding Hf is limited and that Hf to a large extent behaves as Zr, although, with one important exception as pointed out below. More specifically the following conclusions can be made:

- At temperatures below 350ºC, only Sc-diffusion is active. As a consequence the dispersoids first form as Sc-rich clusters homogeneously nucleated in the Al-matrix and Hf does not affect this stage. At 350ºC the Sc-rich phases were found to exhibit the ordered $L1_2$-structure.

- At temperatures above 350˚C, Hf- and Zr-diffusion are activated, and both elements then segregate to the Al_3Sc/matrix interfaces. Elastic strain, related to an Ashby-Brown contrast observed in TEM, is induced by the coherent Sc rich dispersoids,.

- Upon completion of the homogenisation procedure at 475°C, particles consist of an Al_3Sc-$L1_2$ ordered core, surrounded by shells containing both Sc, Zr and Hf. Dispersoid growth is then controlled and limited by Hf or Zr diffusion.

- The addition of Hf to Al-Sc-Zr alloys seems to give a higher density of smaller dispersoids. This may in turn lead to a better

recrystallisation resistance in Hf containing alloys than in Al-Sc-Zr alloys without Hf during and after extrusion. This will be discussed more closely in Part C in the thesis.

From the atom probe and TEM investigations, the different stages of dispersoids formation in the Al-Sc-Zr and Al-Hf-Sc-Zr can be summarised like this:

Super Saturated Solid Solution (SSSS) -> Sc-rich clustering (250^{o}C-300^{o}C) -> Dispersoids with $L1_2$-structure (300^{o}C-475^{o}C) -> Coarsening of dispersoids (at 475^{o}C).

19 References

Davydov, V.G., Elagin, V.I., Zakharov, V.V., Rostov, T.D., Met.Sci. Heat Treat., Vol.38, p.347, 1996

Desch, PB, Schwarz RB, Nash, P, J. Less-Common Met., Vol. 168, p. 69, 1991

Drits, ME, Dutkiewicz, J., Toropova, LS, Salawa, J, Crystal Res. Technol., Vol. 19, p.1325, 1984

Forbord, B., Hallem, H., Ryum, N., Marthinsen, K., Mater. Sci. Eng. A, 387-389, p.936, 2004a

Forbord, B., Hallem, H., Marthinsen, K., Mater. Sci. Forum, 467-470, p.369, 2004b

Forbord, B., Lefebvre, B., Danoix, F., Hallem, H., Marthinsen, K., Scripta Mat., Vol. 51, 4, p.333, 2004c

Flinn, R.A., and Trojan, P.K., Engineering Materials and Their Applications, Houghton Mifflin Company, Boston, 1975

Fujikawa, S.I., Defect and Diffusion Forum, 143-147, pp.115-120, 1997

Hallem, H., Forbord, B., Marthinsen, K., ICAA9, Brisbane, Australia 2004a

Hallem, H., Forbord, B., Marthinsen, K., ICAA9, Brisbane, Australia, 2004b

Harada, Y., Dunand, D.C., Mater. Sci. Eng., Vol. A329-331, p. 686, 2002

Heinrich, A., Al Kassab, T., Kirchheim, R., Mat. Sci. Eng. A, Vol.353, p.92, 2003

Humphreys, F.J., and Hatherly, M., *Recrystallization and Related Annealing Phenomena*, Pergamon Press, Oxford, 1995

Hyland, R.W., Met. Trans. A, 23A, p.1947, 1992

Part B

Jones, A.R., Ralph, B., Hansen, N., Met. Sci. 13, p.140, 1979

Lefebvre, W., Danoix, F., Hallem, H., Forbord, B., Bostel, A., Marthinsen, K., To be published in Acta Mat, 2005

Marquis, E.A., Seidman, D.N., Acta Mater., Vol. 49, p.1909, 2001

Marumo, T., Fujikawa, S., Hirano, K-I., J. Japan Inst. Light Metals. Vol. 23, no.1, pp.17-25. 1973

Minamino, Y., Yamane, T., Nakagawa, S., Araki, H., Hirao, K-I., J. Jpn. Inst. Light Met. Vol. 37, no.1, pp.72-82. 1987

Nes, E., Acta Met., 20, p. 499, 1972

Riddle, Y.W., PhD-thesis, Georgia Institute of Technology, 2000

Robson, J.D., Jones, M.J., Prangnell, P.B., Acta mater., 51, p.1453, 2003

Rostova, T.D., Davydov, V.G., Yelagin, V.I., Zakharov, V.V., Mater. Sci. Forum, 331-337, p.793, 2000

Toropova, L.S., Kamardinkin, A.N., Kindzhibalo, V.V., Tyvanchuk, A.T., Met. Metall., Vol. 70, p.106, 1990

Toropova, L.S., Eskin, D.G., Kharaterova, L., Bobatkina, T.V., Advanced aluminium alloys containing scandium – Structure and properties, Gordon and Breach Sciences, Amsterdam, 1998

Vaumousse, D., Cerezo, A., Warren, P., Ultramic., Vol. 95, p.215, 2003

Villars, P., Calvert, L.D., *Pearson's Handbook of crystallography data for intermetallic phases,* ASM, Metal Park, OH, 1985

Zakharov, V.V., Met.Sci. Heat Treat., Vol. 39, p.61, 1997

Zener, C., quoted by Smith, C.S., Trans. AIME 175, p.47, 1948

Part B

Part C : Extrusion, cold rolling and annealing of aluminium alloys with additions of hafnium, scandium and zirconium.

20 Introduction Part C

After the initial investigations presented in Part A and B, six different alloys with various Hf, Sc and Zr-content were chosen for further studies. The objective of this part has been to study the effect of dispersoids on recrystallisation resistance in the material during extrusion, and also during annealing after cold rolling of the extruded profiles. The results presented in Part C are divided into three chapters:

- **Casting and extrusion:** In this chapter the as cast, homogenised and as extruded microstructure will be shown. The extrusion parameters as force and temperature will also be presented.

- **High temperature annealing of the extruded profiles:** In this chapter the microstructure and dispersoid distribution in the extruded profiles has been studied after annealing at different times and temperatures.

- **Cold rolling of extruded profiles:** In the last chapter the microstructure of profiles cold rolled to various degrees of deformation have been studied after annealing.

21 Experimental

Casting and chemical composition. The alloys were made as explained in Chapter 4 and the microstructure can be seen in Appendix. The composition of the alloys were determined by microprobe equipped with WDS (Wavelength Dispersive Spectrometry), see Table 21.1. The results were also compared with a spark spectrograph (unable to measure Hf or Sc), and XRF (X-Ray Fluorescence). All the different techniques used in the analysis of the chemical composition (XRF, WDS and spectrograph) gave virtually similar results. The compositions found in WDS were chosen since all elements can be measured by this method.

Table 21.1 Chemical composition of the alloys.

Alloy	Hf	Sc	Zr	Si	Fe	Al
1	0,61	-	-	0,14	0,15	Bal
2	0,46	-	0,10	0,13	0,19	Bal
3	0,52	0,16	-	0,16	0,21	Bal
4	0,51	0,16	0,06	0,14	0,22	Bal
5	0,54	0,17	0,14	0,16	0,18	Bal
6	-	0,18	0,22	0,16	0,23	Bal

WDS: Microprobe, Wavelength Dispersive Spectrometry. All given in wt%

Homogenisation. All alloys were homogenised as seen in Table 21.2. A heating rate of 50^{o}C/hr was applied. Further details can be seen in Chapter 4.3. A longer annealing time at 475^{o}C was applied for the alloys without Sc additions because Hf and Zr are slow diffusing elements and need more time to precipitate than Sc containing alloys.

Table 21.2 Overview of homogenisation times for the different alloys

Alloy	Ramping	Annealing at 475^{o}C
1 and 2	50 C/hr	20 hr
3,4,5 and 6	50 C/hr	5 hr

Extrusion. The samples were then extruded and investigated. Details are listed in Chapter 4.5

Annealing. Annealing after extrusion was performed in a salt bath, see Chapter 4.6

Microscopy. The samples were investigated by optical microscopy and transmission electron microscopy. See Chapter 4.7 concerning microscopy and dispersoid measurements.

Electron backscatter diffraction: The procedure for EBSD measurements are presented in Chapter 4.7.2

Cold rolling and annealing: Alloys 2-6 were cold rolled after extrusion according to rolling reductions given in Table 21.3. In order to investigate the structural stability, i.e. recrystallisation resistance, samples were cut from the cold rolled material and flash-annealed (from RT) in salt bath for 1hr at 600^{o}C (c.f. Chapter 4.4).

Table 21.3 Measured thickness and actual reduction in % of the samples

Alloy	As extr.	10%		20%		50%		80%	
	mm	mm	act. %	mm	act. %	Mm	act. %	mm	act. %
2	1,82	1,64	9,9	1,36	25,4	0,87	52,3	0,37	79,5
3	1,83	1,57	14,2	1,37	25,0	0,92	49,6	0,39	78,5
4	1,81	1,66	8,0	1,35	25,5	0,85	53,0	0,39	78,6
5	1,83	1,66	9,4	1,35	26,0	0,90	50,8	0,38	79,4
6	1,82	1,68	7,7	1,37	24,7	0,88	51,5	0,38	79,1

22 Casting and extrusion of the alloys

The dendrite/grain structure and micro-segregation influence the precipitation behaviour during subsequent annealing. These micro-structural features have consequently been investigated and will be presented in the following.

22.1 As cast structures

Table I in the Appendix shows the grain size at the top and the bottom of the ingot in the ND direction. The variation is large and as discussed in Chapter 4, the top and the bottom are cut off to get a more homogeneous structure used for extrusion. The micrographs of the top and bottom of the ingot can also be seen in the Appendix. No micrographs of the microstructure from the middle of the ingot are available, because this material was used for extrusion.

22.2 Homogenisation

Microsegregations of Hf, Sc, Zr, Si and Fe in both the as cast and homogenised variants were investigated by performing line-scans across dendrites/grains by means of microprobe. The results for alloys 1, 4 and 6 are given in Figures 22.1-22.6, where the vertical lines indicate the grain boundaries.

These figures show that the concentration of Hf and Zr in the as cast material are highest in the grain centre and decreases towards the boundaries. Sc, Si and Fe, however, were found to segregate to the grain boundaries. Homogenisation of the alloys did not remove the core gradients in alloys 1-5.

An interesting observation was that all Hf-containing alloys displayed a cell structure. However, when Hf was not present, no such cell structure was detected (Figures 22.5-22.6).

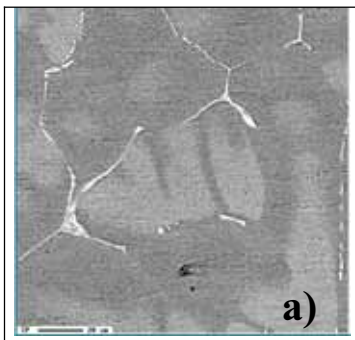

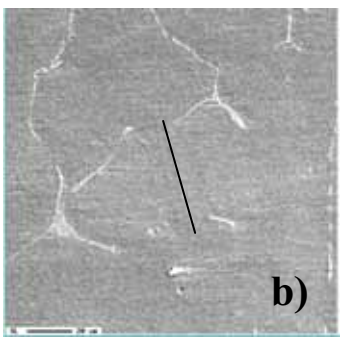

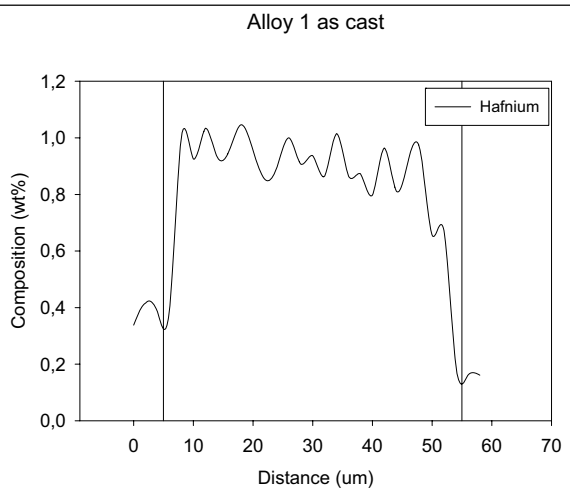

c)

Figure 22.1 Segregation variations in the as cast conditions of alloy 1. a) BE image and b) SE image obtained in the microprobe c) Line scan corresponding to the black line in b).

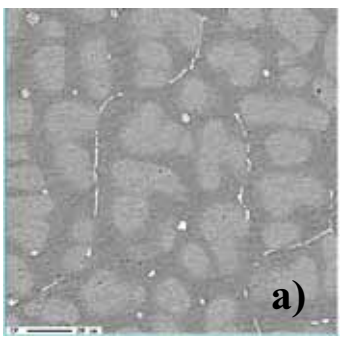

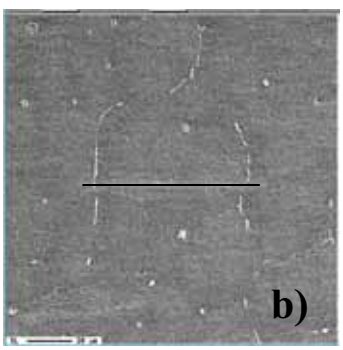

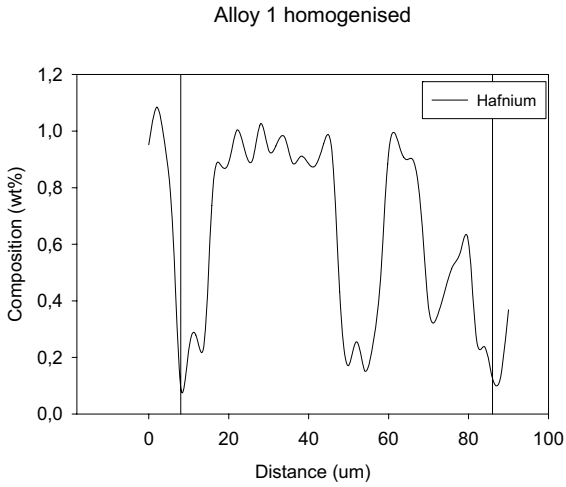

c)

Figure 22.2 Segregation variations in the homogenised conditions of alloy 1. a) BE image and b) SE image obtained in the microprobe c) Line scan corresponding to the black line in b).

BE: Backscatter electrons, SE: Secondary electrons.

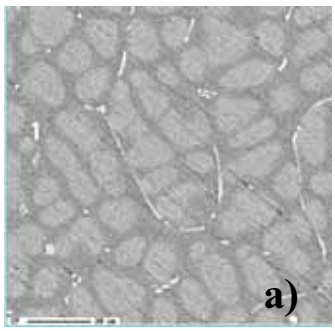

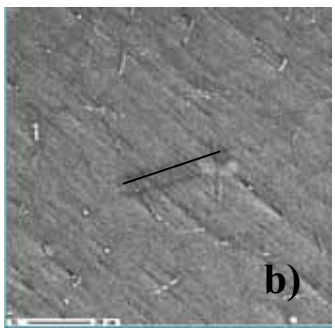

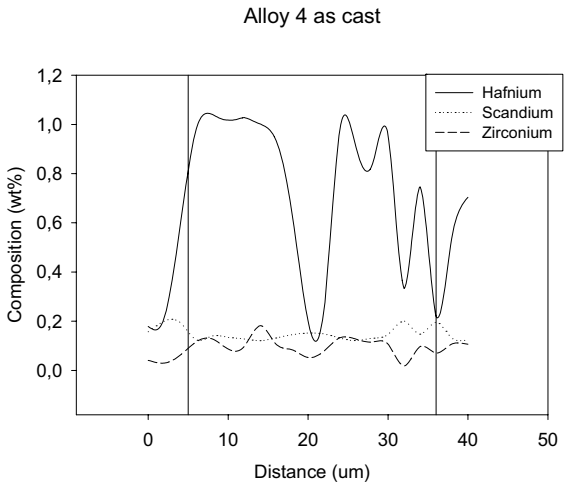

c)

Figure 22.3 Segregation variations in the as cast conditions of alloy 4. a) BE image and b) SE image obtained in the microprobe c) Line scan corresponding to the black line in b).

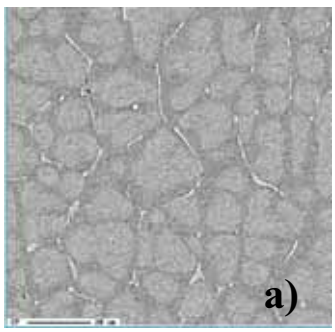

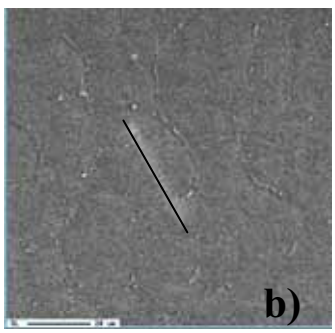

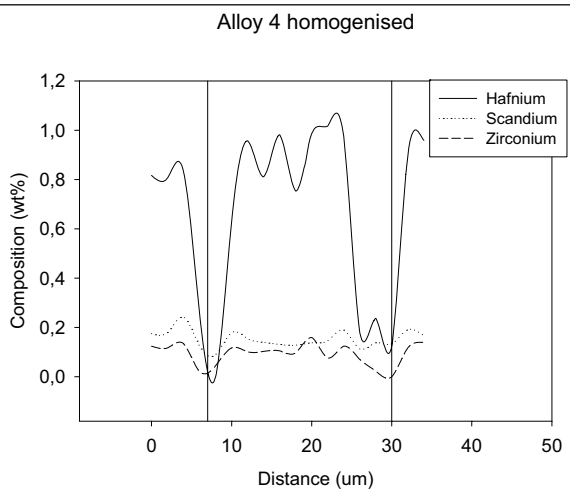

c)

Figure 22.4 Segregation variations in the homogenised conditions of alloy 4. a) BE image and b) SE image obtained in the microprobe c) Line scan corresponding to the black line in b).

BE: Backscatter electrons, SE: Secondary electrons.

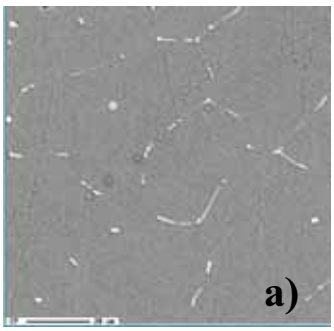

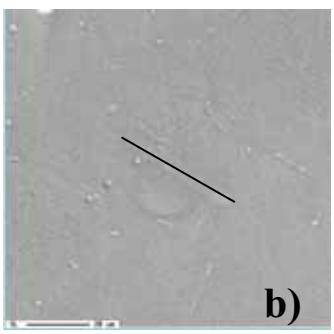

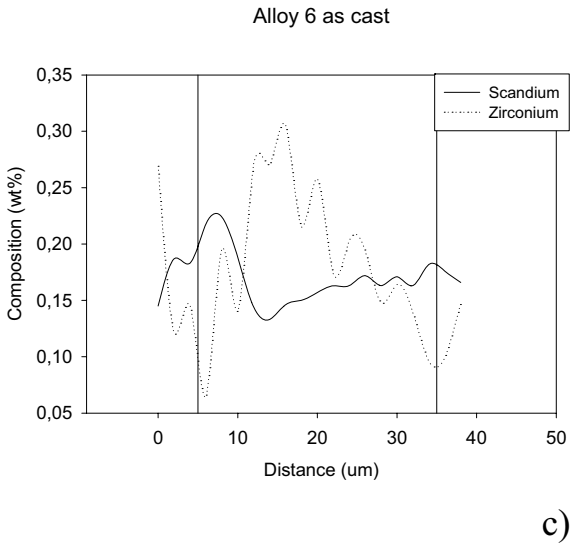

c)

Figure 22.5 Segregation variations in the as cast conditions of alloy 6. a) BE image and b) SE image obtained in the microprobe c) Line scan corresponding to the black line in b).

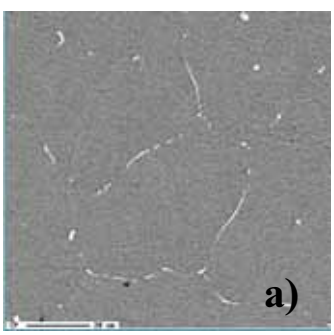

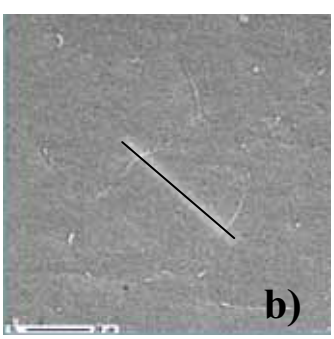

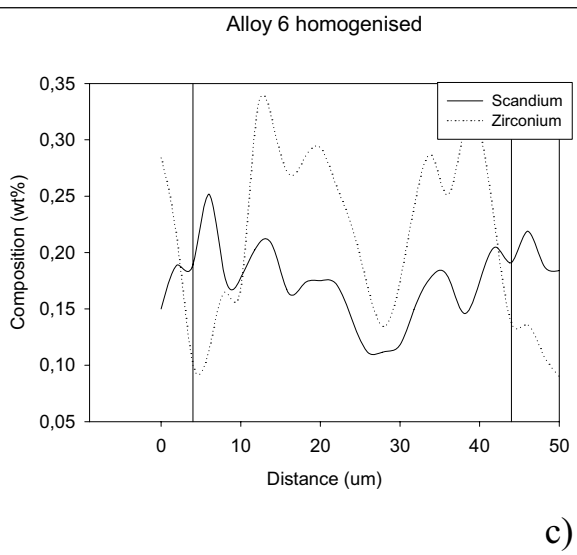

c)

Figure 22.6 Segregation variations in the homogenised conditions of alloy 6. a) BE image and b) SE image obtained in the microprobe c) Line scan corresponding to the black line in b).

BE: Backscatter electrons, SE: Secondary electrons.

22.3 Extrusion

22.3.1 Extrudability

Table 22.1 shows that the maximum temperature as measured in the die bearing during extrusion varies between 533°C and 579°C, and that the extrusion force varies between 2562 kN and 4216 kN for the alloys. The maximum extrusion force generally increases with the amount of Hf, Sc and Zr as these elements form dispersoids, which increases the deformation resistance of the alloy. However, alloy 5 has a slightly lower extrusion force probably due to primary particles (AlHfScZr) which consume alloying elements in the alloy. Figure 22.7 shows the variation in ram force for the different alloys during extrusion.

Table 22.1 Extrusion parameters.

Alloy	Max temp. (°C)	Max extr. Force (kN)	Extr. speed (mm/s)	Pre-heating of billett (°C)
1.Al-Hf-Si-Fe	533	2562	6,1	477
2.Al-Hf-Zr-Si-Fe	552	2926	6,1	480
3.Al-Hf-Sc-Si-Fe	572	3886	6,1	475
4.Al-Hf-Sc-Zr-Si-Fe	578	4216	6,1	480
5.Al-Hf-Sc-Zr-Si-Fe	579	3709	6,1	485
6.Al-Sc-Zr-Si-Fe	579	3950	6,1	484

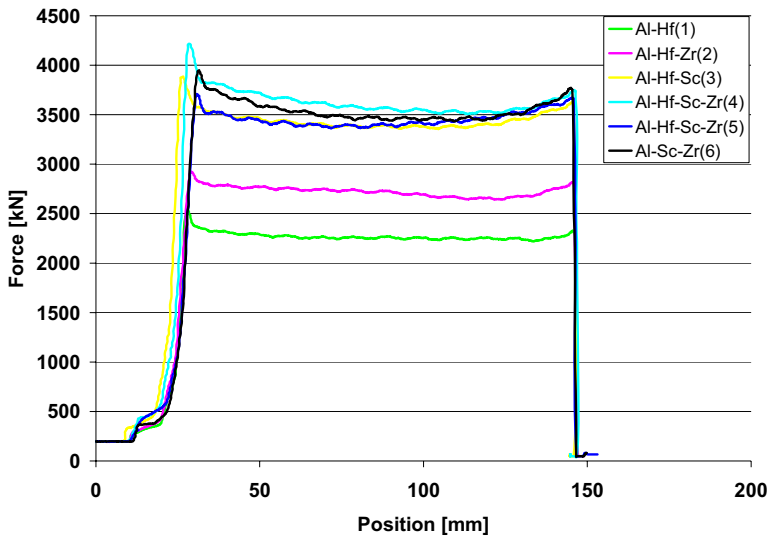

Figure 22.7 Extrusion force, as function of ram position for all the alloys.

22.3.2 As extruded microstructure

While alloy 1 recrystallised completely during extrusion, alloys 2-6 displayed a fibrous microsructure without any signs of recrystallisation. Furthermore, coarse primary particles (10-30µm) were observed in alloys 4-5. These particles were found to have a composition of approximately ~50wt%Hf-15wt%Zr-2wt%Sc, see Figure 22.8.

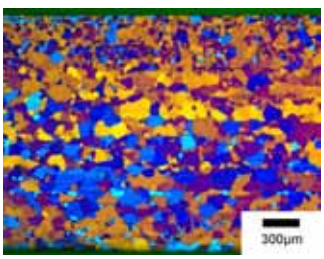

a) Al-Hf-Si-Fe (alloy 1)

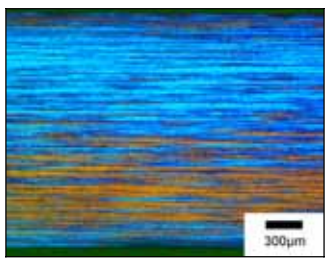

b) Al-Hf-Zr-Si-Fe (alloy 2)

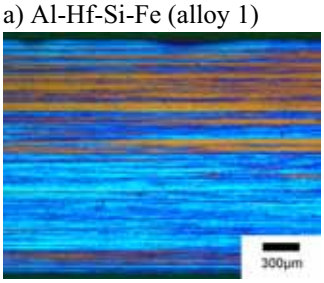

c) Al-Hf-Sc-Si-Fe (alloy 3)

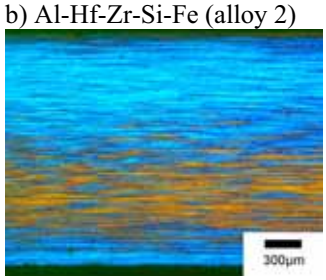

d) Al-Hf-Sc-Zr-Si-Fe (alloy 4)

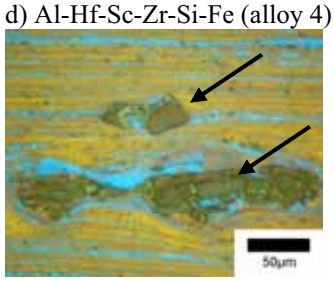

e) Al-Hf-Sc-Zr-Si-Fe (alloy 4)

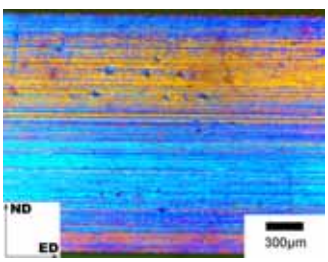

f) Al-Hf-Sc-Zr-Si-Fe (alloy 5)

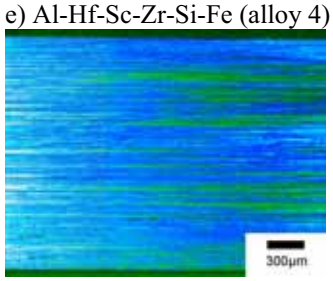

g) Al-Sc-Zr-Si-Fe (alloy 6)

Figure 22.8 Micrographs of the as extruded profiles showing the microstructure of the alloys. Image e) shows coarse primary particles in alloy 4 (indicated by arrows).

22.3.3 Dispersoids in the as extruded material

Recrystallisation does not take place in alloys 2-6 due to a high density of dispersoids, see Figures 22.9a-e. EDS/TEM revealed that the dispersoids were of the type Al_3(Hf,Zr) in alloy 2, Al_3(Hf,Sc) in alloy 3, Al_3(Hf,Sc,Zr) in alloys 4-5 and Al_3(Sc,Zr) in alloys 6.

An interesting observation is that the width of the dispersoid size distribution decreases when Sc and Zr are added in combination (alloy 4-6). This indicate that the Al_3(Hf,Sc,Zr) and Al_3(Sc,Zr) dispersoids nucleate almost simultaneously. The results are given in Table 22.2 and Figure 22.10.

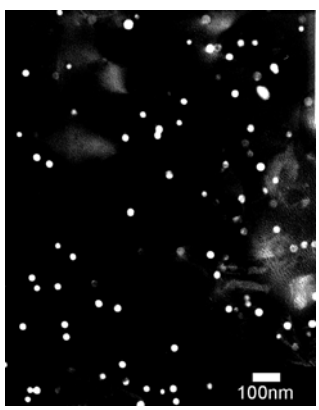

a) Al-Hf-Zr-Si-Fe (2)

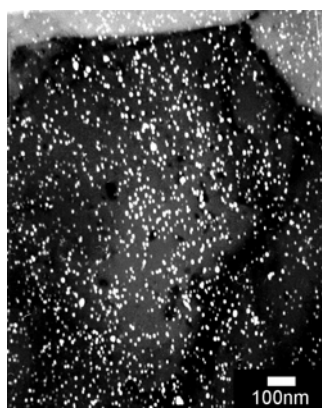

b) Al-Hf-Sc-Si-Fe (3)

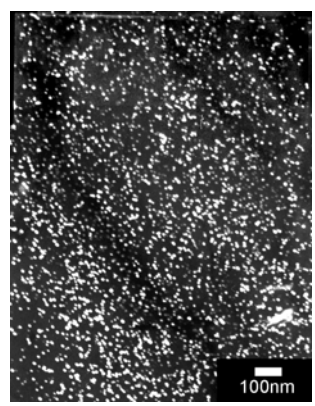

c) Al-Hf-Sc-Zr-Si-Fe (4)

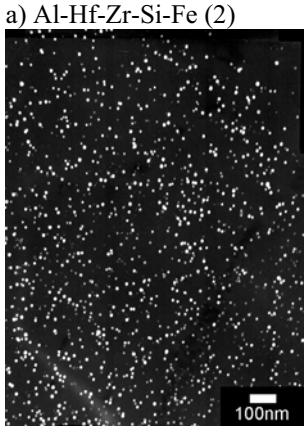

d) Al-Hf-Sc-Zr-Si-Fe (5)

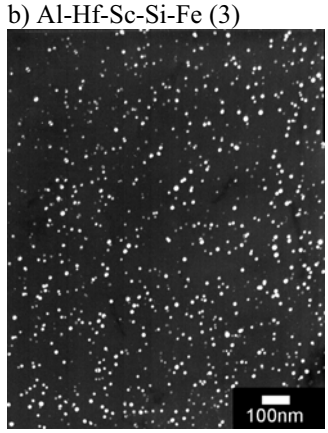

e) Al-Sc-Zr-Si-Fe (6)

Figure 22.9 Dark Field TEM micrographs of dispersoids (white spots) in a) Al_3(Hf,Zr) b) Al_3(Hf,Sc) c) Al_3(Hf,Sc,Zr) d) Al_3(Hf,Sc,Zr), and e) Al_3(Sc,Zr) in the as extruded condition.

Table 22.2 Average radius, maximum density and volume fraction of dispersoids in the different alloys after extrusion.

Alloy	**Average radius/ St.dev**	**Max Density [m^{-3}]**	**Average Density [m^{-3}]**	**Average volume fraction**	**f/r [10^{-3}]**
1.Al-Hf-Si-Fe	Too few to measure	-	-	-	-
2.Al-Hf-Zr-Si-Fe*	14nm/4nm	2,5E+21	9,1E+20	-	-
3.Al-Hf-Sc-Si-Fe	9nm/3nm	1,1E+22	4,5E+21	1,2E-02	1,3
4.Al-Hf-Sc-Zr-Si-Fe	7nm/1nm	1,7E+22	1,4E+22	2,1E-02	3,0
5.Al-Hf-Sc-Zr-Si-Fe	6nm/1nm	1,0E+22	8,8E+21	7,5E-03	1,3
6.Al-Sc-Zr-Si-Fe	7nm/1nm	5,6E+21	4,9E+21	5,9E-03	0,8

*Due to the heterogeneous distribution, the average volume fraction of dispersoids in this variant was not measured.

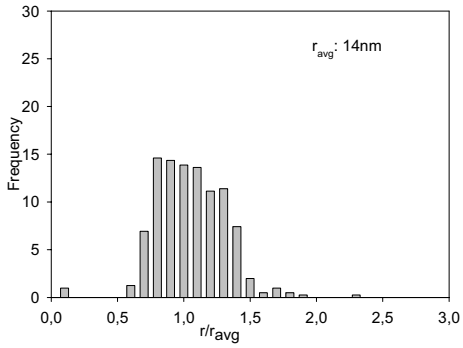

a) $Al_3(Hf,Zr)$ dispersoids, alloy 2.

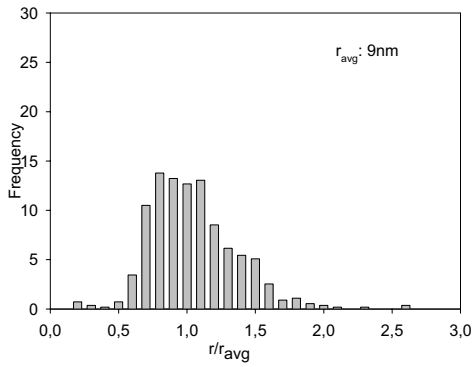

b) $Al_3(Hf,Sc)$ dispersoids, alloy 3.

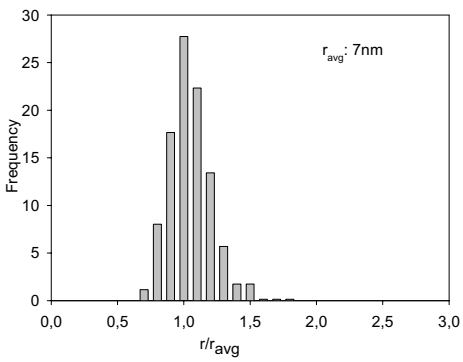

c) $Al_3(Hf,Sc,Zr)$ dispersoids, alloy 4.

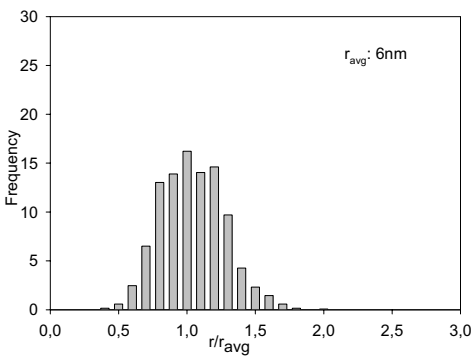

d) $Al_3(Hf,Sc,Zr)$ dispersoids, alloy 5

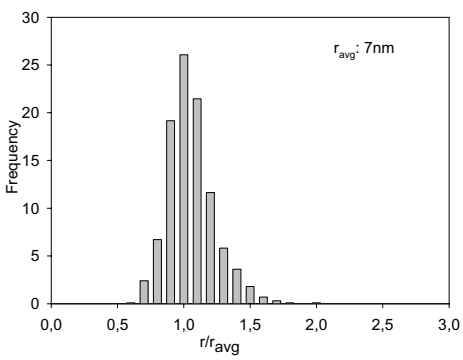

e) $Al_3(Sc,Zr)$ dispersoids, alloy 6.

Figure 22.10 Particle size distributions for alloys 2-6.

23 High temperature annealing of the as extruded alloys

23.1 Microstructure evolution after annealing of extruded profiles

The recrystallisation resistance of alloy 2-6 was investigated, by annealing the extruded variants for different times at temperatures between 500^{o}C-600^{o}C in salt bath (Figures 23.1-23.3).

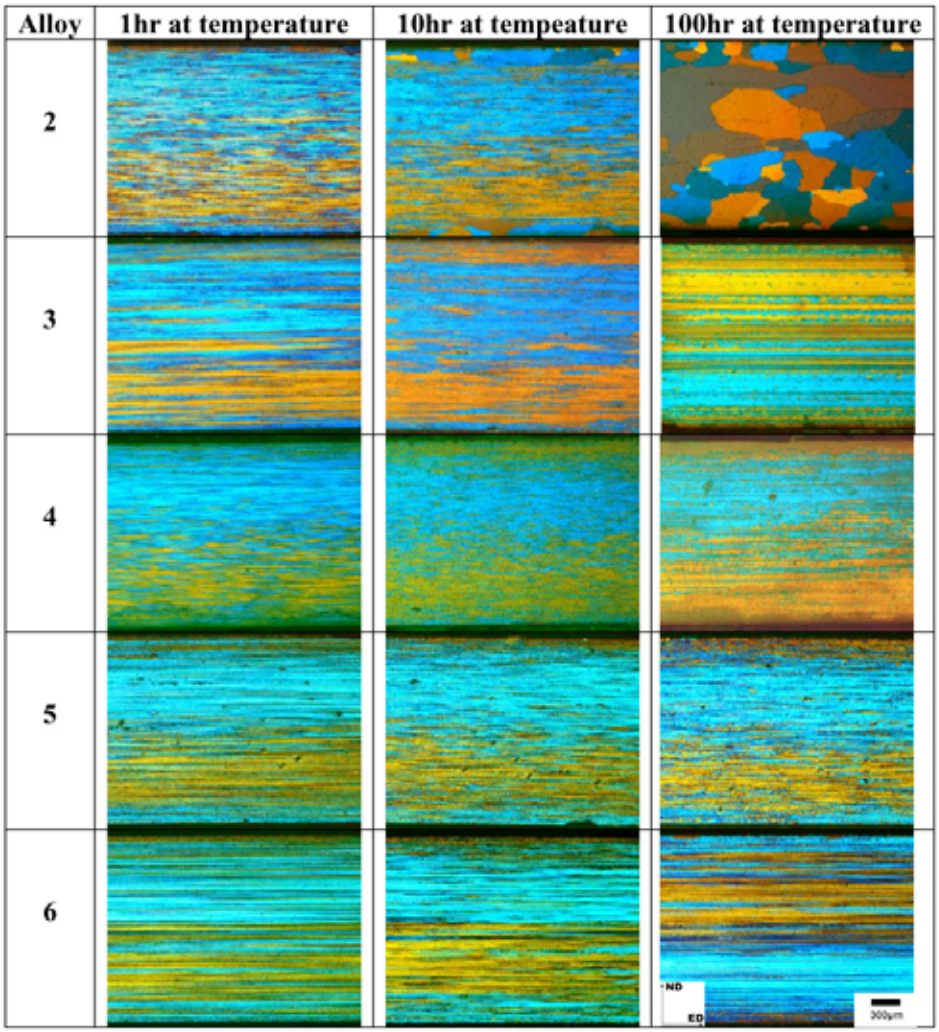

Figure 23.1 Microstructure in alloys 2-6 annealed for 1-100hrs at 500°C

Apart from alloy 2, all variants resist recrystallisation at 500°C even after 100hrs annealing. Alloy 2, on the other hand, begins to recrystallise in the surface of the profile after 10 hrs, and was completely recrystallised after 100hrs.

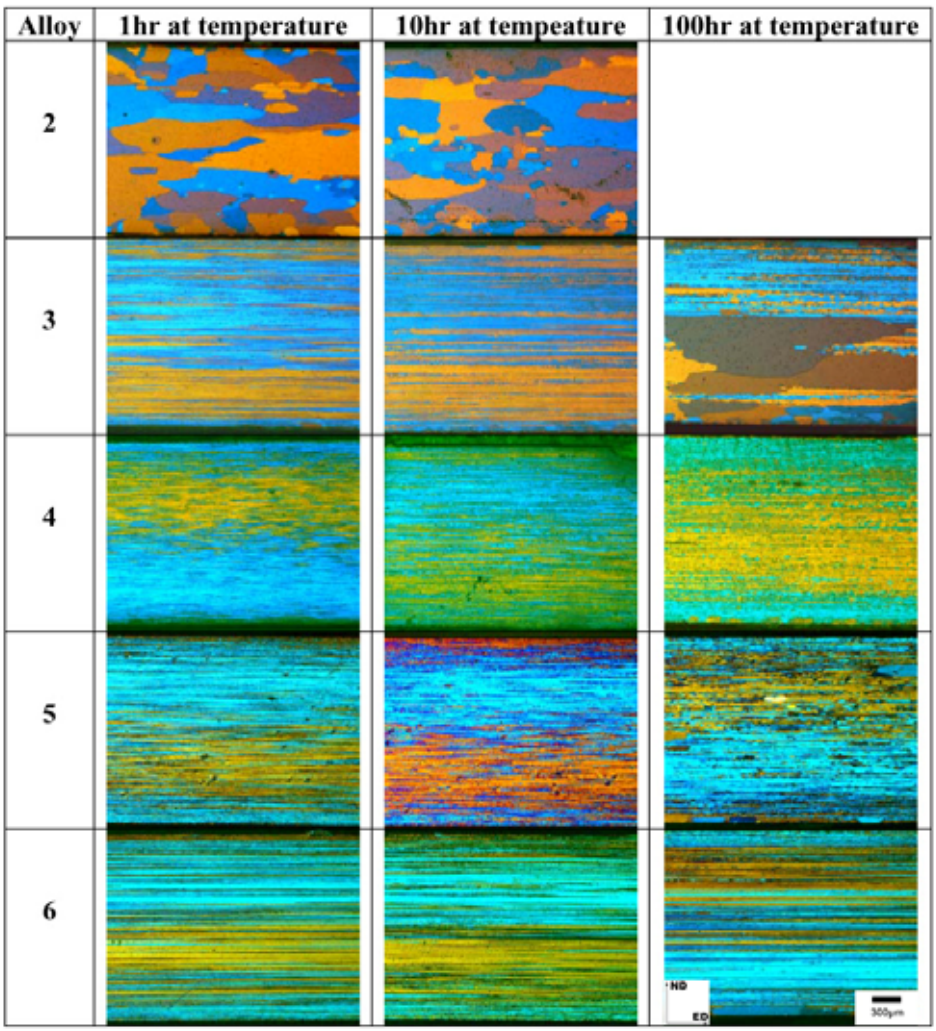

Figure 23.2 Microstructure in alloys 2-6 annealed for 1-100hrs at 550°C

When the temperature is increased to 550°C, alloy 2 recrystallises already after 1hr. In alloy 3 a thin recrystallised surface layer was observed after 10 hr, while 100 hrs annealing resulted in an almost completely recrystallised structure. The other variants displayed a remarkable recrystallisation resistance. However, in both alloys 5 and 6 some randomly positioned recrystallised grains were observed in the surface of the profile.

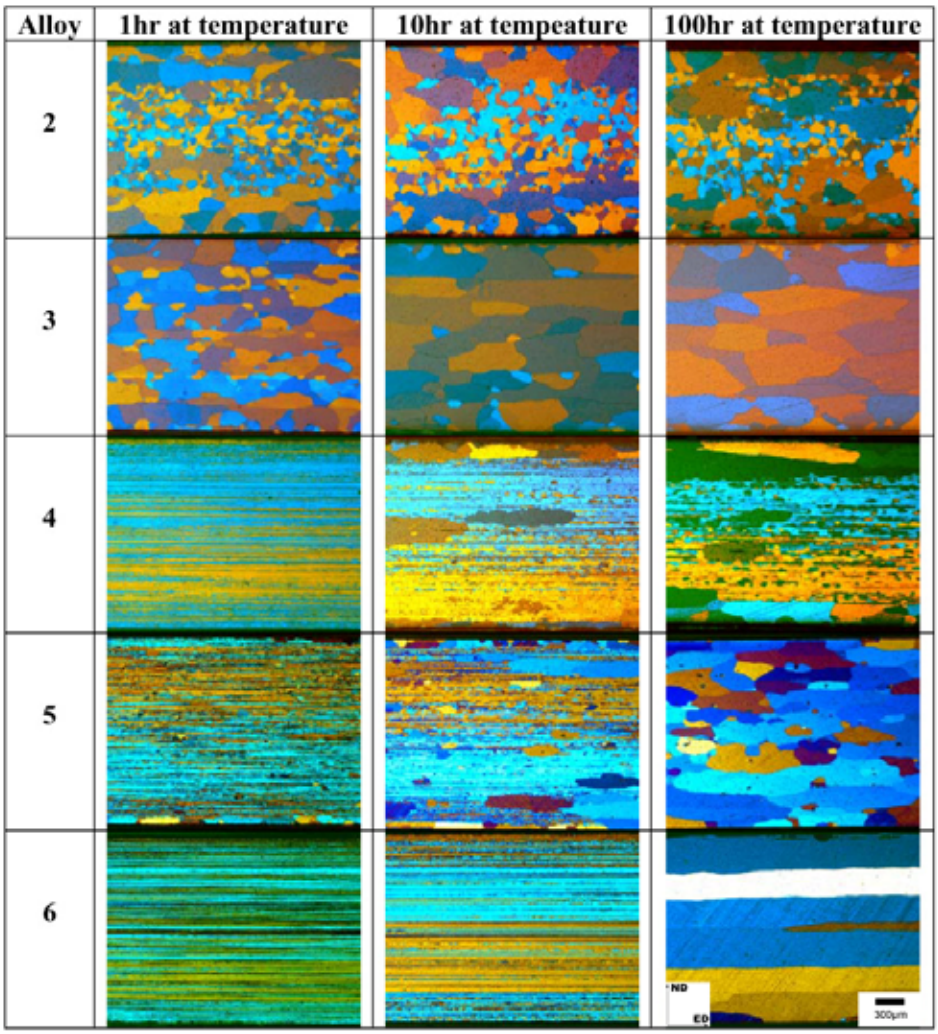

Figure 23.3 Microstructure in alloys 2-6 annealed for 1-100 hrs at 600°C

When the temperature was raised to 600°C, alloys 2 and 3 were recrystallised completely after 1hr annealing time. Alloys 4 and 6 still displayed a fibrous structure, while a thin recrystallised surface layer was observed in alloy 5. In alloy 6 this remarkably high resistance towards recrystallisation was maintained even after 10hrs annealing at 600°C. However, after 100hrs it recrystallised completely, displaying very coarse grains. Alloys 4 and 5 displayed recrystallised grains randomly distributed through the thickness of the profile after 10 hrs. 100 hrs annealing resulted in complete recrystallisation of alloy 5. However, the most remarkable observation during this investigation was that alloy 4

mainly displayed a fibrous structure even after 100 hrs annealing. Only a few recrystallised grains were observed, and practically all of these grains were connected to coarse primary particles which had formed in the material during solidification, see Figure 23.4 which shows a similar phenomena (PSN) in alloy 5.

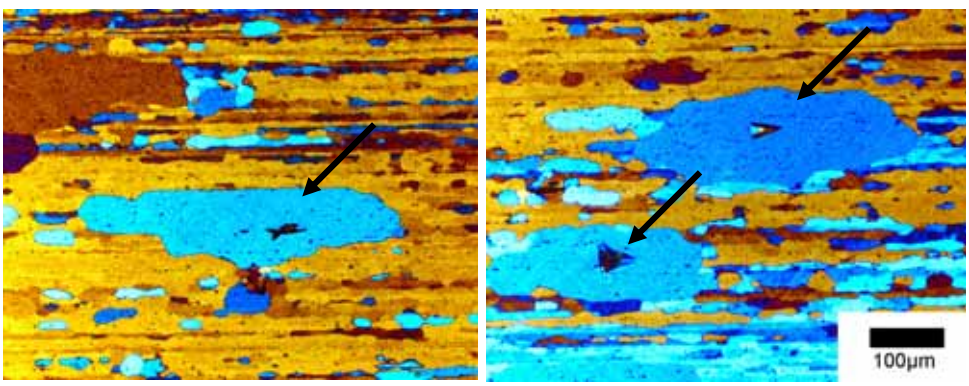

Figure 23.4 Anodised samples from alloy 5 heated at 600°C at 10 hr showing primary particles inside the recrystallised grains, indicated by arrows.

Table 23.1 gives an overview of the results for all the alloys (1hr at different temperatures). Alloys 4, 5 and 6 are all unrecrystallised even after 1hr at 600°C, while alloy 4 and 5 displayed a thin recrystallised surface layer.

Table 23.1 Recrystallisation behaviour of the different alloys, 1hr at temperature.

Alloy	Homogenisation	Temperature	Microstructure
1.Al-Hf-Si-Fe	50C/hr +20hr at 475C	As extruded 500°C 550°C 600°C	Recrystallised - - -
2.Al-Hf-Zr-Si-Fe	50C/hr +20hr at 475C	As extruded 500°C 550°C 600°C	Unrecrystallised Unrecrystallised Recrystallised Recrystallised
3.Al-Hf-Sc-Si-Fe	50C/hr +5hr at 475C	As extruded 500°C 550°C 600°C	Unrecrystallised Unrecrystallised Unrecrystallised Recrystallised
4.Al-Hf-Sc-Zr-Si-Fe	50C/hr +5hr at 475C	As extruded 500°C 550°C 600°C	Unrecrystallised Unrecrystallised Unrecrystallised Surface Recrystallised
5.Al-Hf-Sc-Zr-Si-Fe	50C/hr +5hr at 475C	As extruded 500°C 550°C 600°C	Unrecrystallised Unrecrystallised Unrecrystallised Surface Recrystallised
6.Al-Sc-Zr-Si-Fe	50C/hr +5hr at 475C	As extruded 500°C 550°C 600°C	Unrecrystallised Unrecrystallised Unrecrystallised Unrecrystallised

23.2 EBSD investigations and mechanical properties

A well known problem during extrusion of aluminium alloys is the formation of recrystallised layers in the surface. As a consequence the substructure evolution in the surface regions usually cannot be investigated. However, this is possible in alloys 4-6 due to their high recrystallisation resistance. The unrecrystallised surface structure also opens for possibility of comparing the sub-grain and dispersoid structure in the middle and surface regions after extrusion. Both the temperature and the deformation conditions vary strongly from the middle to the surface of the profiles, which, in turn, will affect the stored energy and precipitation conditions during subsequent heat treatment.

Figures 23.5-23.10 show the orientation imaging maps (OIM, high angle grain boundaries appear black while low angle grain boundaries are white) of the microstructures of samples of alloys 4, 5 and 6 as extruded and annealed for 30 sec, 5 and 60 minutes, respectively at 600°C. The measurements of subgrain sizes are listed in Table 23.2. The subgrain size of alloys 4 and 6 after 60min at 500°C are also listed in Table 23.2

Table 23.2 Development of the substructure after annealing at 500°C and 600°C measured by EBSD where all the sub-grain sizes are given in μm.

Alloy	As extruded	30 sec at 600°C	5 min at 600°C	60 min at 600°C	60 min at 500°C
4.middle	0,9	2,3	3,3	3,3	1,9
4.surface	0,8	1,5	2,6	3,0	1,9
5.middle	0,8	1,5	2,9	3,5	-
5.surface	0,9	2,1	7,7	REX	-
6.middle	0,7	1,4	2,0	3,1	2,0
6.surface	0,9	1,3	1,8	2,6	1,5

REX: recrystallised structure.
Profile thickness was 1,9mm.

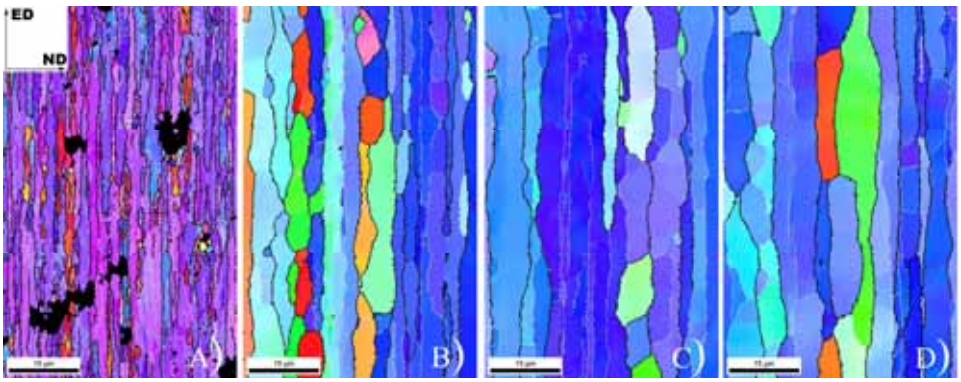

Figure 23.5 OIM images from the middle of alloy 4, heat-treated at 600°C. a) as extruded, b) 30sec at temperature, c) 5min at temperature and d) 60min at temperature.

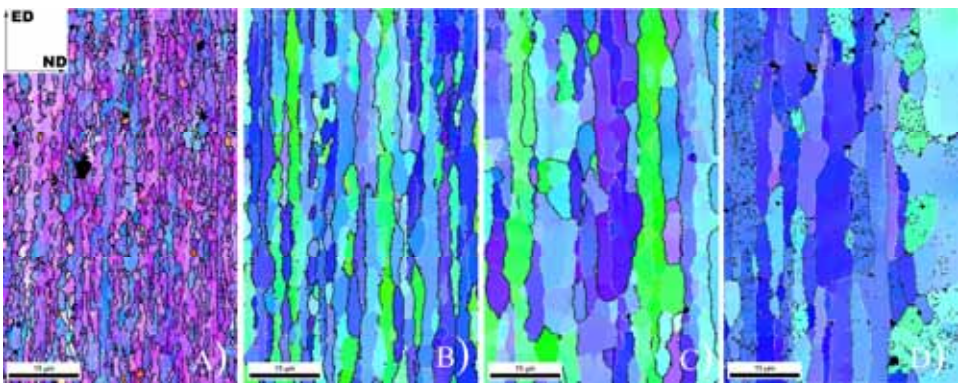

Figure 23.6 OIM images from the surface of alloy 4, heat-treated at 600°C. a) as extruded, b) 30sec at temperature, c) 5min at temperature and d) 60min at temperature.

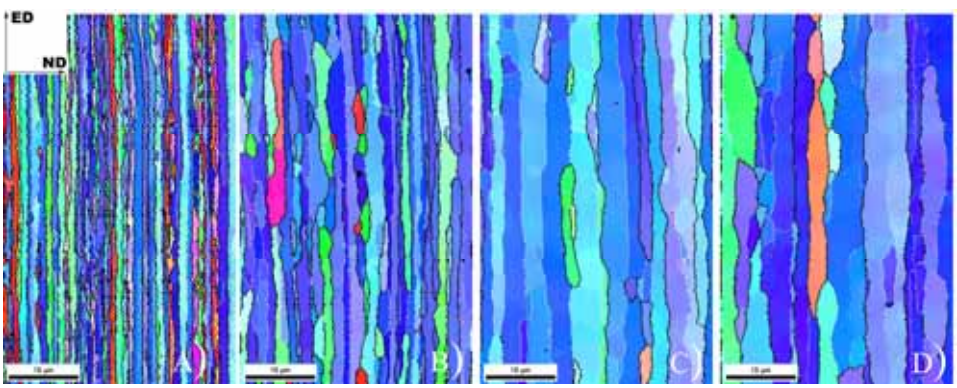

Figure 23.7 OIM images from the middle of alloy 5, heat-treated at 600°C. a) as extruded, b) 30sec at temperature, c) 5min at temperature and d) 60min at temperature.

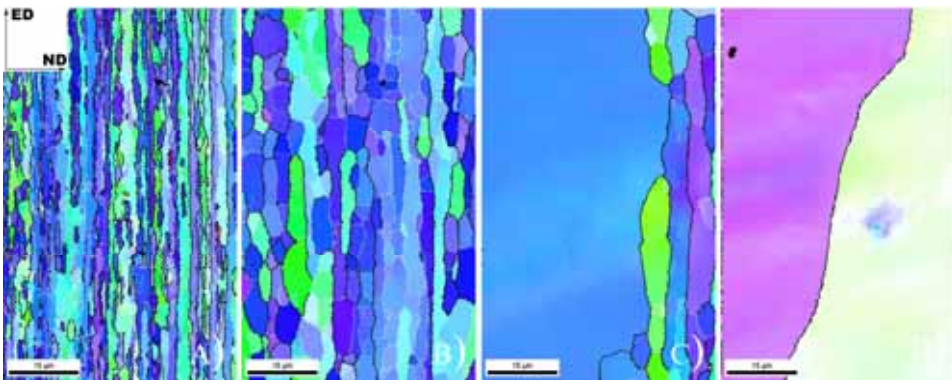

Figure 23.8 OIM images from the surface of alloy 5, heat-treated at 600°C. a) as extruded, b) 30sec at temperature, c) 5min at temperature and d) 60min at temperature.

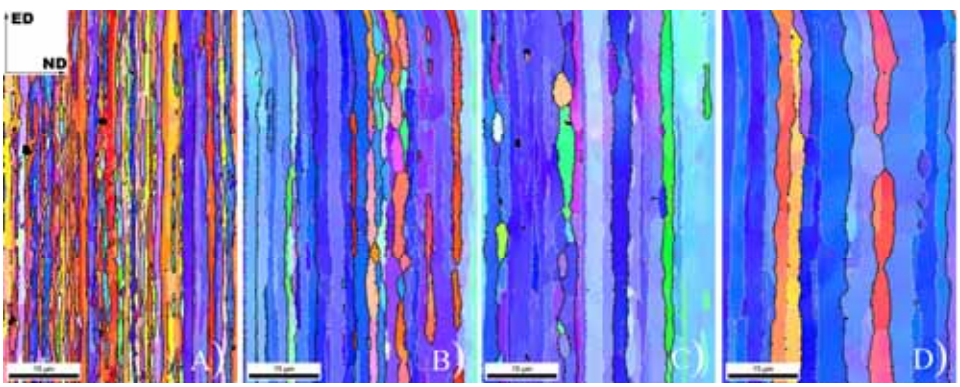

Figure 23.9 OIM images from the middle of alloy 6, heat-treated at 600°C. a) as extruded, b) 30sec at temperature, c) 5min at temperature and d) 60min at temperature.

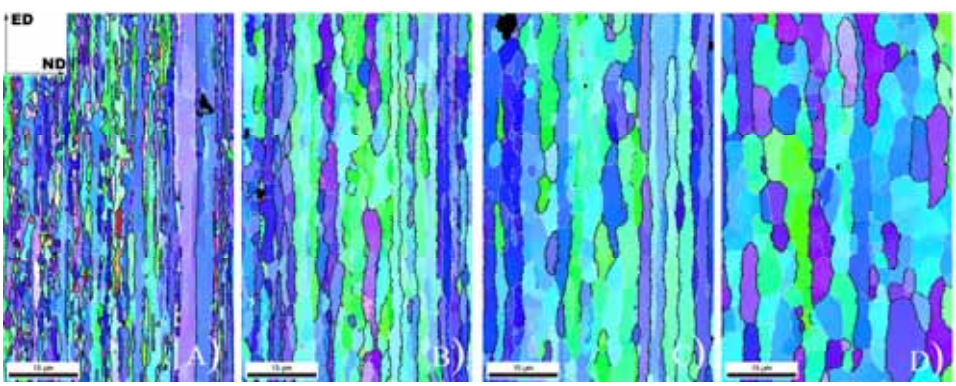

Figure 23.10 OIM images from the surface of alloy 6, heat-treated at 600°C. a) as extruded, b) 30sec at temperature, c) 5min at temperature and d) 60min at temperature.

23.2.1 Variation in subgrain size

Figure 23.11 illustrate the difference in subgrain size between the surface and middle regions. The edge of the profile clearly shows smaller subgrains compared to those found in the middle. The measurements of the as extruded samples were obtained in the ND direction.

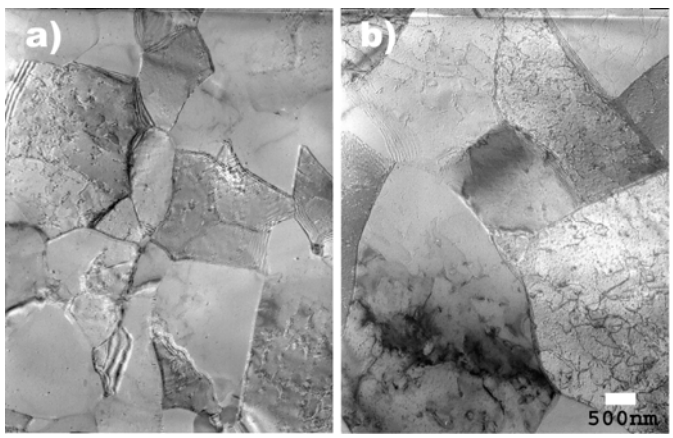

Figure 23.11 show the difference in subgrain size between a) the surface and b) the middle in alloy 4 as extruded, TEM micrographs.

23.3 Coarsening kinetics of dispersoids

The size (mean radius), r, number density, N and volume fraction, f_v, of dispersoids are important factors which determine the recrystallisation resistance of a material. Equation 2.17 (Chapter 2), show that a high f/r-ratio is beneficial in order to provide a high recrystallisation resistance. This also means that to maintain this good recrystallisation resistance it is crucial to avoid or to minimise dispersoid coarsening. Limited data concerning coarsening kinetics are available in the literature for temperatures close to 600^{o}C. As a consequence such studies have been carried out for alloys 4-6. Figures 23.12-23.14 show that limited coarsening takes place at 500^{o}C. However, at 600^{o}C the coarsening is much more pronounced than at lower temperatures. From Table II-IV in Appendix, the dispersoid data for alloys 4-6 at different temperature can be seen. Figures 23.15-23.20 show TEM micrographs of particle coarsening in alloy 4 and 6 annealed at different times and temperatures.

a)

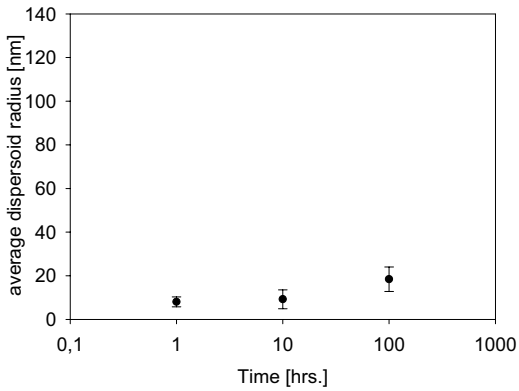

b)

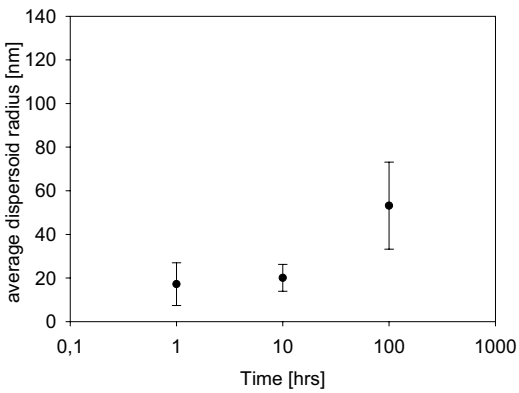

c)

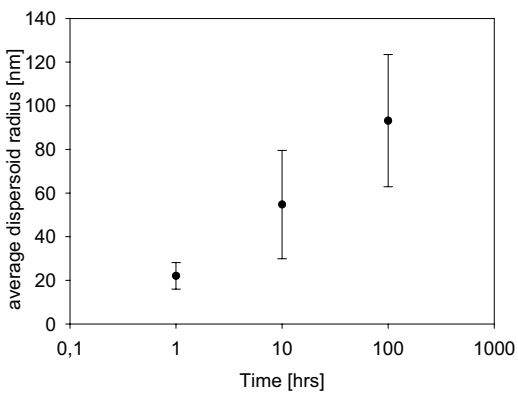

Figure 23.12 Dispersoid coarsening in alloy 4 during annealing at a) 500^{o}C b) 550^{o}C c) 600^{o}C

Part C

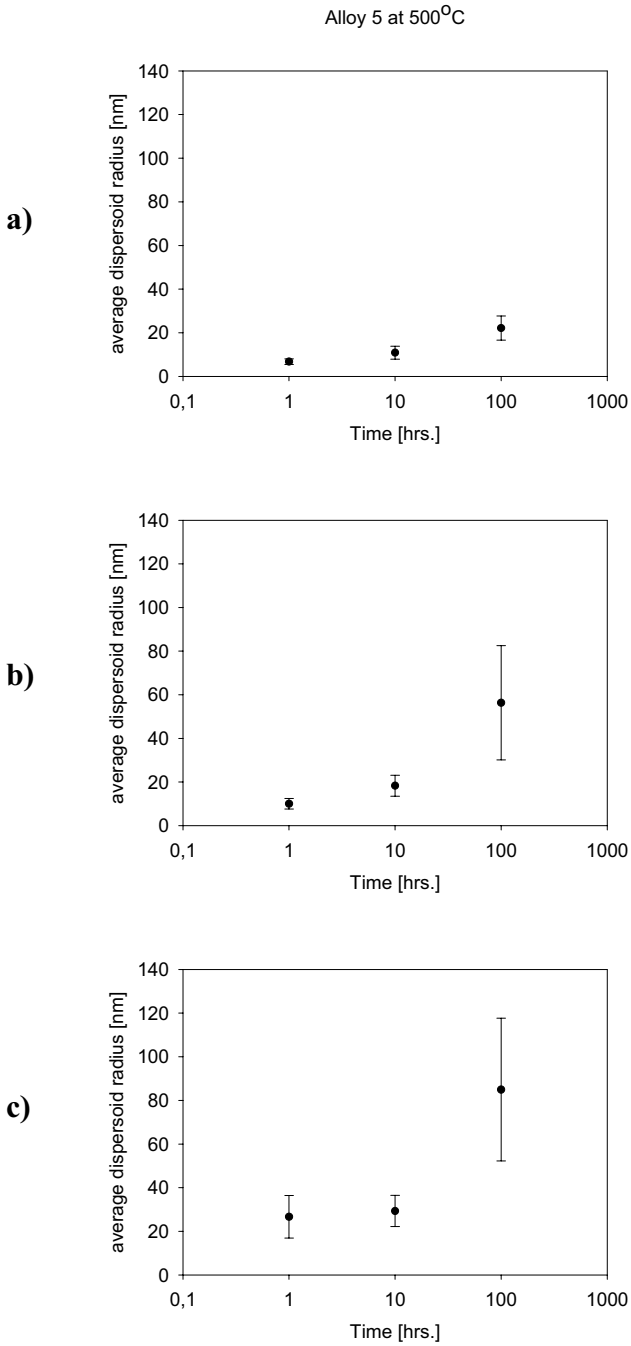

Figure 23.13 Dispersoid coarsening of alloy 5 during annealing at a) 500°C b) 550°C c) 600°C

a)

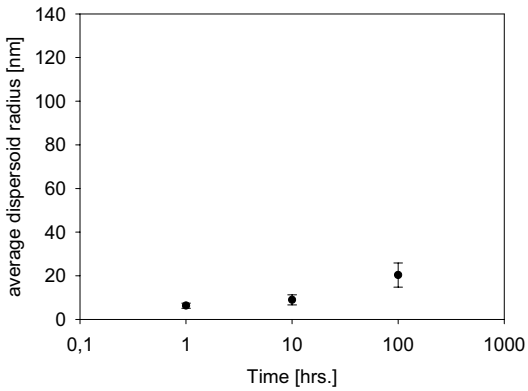

b)

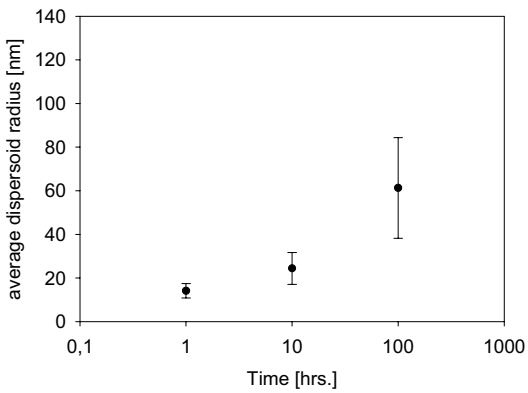

c)

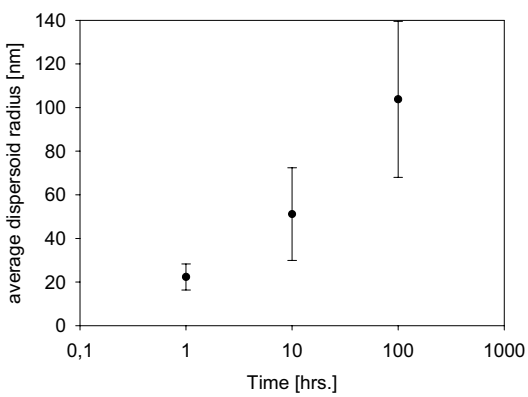

Figure 23.14 Dispersoid coarsening in alloy 6 during annealing at a) 500°C b) 550°C c) 600°C

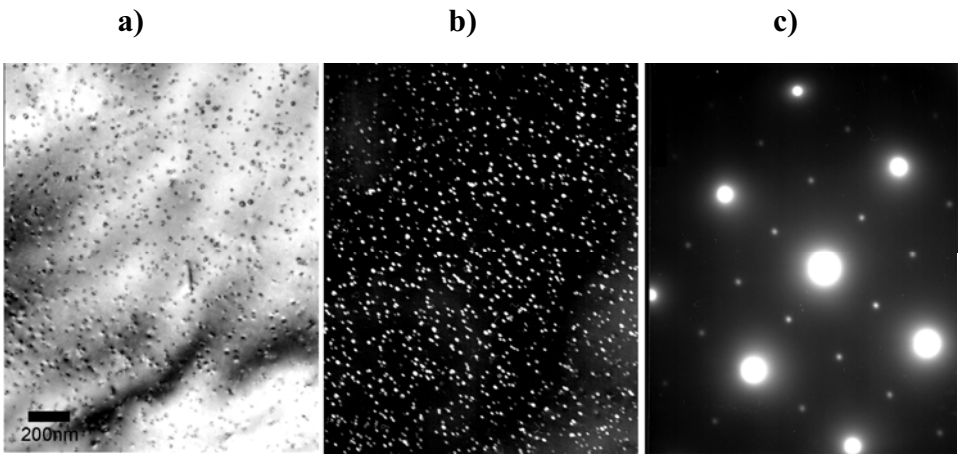

Figure 23.15 TEM images of alloy 6 after 1hr at 500°C. a)BF, b)DF and c)Diffraction pattern from [100]-zone. $Al_3(Sc,Zr)$ dispersoids can be seen.

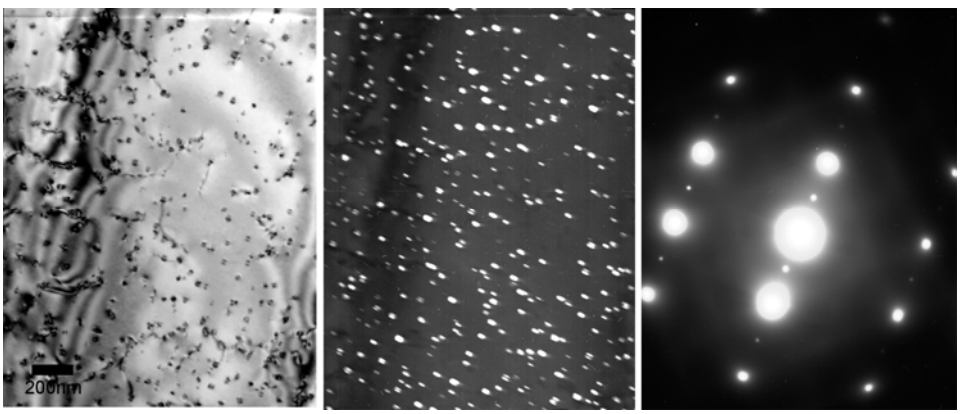

Figure 23.16 TEM images of alloy 6 after 1hr at 550°C. a)BF, b)DF and c)Diffraction pattern from [310]-zone. $Al_3(Sc,Zr)$ dispersoids can be seen.

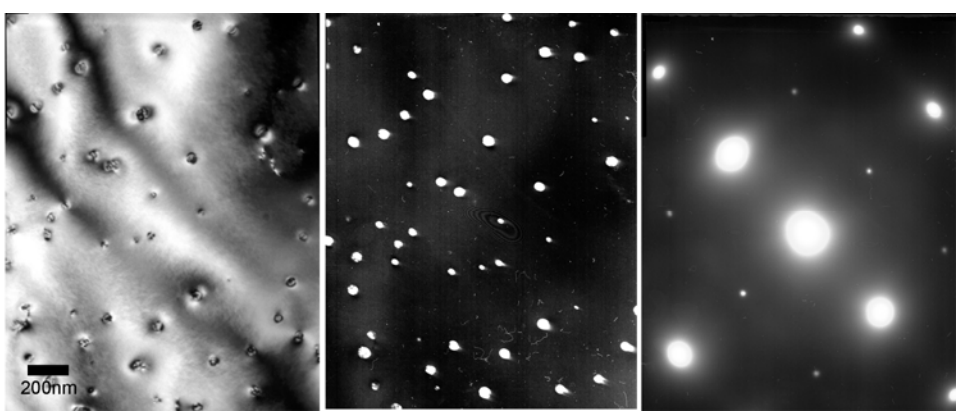

Figure 23.17 TEM images of alloy 6 after 1hr at 600°C. a)BF, b)DF and c)Diffraction patterns from [211]-zone. $Al_3(Sc,Zr)$ dispersoids can be seen.

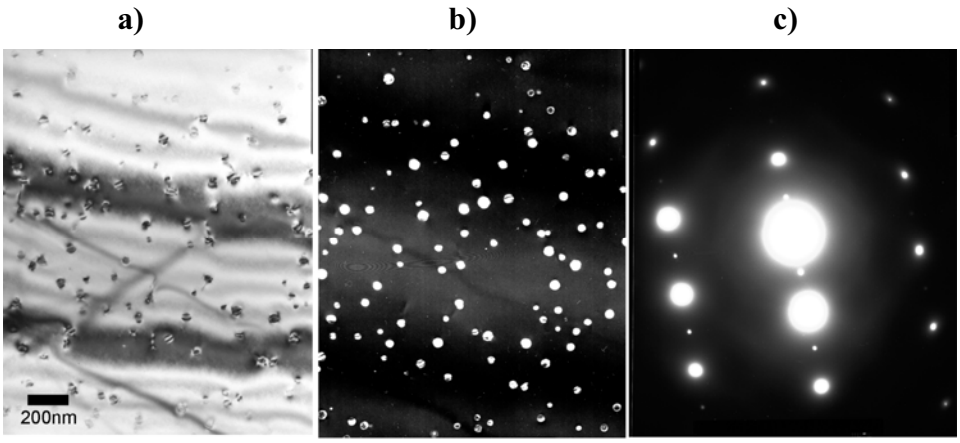

Figure 23.18 TEM images of alloy 4 after 1hr at 600°C. a)BF, b)DF and c)Diffraction patterns from [310]-zone. $Al_3(Hf,Sc,Zr)$ dispersoids can be seen.

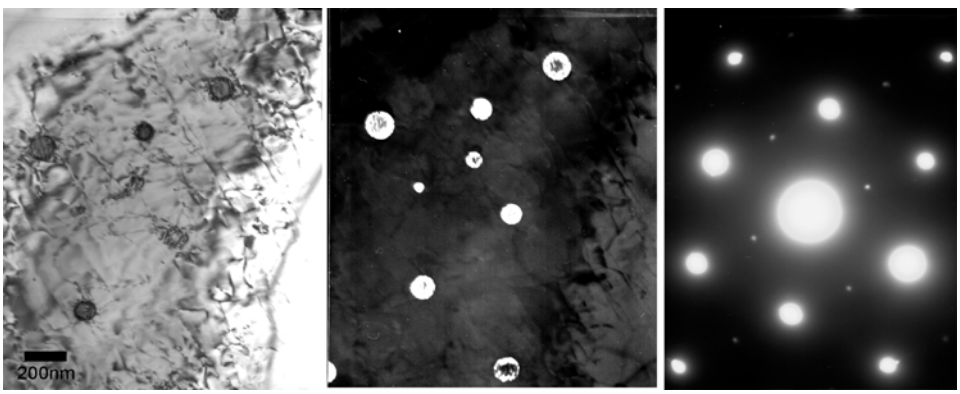

Figure 23.19 TEM images of alloy 4 after10hr at 600°C. a)BF, b)DF and c)Diffraction patterns from [110]-zone. $Al_3(Hf,Sc,Zr)$ dispersoids can be seen.

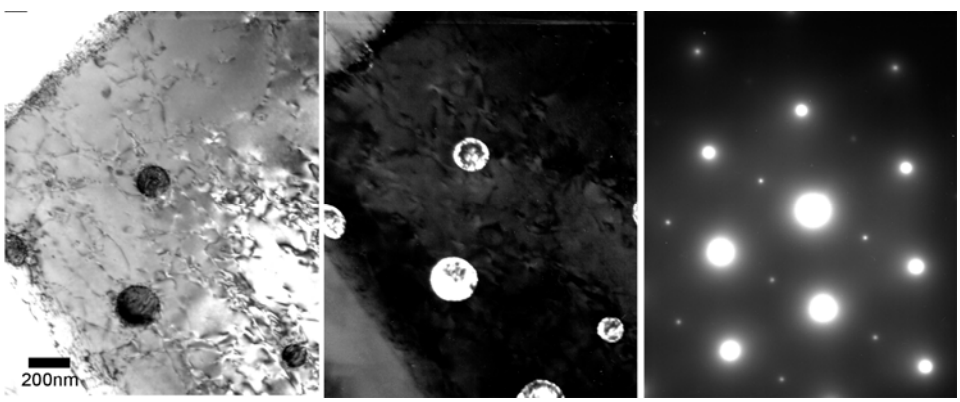

Figure 23.20 TEM images of alloy 4 after100hr at 600°C. a)BF, b)DF and c)Diffraction patterns from [110]-zone. $Al_3(Hf,Sc,Zr)$ dispersoids can be seen.

23.3.1 Variation in dispersoid distribution

Table 23.3 shows that the size of the dispersoids in the middle and surface regions of the extruded profiles were fairly similar. However, as shown in Figure 23.21, the dispersoid distribution was significantly different. While a homogeneous distribution was observed in the middle of the profiles, the dispersoids were more heterogeneously distributed in the surface regions and also the density was found to be lower in the surface region. A similar variation was also observed by Forbord (2005) in an Al-Mn-Sc-Zr alloy.

Table 23.3 Dispersoid data for the surface and the middle regions of the extrude profile.

Alloy 4	**Disp radius Surface (nm)**	**Density (m^{-3}) 10^{21}**	**Volume fraction 10^{-3}**	**Disp radius Middle (nm)**	**Density (m^{-3}) 10^{21}**	**Volume fraction 10^{-3}**
As extruded	8	5,6	9,9	7	13,9	20,8
60 min at 600°C	23	0,2	9,5	22	0,9	38,5
Alloy 6						
As extruded	9	2,9	7,7	7	4,9	5,9
60 min at 600°C	25	0,3	16,7	22	0,19	9,1

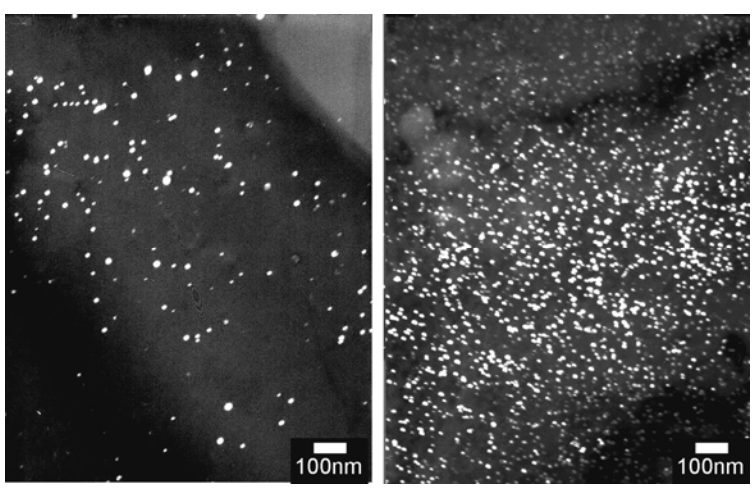

Figure 23.21 Micrographs illustrating the difference in dispersoid distribution between the surface (left image) and the middle of the profile (right image) in alloy 4.

23.3.2 Mechanical properties

Figures 23.22-23.24 show the yield strength (cf. Chapter 4.6) of the extruded profiles as a function of annealing time. At the lowest temperature, 500°C, the loss in strength is small for all the variants. When the temperature is raised to 550°C, the strength drop is larger and alloy 2 stabilises at 50 MPa while alloys 3-6 stabilise at 90-110 MPa. However, at 600°C the strength loss is considerably larger. Alloys 4-6 stabilise at 50-80 MPa and alloys 2-3 at 20-30 MPa.

The strength of alloys 4-6 during annealing at 600°C was also followed by hardness measurements especially to study the hardness after short annealing times in more detail, see Figure 23.25. An abrupt drop in strength was observed already after 30sec annealing time in all alloys, but after 5 minutes the hardness seems to stabilise at a "minimum" value for all variants as also observed in the yield strength tests. However, it is worth to notice that this value is significantly higher in alloy 4 and 6, than in 2, 3 and 5.

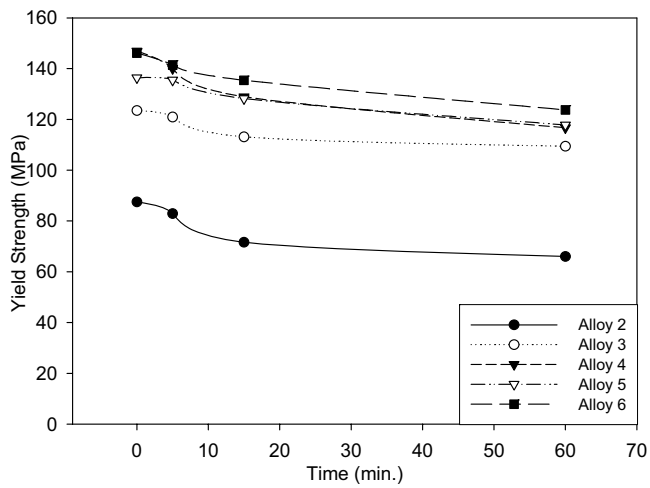

Figure 23.22 Yield strength as a function of time at 500°C for alloy 2-6.

Part C

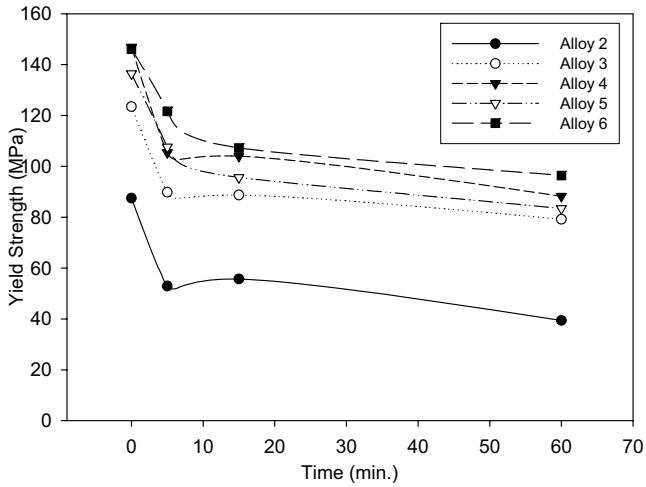

Figure 23.23 Yield strength as a function of time at 550°C for alloy 2-6.

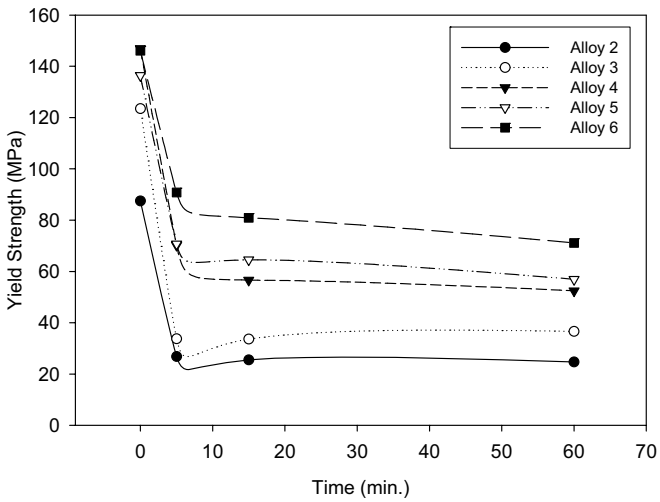

Figure 23.24 Yield strength as a function of time at 600°C for alloy 2-6.

Part C

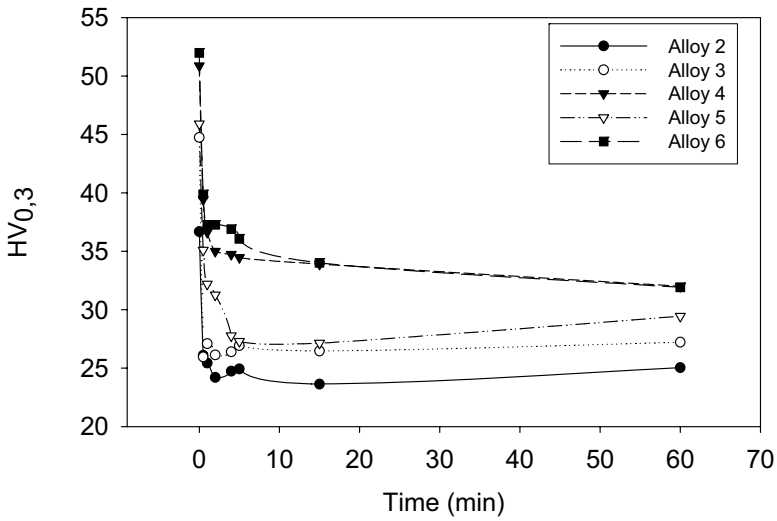

Figure 23.25 Microhardness as a function of time of the alloys after annealing at 600°C.

24 Cold rolling and annealing of the extruded profiles

After extrusion, profiles are frequently subjected to stretching and/or various forming operations (rolling). The stored energy introduced during forming, provide an additional driving force for recrystallisation. As a consequence it is interesting to investigate the recrystallisation resistance of extruded profiles of alloys 2-6 after cold rolling to various degrees of deformation (0-80%). This was done by annealing the cold rolled profiles for 1hr at temperatures between 500°C-600°C in salt bath.

As shown in Figure 24.1, a significant increase in the recrystallisation resistance can be achieved by the addition of Sc to the alloys. Alloy 2 (Al-Hf-Zr) maintains a fibrous structure for all rolling reductions at 450°C. However, at 500°C only the variants cold rolled 0% and 10% stayed unrecrystallised. The Sc-containing alloys were remarkably stable. Alloy 3 (Al-Sc-Hf) and 4 (Al-Hf-Sc-Zr) only show surface recrystallisation both after annealing at 550°C and 600°C for 1 hr following 80% cold rolling. Alloy 5 displays recrystallised grains randomly distributed in the material after annealing at 600°C in the samples deformed 0, 10 and 20%, while it is fully recrystallised after 50% cold rolling. However, alloy 6 (Al-Sc-Zr), which is the alloy with the lowest alloying content totally, shows the best recrystallisation resistance as this alloy remains unrecrystallised up to 80% cold rolling followed by a heat treatment of 1 hr at 600°C.

From Figure 24.2 it can be seen that there is no clear drop in hardness visible upon recrystallisation. All alloys, except for alloy 2 (Al-Hf-Zr) show an increase in hardness at ~300°C, probably caused by precipitation of new dispersoids. With increasing annealing temperature there is a gradually decreasing hardness.

Part C

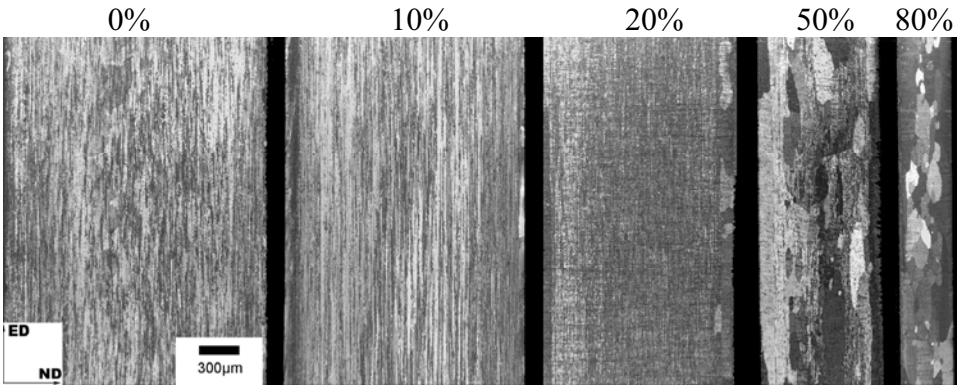

a) Alloy 2, 500ºC, 1 hr

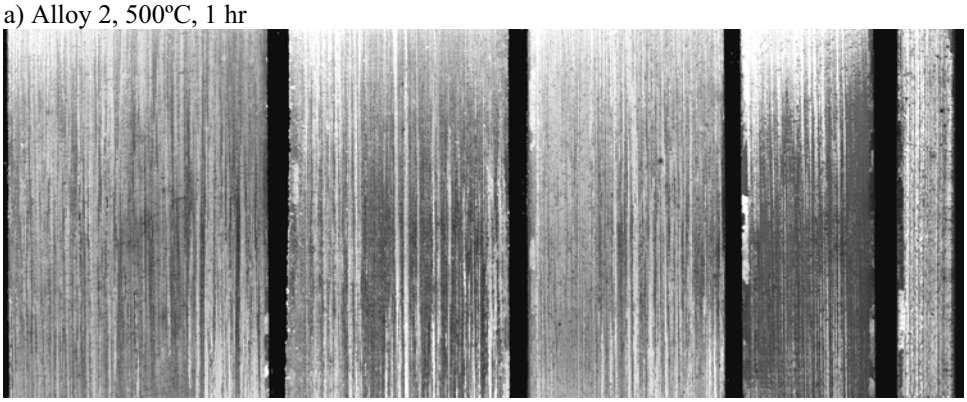
b) Alloy 3, 550ºC, 1 hr

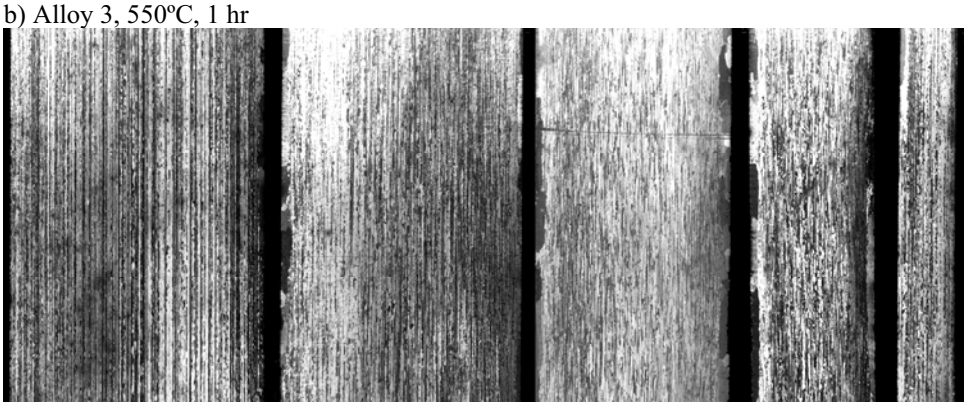
c) Alloy 4, 600ºC, 1 hr

d) Alloy 5, 600ºC, 1 hr

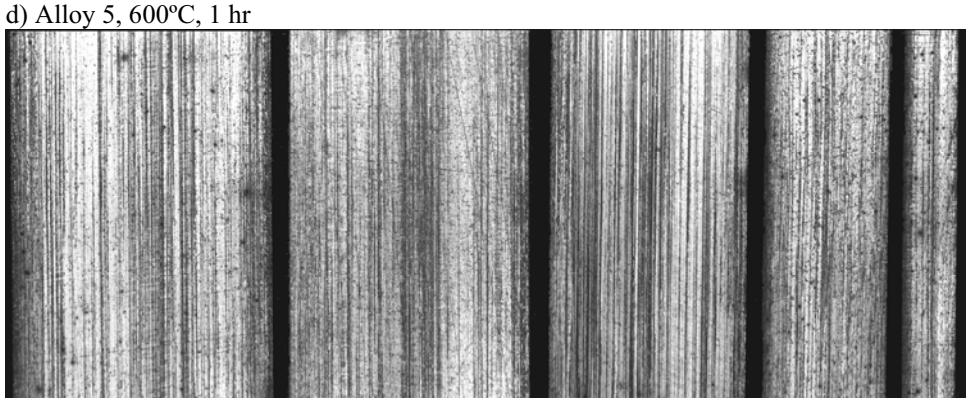

e) Alloy 6, 600ºC, 1 hr

Figure 24.1 (a-e): Examples of microstructures as observed in the optical light microscope after cold rolling and annealing of the extruded profiles. For each alloy the specimens are ordered from left to right with an increasing degree of cold rolling (0-10-20-50-80%).

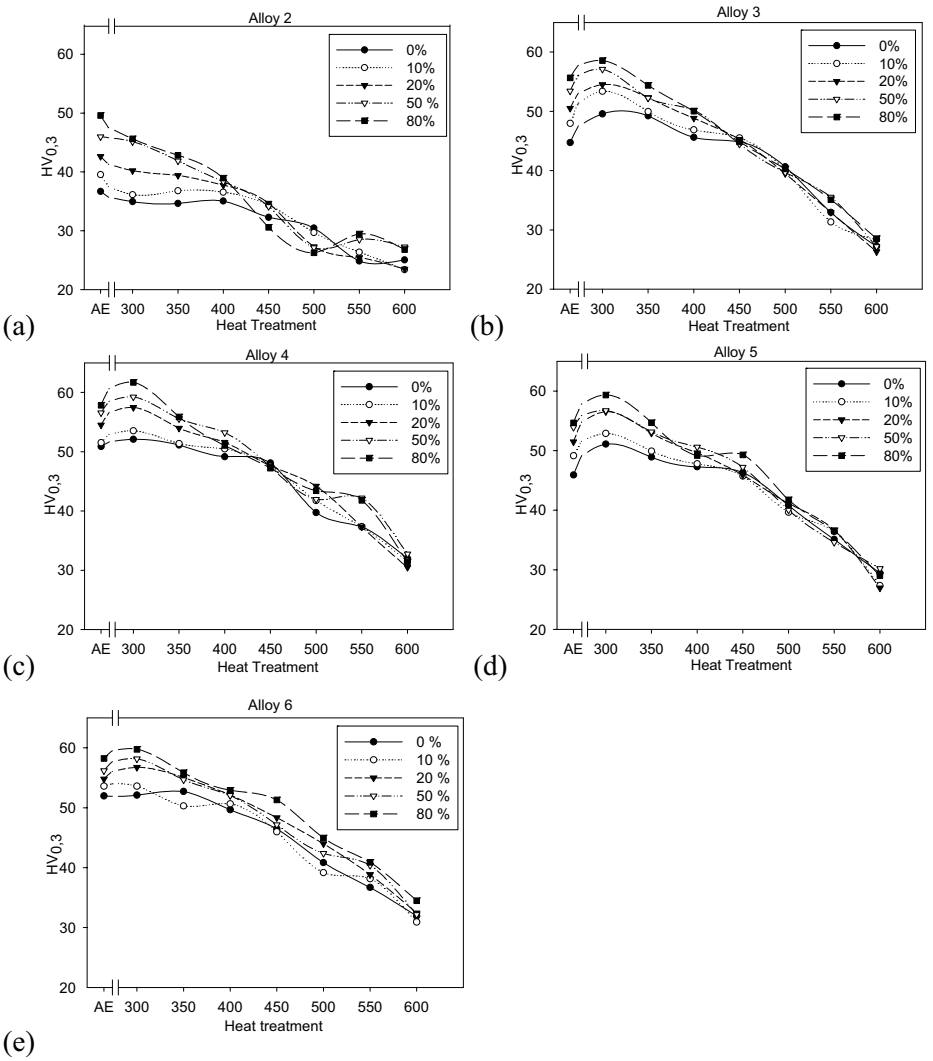

Figure 24.2 (a-e): Hardness measurements as a function of the degree of cold rolling and subsequent annealing temperature in salt bath for the investigated alloys. The legend indicates the nominal degree of cold rolling for the specimens.

25 Discussion

25.1 Precipitation of dispersoids during homogenisation

The main objective of the homogenisation process was to induce precipitatation of dispersoids. The homogenisation annealing is also well described and thoroughly investigated in part B.

25.1.1 Influence of micro-segregation on precipitation

The line scan investigations revealed large differences in Hf, Sc and Zr concentrations across the grains in both the as cast and homogenised samples, see Figures 22.1-22.6. As Al-Sc is a eutectic alloy system, the highest concentration of Sc are found close to the grain boundaries [Riddle et al. (2002), Røyset and Ryum (2005)]. Hf and Zr, on the other hand, segregates to grain centres as Al-Hf and Al-Zr are peritectic systems [Forbord et al. (2004), Murray et al. (1998), Robson and Prangnell (2001)]. From Figure 25.1 it is shown that when the temperature reaches 475^{o}C after a heating rate of 50^{o}C/hr, Zr has diffused on average about 35 nm and Hf 15 nm. Sc, however, has diffused almost 900 nm when the alloy reached 475^{o}C according to Eq 17.5, see Figure 25.2. As Hf and Zr diffuses slowly in Al, the concentration gradients were not removed during homogenisation. Due to this, precipitation took place in segregated structures, and the driving force for precipitation consequently varied in the Sc-free material. This explains why the dispersoid distributions were heterogeneous in the Sc-free variants and homogeneous in the Sc containing alloys [Hallem et al. (2004a)].

Even though Sc diffuses considerably faster than Hf and Zr [Fujikawa (1996) and (1997),], the homogenisation did not lead to a completely smooth concentration profile. This is in contrast with findings of Riddle et al. (2002) who found that it was possible to level out the concentration gradients in the grains during homogenisation of an Al-Mn-Mg-Sc-Zr alloy (50^{o}C/hr to 475^{o}C and held for 5hrs). However, due to the extremely low solubility of Sc in Al (large driving force), precipitation of Sc-

containing dispersoids still takes place everywhere in the structure and ensures a homogeneous dispersoid distribution. At the grain boundaries, where the Sc-content is high and the Hf- and Zr- contents are relatively low, Sc increases the driving force for precipitation leading to no particle free zones as observed in Al-Zr alloys [Robson and Prangnell (2001)]. Due to this fact and the fast Sc diffusion, all dispersoids, even in the grain centre, were found to be rich on Sc. This is also consistent with what different models predict for these alloys [Lae et al. (2004), Robson et al. (2003), (2004)]

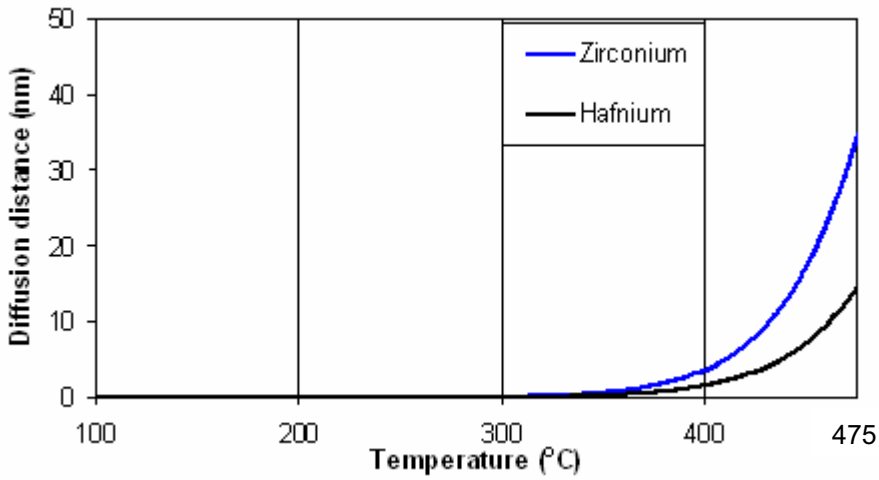

Figure 25.1 Average diffusion distance of Hf and Zr during homogenisation (50°C/hr).

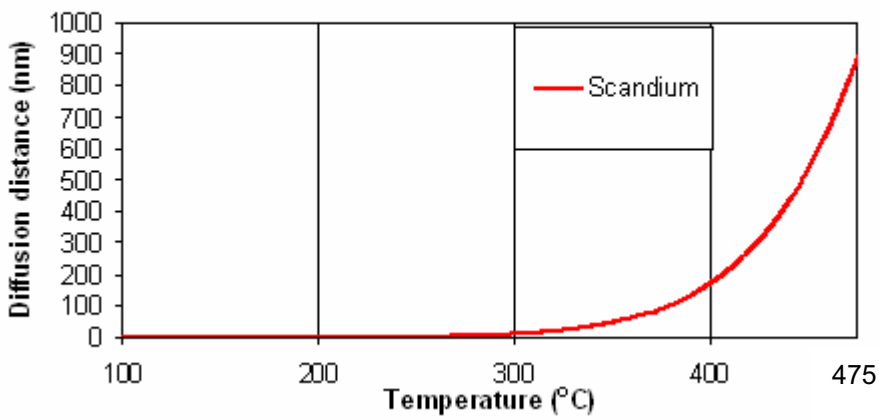

Figure 25.2 Average diffusion distance of Sc during homogenisation (50°C/hr).

25.2 Extrusion of the alloys

25.2.1 Effect of dispersoids on recrystallisation resistance during extrusion.

Only the Al-Hf alloy (alloy 1) recrystallised during extrusion, the poor recrystallisation resistance can be related to the low number density and heterogeneous distribution of dispersoids which is observed in the alloy. However, in alloy 2 where Zr and Hf are added in combination no recrystallisation was observed despite the fact that the dispersoids were few and heterogeneously distributed. This may indicate that addition of Zr reduces the solubility of Hf, leading to increased driving force for precipitation. Zr has also a higher diffusion rate than Hf, which may ensure faster precipitation of dispersoids in the alloy.

In the Sc-containing alloys 3-6, all variants displayed a high density of homogeneously distributed dispersoids which provide a high Zener-drag and consequently stabilise the structure. The Sc containing alloys also display a smaller dispersoid size, leading to better recrystallisation resistance. From the calculations, alloy 4 displayed the largest f/r ratio, more than three times larger than alloy 6 after extrusion. Alloy 3 has also a larger f/r ratio, which may indicate that Hf decreases the solubility of Sc enhancing the precipitation. The results can be seen in Table 25.1 and Figures 22.8-22.9.

Table 25.1 f/r calculations for the different alloys.

Alloy	Average radius	Average volume fraction	f/r [10^{-3}]
1.Al-Hf-Si-Fe	Too few to measure	-	
2.Al-Hf-Zr-Si-Fe	14nm	-	
3.Al-Hf-Sc-Si-Fe	9nm	1,2E-02	1,3
4.Al-Hf-Sc-Zr-Si-Fe	7nm	2,1E-02	3,0
5.Al-Hf-Sc-Zr-Si-Fe	6nm	7,5E-03	1,3
6.Al-Sc-Zr-Si-Fe	7nm	5,9E-03	0,8

In Figure 22.10 an overview of the particle size and distribution of dispersoids are plotted. In alloys 4, 5 and 6 which are the alloys with the best performance in terms of the recrystallisation resistance, a narrow particle size distribution was observed. However, alloy 5 has a broader distribution than alloys 4 and 6, but displays still a better/narrower distribution than alloys 2 and 3. This may indicate that the Al_3(Hf,Sc,Zr) and Al_3(Sc,Zr) dispersoids nucleate almost simultaneously (site saturation) [Hallem (2004b)].

25.3 Recrystallisation resistance of the extruded profiles during high temperature annealing

Aluminium alloys are currently seldom used for high temperature applications, as their strength drops considerably above 400˚C. However, a higher thermal stability can possibly be achieved by forming a dense distribution of thermally stable dispersoids, which exerts a drag force on moving subgrain boundaries and inhibits recrystallisation and subsequent strength loss. Both Hf, Zr and Sc form such dispersoids, and the objective of this investigation was to study the structural stability of the alloys that did not recrystallise during extrusion (alloys 2-6) at elevated temperatures (500-600^{o}C).

25.3.1 Effect of dispersoid coarsening on recrystallisation resistance

Eq. 2.6 and 2.11 in Chapter 2 shows that dispersoids increase the resistance towards recrystallisation by increasing the critical radius for nucleation, R_c, and the softening rate during high temperature exposure is consequently also reduced. In alloys where the volume fraction, f, becomes high enough, a situation may arise where the substructure is completely stabilised by the dispersoids. In such cases subgrain growth and alloy softening is controlled by the coarsening of dispersoids.

In accordance with fact that the dispersoid distribution varied considerably (Figures 22.9 and 23.15-23.20), the investigated alloys responded differently to the heat exposure (Figures 23.1-23.3). 1hr annealing at 600^{o}C, resulted in complete recrystallisation of alloys 2-3, while alloys 4-6 displayed fibrous structures without any signs of

recrystallisation, see Figure 23.3. The relatively low recrystallisation resistance of alloys 2-3 is due to the inhomogeneous dispersoid distribution in these alloys [Robson and Prangnell (2001), Forbord et al. (2004), Hallem et al. (2004b),]. In regions with a low density of dispersoids (low f/r-ratio), the Zener-drag and consequently also the recrystallisation resistance is low. This can also be seen when alloy 2 recrystallises after 1 hr at 550^{o}C, see Figure 23.2. However, in alloys 4-6, which displayed dense and homogeneous dispersoid distributions, the resistance towards recrystallisation was high everywhere in the material.

It should be noted, though, that the coarsening rates of alloys 4-6 varied. After 100 hrs the average dispersoid size, r, was measured to be 104nm in alloy 6, while in alloy 4 and 5, *r* was 93 nm and 85 nm, respectively, i.e. it seems as though the dispersoid size, *r*, decreases with increasing alloying content. These results indicate that Al_3(Hf,Sc,Zr) dispersoids are even more stable than Al_3(Sc,Zr) dispersoids. Literature-data show that Al_3(Sc,Zr) has a higher lattice mismatch with the matrix than Al_3(Hf,Sc) [Harada (2002)]. The interfacial energy between Al_3(Sc,Zr) and matrix is consequently higher than for Al_3(Hf,Sc)/matrix, and the coarsening rate of the former types of dispersoid will consequently be higher. No data is found for Al_3(Hf,Sc,Zr), but it is natural to assume that the coarsening rates of these dispersoids would be somewhere between those of Al_3(Sc,Zr) and Al_3(Sc,Hf). These results indicate that Hf has a beneficial effect in these alloys when alloyed with Sc and Zr. However, it is important to notice that the standard deviation of the dispersoid measurements are large at these temperatures and long annealing times (due to relatively few measurements).

Despite the fact that alloy 4 displays a slower coarsening rate (and higher f/r-ratio) than alloy 6, the former begins to recrystallise first. However, this is due to the coarse primary particles which form during solidification of alloy 4. During extrusion, deformation zones will form around these phases and later act as nucleation sites for recrystallisation during post-extrusion annealing [Humpherys and Hartherly (1995)]. Such coarse phases were not present in alloy 6, and this explains why alloy 6 displays the highest resistance towards recrystallisation after 1 and 10 hrs annealing. However, alloy 4 can display a partly fibrous structure even after 100hrs at 600^{o}C while alloy 6 is totally recrystallised at this stage (Table 23.1 and Figures 23.1-23.3). The amount of primary phases can probably be reduced by increasing the cooling rate during casting or decreasing the amount of Hf in the alloys.

The data was finally plotted as ln(r) vs. ln(t) in order to investigate whether the dispersoid coarsening was controlled by interface or volume diffusion. By studying the logarithmic form of the coarsening expression (Eq. 2.25-2.26), it becomes obvious that volume diffusion dominates if a slope of 1/3 is obtained when plotting ln(r) as a function of ln(t). A slope of (1/4), on the other hand, indicates interface diffusion. The calculations show that interface diffusion dominates at 500°C as a slope close to 1/4 was obtained. However, at 600°C a slope of 1/3 was found revealing that diffusion through the volume controlled the coarsening. The theoretical background for this is further explained in Chapter 2.

Table 25.2 Calculated diffusion values.

Temperature	Alloy 4	Alloy 5	Alloy 6
500°C	0,18	0,26	0,26
550°C	0,25	0,38	0,3
600°C	0,31	0,30	0,33

Loss of coherency: When a dispersoid grows, it will sooner or later reach a critical size, where it will be more energetically favourable to introduce dislocations at the dispersoid/matrix interface and thereby loss of coherency, rather than increasing the matrix strain. For Al_3Sc this critical radius was found to be ~20 nm in Al-Sc [Drits et al. (1984), Marquis and Seidman (2001)] and 25 nm in Al-0,2wt%Sc [Riddle (2000)]. The addition of Zr may have a positive effect, as Riddle also concluded from the fact that $Al_3(Sc,Zr)$-dispersoids with a radius of 28 nm was fully coherent with the matrix in an Al-0,2wt%Sc-0,12wt%Zr-alloy. In the TEM-investigations carried out here (Figure 23.15-23.20), no evidence of coherency-loss was detected at radii between ~20-30 nm for alloys 4-6. However, as their sizes exceed r~50 nm the Moire-contrast and dislocations clearly reveal coherency loss.

An interesting possibility of increasing the thermal stability, i.e. reducing coarsening rate, is Mg-additions. For instance, Drits (1983) found that Al_3Sc remained coherent up to 58nm radius in Al-(4,4-8,3)Mg-(0,25-0,3)Sc alloys. Drits (1982) also calculated the mismatch between Al and Al_3Sc as a function of Mg-content. These calculations revealed that the difference between Al and Al_3Sc lattice parameters decreases with increasing Mg content, hence postponing coherency-loss to larger

dispersoid sizes. Due to the microstructural similarities between Al_3Sc, $Al_3(Sc,Zr)$ and $Al_3(Hf,Sc,Zr)$, it is likely that Mg-additions may improve the thermal stability of the two latter dispersoids types as well. This is important as coherent disperoids not only coarsen more slowly than semi-/incoherent ones, but also exert a relatively higher Zener drag on moving subgrain boundaries.

25.4 Relationship between substructure and mechanical properties

The strength of a material can be related to microstructural parameters such as the particle size, r, dislocation density, ρ, subgrain size, δ, grain size, D and fraction recrystallised, X(t) . A widely used expression for this relationship is [Vatne et al. (1996, 1998), Sæter (1998)], see also Chapter 2.5.4:

$$\sigma_{0,2} = \sigma_i + \sigma_p + \left(\alpha_1 MGb\sqrt{\rho_i} + \alpha_2 MGb\left(\frac{1}{\delta} + \frac{1}{D}\right)\right)\left(1 - X(t)\right) \qquad (25.1)$$

In the following this relationship will be used to explain the softening of the alloys at temperatures between 500 and 600°C (Figure 23.22-23.25).

25.4.1 Effect of dispersoids coarsening and subgrain growth on softening

Annealing at high temperatures leads to subgrain growth. As shown in Equation (25.1) an increase in subgrain size, δ, leads to a strength reduction. Normally, subgrain growth would eventually lead to recrystallisation, but in alloys 4 and 6, where the dispersoid density is extremely high, no signs of recrystallisation were observed. In other words, these two variants probably soften by extended recovery/continuous recrystallisation controlled by the coarsening of these dispersoids. By comparing softening, subgrain growth and dispersoid coarsening kinetic, there seems to be a strong correlation between these data (Figures 25.3-25.4). Both σ_p, $1/\delta$ and $1/r$ display a

similar dependence on the annealing time, *t*. This behaviour is in agreement with Eq. 25.1.

The assumption of diffusion controlled softening is further supported by the r vs. δ-plot and *1/δ* vs. *σ* in Figures 25.5-25.6, where a linear relationship was obtained between these parameters in alloy 6. For alloy 4, however, the results are not that conclusive as seen from Figure 25.6, but this may be due to poor statistics and large uncertainties in the measurements. Finally, it should be mentioned that Ferry et al. (2005) performed a similar investigation of an Al-0,2wt%Sc-alloy, where it was also concluded that dispersoid coarsening controlled the subgrain growth and alloy softening.

Alloys 4 and 6 were also compared after annealing for 60 min at both 500°C and 600°C. These results showed that the coarsening of the grains/subgrains are much smaller at 500°C than at 600°C due to less coarsening of the dipersoids. This can also be seen in the strength evolution (Figures 23.22-23.25)

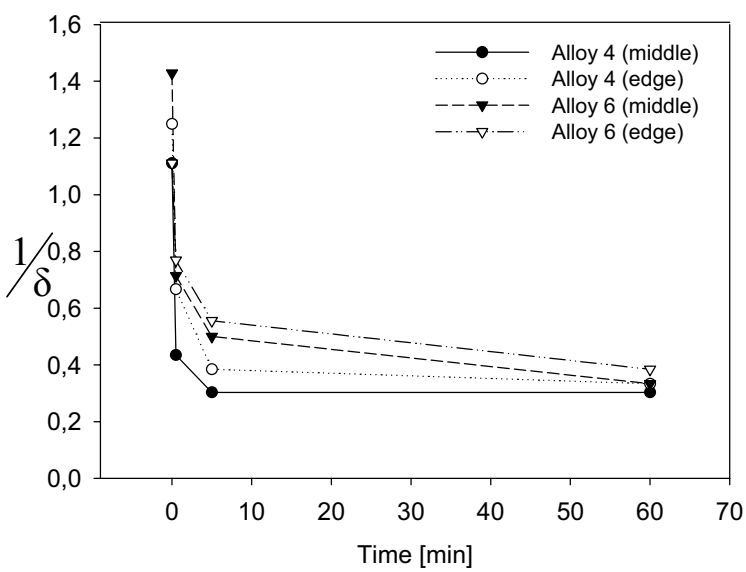

Figure 25.3 Variation of average subgrain size at 600°C.

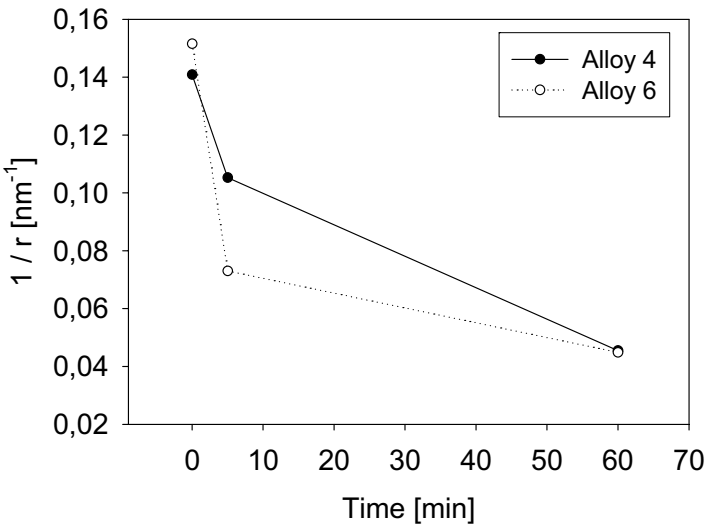

Figure 25.4 Variation of inverse dispersoid radius with time at 600°C.

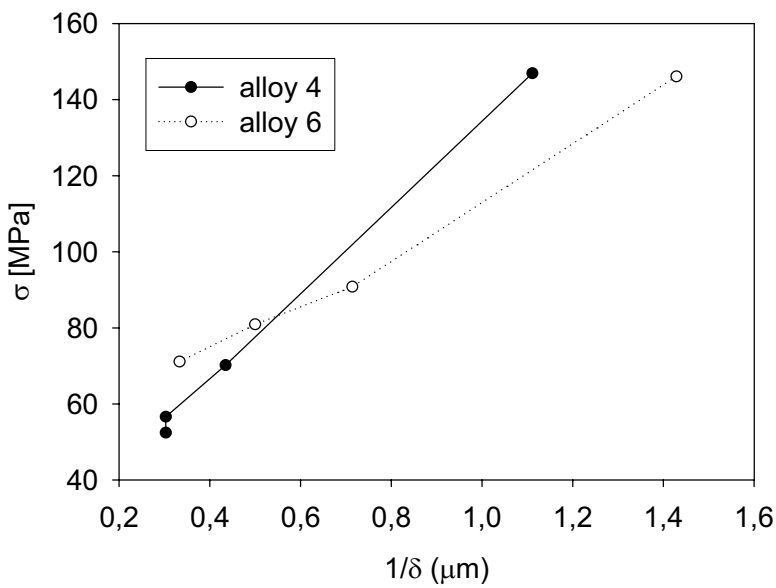

Figure 25.5 Comparison of yield strength and inverse subgrain growth at 600°C

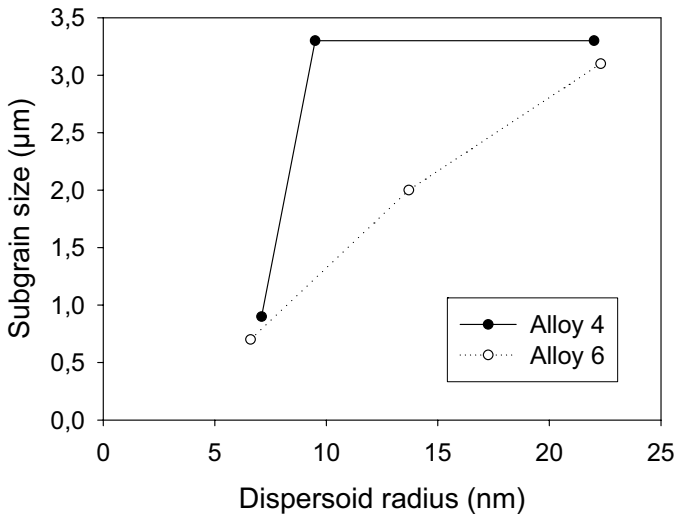

Figure 25.6 Comparison of subgrain growth and dispersoid coarsening at 600°C.

25.4.2 Formation of recrystallised surface layer

Alloys 4-6 displayed a remarkable recrystallisation resistance during high temperature annealing (HTA) at 600°C. However, a thin recrystallised layer appeared in the surface after 1 hr and 10hrs for alloys 6 and 4, respectively. The formation of these layers can probably be related to the more severe deformation of the surface layer during extrusion. A consequence of this is a higher stored energy, P_D, i.e. finer subgrain size (Figure 23.11), and possibly also a coarser dispersoid distribution (Figure 23.21 and Table 23.3) in the surface regions, which in turn would lead to a lower Zener-drag, P_Z, compared to the centre of the profile (Eq.2.6).

These differences are not easily detected in EBSD due to the relatively poor spatial resolution in SEM. As a consequence TEM-investigations of both the subgrain structure and the distribution of dispersoids were performed on samples from the middle and from the surface of the profiles. The investigations revealed that the subgrain size, δ, was almost twice as large in the centre as in the surface regions. These variations are also observed by Tangen et al. (2003), in an Al-Mn-Mg-Sc-Zr alloy.

Slightly larger dispersoids were also observed close to the surface. A somewhat surprising observation, however, was that the investigations revealed that the dispersoid distribution in the surface regions was in fact heterogeneous. Semi-coherent dispersoids was also observed, while those in the centre were exclusively coherent. The variation in both subgrains and dispersoids can explain the recrystallised surface layer which appears during HTA in some alloys. These variations have been summarised in Figure 23.21 and Table 23.3.

25.5 Cold rolling and annealing

Extruded profiles are often subjected to further forming operations. In order to study the structural stability of alloy, 2-6, after various degrees of deformation, the extruded profiles were therefore as described in Chapter 4.4 cold rolled and subsequently annealed. Cold deformation is a far more severe deformation process than hot deformation at comparable deformation reductions, involving a higher stored energy and thus driving force for recrystallisation upon subsequent annealing. From this fact it is consequently possible that a finer and more stable dispersoid distribution, i.e. a higher Zener-drag, is necessary to stabilise the structure. This aspect will be discussed in the following.

25.5.1 Recrystallisation resistance in cold rolled material.

Alloy 6, which contains Al-Sc-Zr, displayed an unrecrystallised structure after annealing for 1 hr at 600^{o}C after 80% cold rolling. To the author's knowledge it is most unusual as compared to alloys with any other dispersoid forming elements to perform so well. Even though alloy 4 and 5 displayed a larger f/r ratio than alloy 6 after extrusion (larger Zener-drag), these alloys did not display a similar good recrystallisation resistance as alloy 6 after cold deformation. As discussed earlier, deformation zones around the primary particles in these alloys (alloy 4 and 5) do form after cold rolling and induce PSN.

From Figure 24.2 it can be seen that there is no clear drop in hardness in any of the alloys upon recrystallisation. All alloys, except for alloy 2 (Al-

Hf-Zr) actually shows an increase in hardness around 300°C. This is probably caused by precipitation of new Sc-containing dispersoids upon heat treatment at these temperatures (~300°C). With increasing annealing temperature there is a gradually decreasing hardness. Up till an annealing temperature of 450°C the decrease in hardness for the samples with a high degree of cold deformation is steeper than for the sample with a low degree of cold work. Above 450°C hardly any visible effect of the cold rolling is seen as a result of the preceding heat treatment as long as the microstructure remains non-recrystallised. However, the coarsening and dissolution of the dispersoids, which lower the Zener-drag, leads to a faster recovery process and consequently a lower hardness. As discussed earlier, the substructure is stabilised by the dispersoids and the coarsening of the dispersoids will control the softening reactions. The diffusion and thereby the coarsening in these alloys will go faster, since more high speed diffusion-paths are available (dislocations, subgrain boundaries) after cold rolling.

A similar experiment with Al-Mn-Mg-Sc-Zr alloys has been performed by Røyset and Riddle (2004). In Røyset's experiment it was found that an alloy containing 0,26wt% Sc and 0,15wt% Zr resisted recrystallised after 80% reduction and annealing 1hr at 600°C. In our experiments only 0,18wt% Sc and 0,22wt% Zr were present in the alloy that performed best (Al-Sc-Zr), an aspect which from a cost/benefit point of view is an interesting result since Sc is very expensive.

26 Conclusions

The following conclusions may be drawn from the investigations carried out in Part C.

- A heterogeneous distribution of dispersoids was observed in the Sc-free alloys, Al-Hf (1) and Al-Hf-Zr (2), while the Sc-containing, Al-Hf-Sc (3), Al-Hf-Sc-Zr (4-5) and Al-Sc-Zr (6), alloys displayed a homogeneous distribution of dispersoids.

- All alloys except the Al-Hf (1) alloy resisted recrystallisation during the extrusion process.

- During high temperature annealing of the extruded profiles, alloys 4-6 displayed fibrous structures without any signs of recrystallisation after 1hr at 600^{o}C. Alloy 4 (Al-Hf-Sc-Zr) displayed a mainly fibrous structure even after 100hrs at 600^{o}C. Both alloy 4 and 6 (Al-Sc-Zr) were also unrecrystallised after annealing 100hrs at 500 and 550^{o}C.

- The substructure coarsening and consequently also the strength, is controlled by the coarsening of the dispersoids.

- A heterogeneous distribution of dispersoids was observed close to the surface of the extruded profiles. Furthermore, smaller subgrains were observed in the surface compared to the middle of the profiles, i.e. the driving force for recrystallisation is highest in the surface.

- Alloys 4 and 6 displayed a remarkable recrystallisation resistance after extrusion and cold rolling. Alloy 6 totally resisted recrystallisation even after 80% cold deformation and 1hr annealing at 600^{o}C. Alloy 4 displayed an almost equally remarkable resistance, only displaying a thin recrystallised region in the surface of the profile.

27 References

Drits, M.E., Torpova, L.S., Bykov, Yu.G., Ber, L.B., Pavlenko, S.G., Russian Meatllurgy, v1, pp.148-152, 1982

Drits, M.E., Metal Sci. And Heat Treating, v25, pp.550-554, 1983

Drits, M.E., Ber, L.B., Bykov, Yu.G., Torpova, L.S., Anastas'eva, G.K., Phys.Met.Meatll, v57, n6, pp.118-126, 1984

Ferry, M., Hamilton, N.E., Humpherys, F.J., Acta Materialia, 53, pp.1097-1109, 2005

Forbord, B., Hallem, H., Marthinsen, K., ICAA-9, Brisbane, Australia, pp.1179-1185, 2004

Forbord, B., Private communication, 2005

Fujikawa, S.I., Journal of the Japan Institute of Light Metals, 46(4) pp. 202-215, 1996

Fujikawa, S.I., Defect and Diffusion Forum, pp.143-147, 1997

Hallem, H., Forbord, B., Marthinsen, K., ICAA-9, Brisbane, Australia, pp.240-245, 2004a

Hallem, H., Forbord, B., Marthinsen, K., ICAA-9, Brisbane, Australia, pp.825-831, 2004b

Harada, Y., and Dunand, D.C., Materials Sci and Eng, A329-331, pp.686-695, 2002

Humpherys, F.J., and Hartherly, M., *Recrystallisation and related annealing phenomena, Pergamon Press*, Oxford, 1995

Lae, L., Guyot, P., Sigli, C., ICAA-9, Brisbane, Australia, pp.281-286, 2004

Marquis, E.A., and Seidman, D.N., Acta Mater, 49, p.1909, 2001

Part C

Murray, J.L., McAlister, A.J., Kahan, D.J., Journal of Phase Equilibria Vol. 19, No 4, pp.376-379, 1998

Riddle, Y.W., PhD-thesis, Georgia Institute of Technology, 2000

Riddle, Y.W., Hallem, H., Ryum, N., Mats.Sci.Forum, Vols. 396-402, pp.563-568, 2002

Robson, J.D., and Prangnell, P.B., Acta Mater, 49, pp.599-613, 2001

Robson, J.D., Jones, M.J., Prangnell, P.B., Acta Mater,51, pp.1453-1468, 2003,

Robson, J.D., Acta Materialia, 52, pp.1409-1421, 2004

Røyset, J. and Riddle, Y.W., ICAA-9, Brisbane, Australia, p.1210-1215, 2004

Røyset, J. and Ryum, N., International Materials Reviewes, vol 50, Nr2, pp.1-26, 2005

Sæter, J.A., Forbord, B., Vatne, H.E., Nes, E., ICAA6, p.113, 1998

Tangen, S., Hallem, H., Bjerkaas, H., Hjelen, J. Nes, E., Conference proceedings Scandem , Oslo, 2003

Vatne, H.E., Furu, T., Ørsund, R., Nes, E., Acta Mater., vol44, p.4463, 1996

Vatne, H.E., Furu, T., Nes, E., ICAA6., vol44, p.1257, 1998

Summary

The overall objective of this work has been to develop aluminium alloys, which after hot and cold deformation are able to withstand high temperatures without recrystallising. This has been done by investigating aluminium alloys with various additions of hafnium, scandium and zirconium, with a main focus on Hf and to which extent it may partly substitute or replace Zr and/or Sc as a dispersoid forming elements in these alloys.

What is the effect of hafnium, alone and in combination with Zr and/or Sc and how do hafnium containing alloys perform?

It is shown that hafnium may alter or modify the casting structure, though, not to the better as it can form TCGs in combinations with Zr and/or Sc. This is not advantageous neither as far as it concerns grain refining nor precipitation of dispersoids.

When precipitation of binary Al-Hf is compared to Al-(Hf)-(Zr) alloys, hafnium shows even slower precipitation than in Al-(Hf)-(Zr) alloys and also much slower and with a poorer spatial distribution of dispersoids than in Al-Sc or Al-Hf-Sc alloys. As a consequence, it may be concluded that binary aluminium-hafnium alloys are of limited interest as they display a poor recrystallisation resistance when no other alloying elements are added.

However, when hafnium is added together with scandium and/or zirconium, precipitation may actually improve both in Al-Hf-Zr alloys and in scandium containing alloys like Al-Hf-Sc and Al-Hf-Sc-Zr. Hafnium can still not completely replace neither Zr nor Sc due to its poor precipitation properties. However, Al-Hf-Sc-Zr alloys show a better dispersoid distribution (number density and volume fraction) than what was observed in Al-Sc-Zr alloys after extrusion. The Al-Hf-Sc-Zr alloys also show extreme high temperature properties, by withstanding recrystallisation at high temperatures and long annealing times. After severe cold deformation, the extruded profiles of both the Al-Sc-Zr alloy and the Al-Hf-Sc-Zr alloy displayed a remarkable recrystallisation resistance.

The reason why the Al-Zr-Sc- and the Al-Hf-Zr-Sc alloys behave so well has been investigated by detailed 3D Atom Probe investigations. Due to the homogeneous precipitation of Al_3Sc dispersoids and the retarding effect from Hf and/or Zr containing shells, thus limiting the coarsening of these dispersoids, these combinations have been shown successful.

As we have seen when Hf and Zr are added in combination equal or improved recrystallisation properties can be obtained. This is specially the case when both these elements are added together with scandium. Since Hf and Zr are extremely difficult (and thus costly) to separate, Al-Zr master alloys used in industry today can in the future probably contain more Hf, lowering the cost of master alloys.

The work presented in this thesis have hopefully added some new insight and a better understanding of the effects of adding various dispersoid forming elements to aluminium, alone and in various combinations, which may be useful for industry today and a basis for further alloy development.

Further work

- Optimise the Hf level both for as cast structures (TCG formation) and precipitation of dispersoids.
- Update the Al rich part of the Al-Hf phase diagram.
- A thorough investigation of dispersoid evolution due to loss of coherency and dissolution temperature.
- Investigate whether other elements like Mg and Mn will affect the precipitation and stability of the dispersoids?
- Comparison of cold and hot deformed material with respect to dispersoid stability.
- Perform atom probe investigations concerning inhomogeneous precipitation.

Appendix

Appendix

Top of the billet

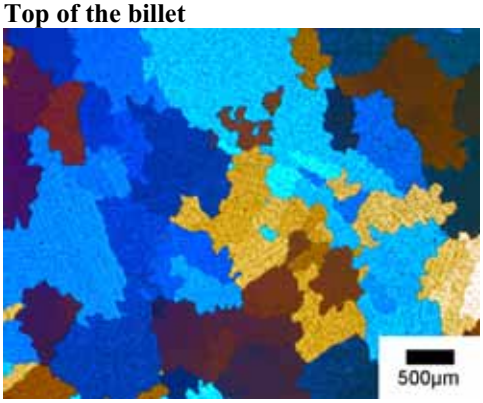

a) Alloy 1(Al-Hf-Si-Fe), anodised sample from the top

Bottom of the billet

No sample

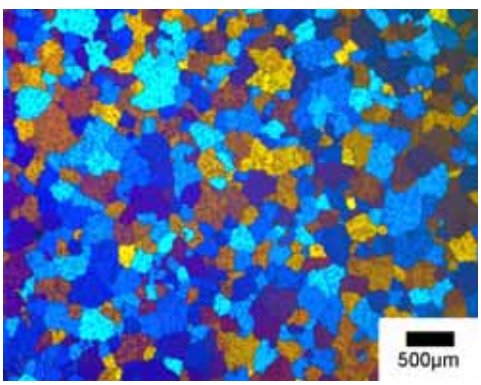

b) Alloy 2 (Al-Hf-Zr-Si-Fe) anodised sample from the top

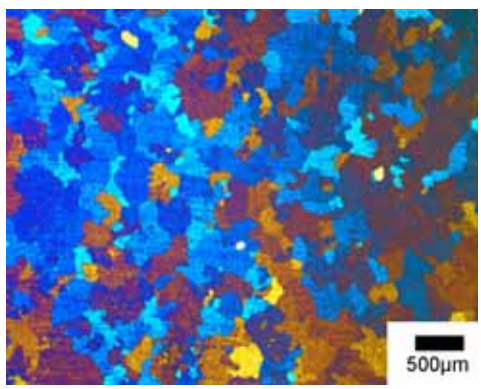

c) Alloy 2 (Al-Hf-Zr-Si-Fe) anodised sample from the bottom

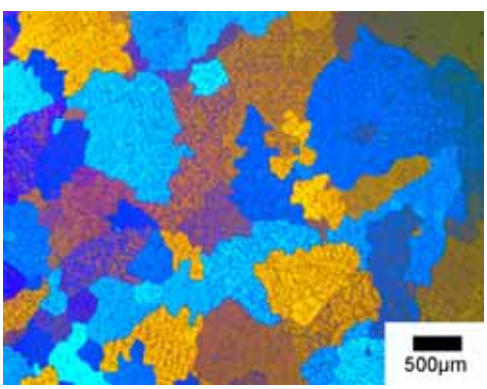

d) Alloy 3 (Al-Hf-Sc-Si-Fe) anodised sample from the top

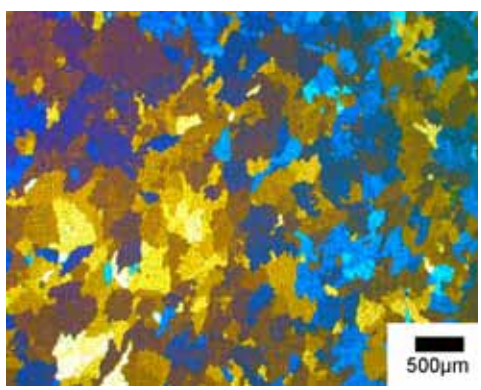

e) Alloy 3 (Al-Hf-Sc-Si-Fe) anodised sample from the bottom

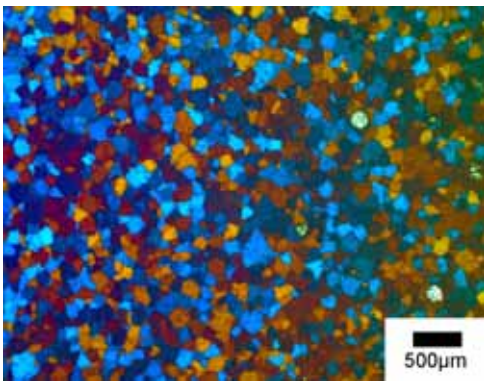

f) Alloy 4 (Al-Hf-Sc-Zr-Si-Fe) anodised sample from the top

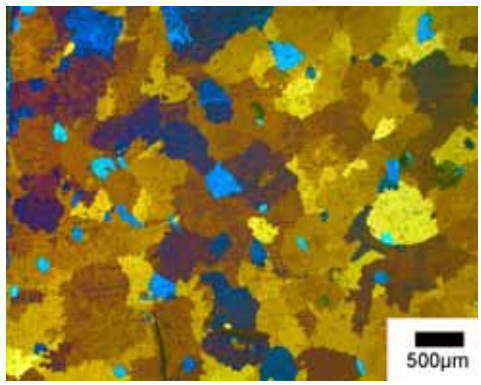

g) Alloy 4 (Al-Hf-Sc-Zr-Si-Fe) anodised sample from the bottom

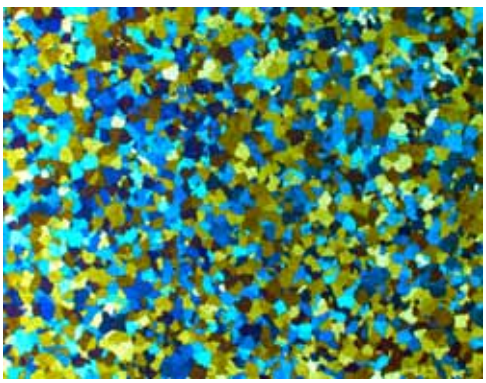

h) Alloy 5 (Al-Hf-Sc-Zr-Si-Fe) anodised sample from the top

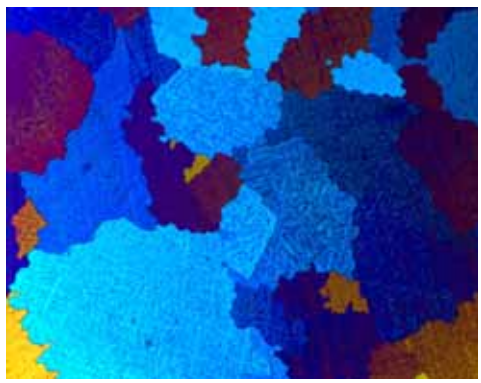

i) Alloy 5 (Al-Hf-Sc-Zr-Si-Fe) anodised sample from the bottom

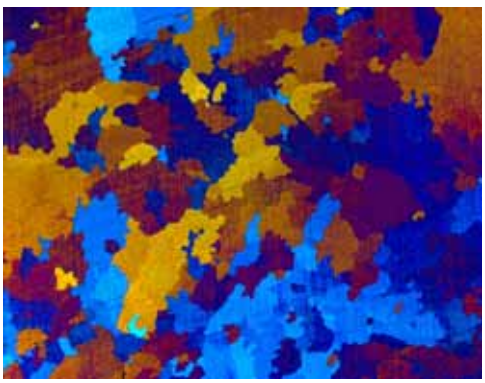

j) Alloy 6 (Al-Hf-Sc-Zr-Si-Fe) anodised sample from the top

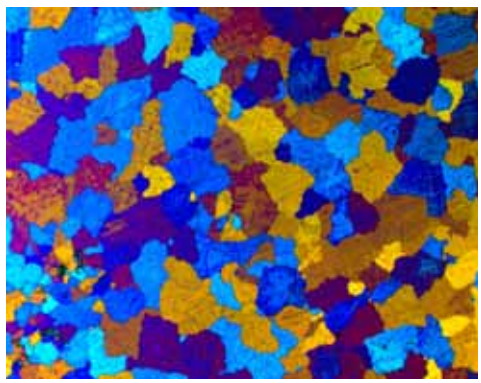

k) Alloy 6 (Al-Hf-Sc-Zr-Si-Fe) anodised sample from the bottom

Figure I Optical micrographs of anodised samples from the top and the bottom of the as cast samples. Same magnification on all of the micrographs in the ND direction.

Appendix

Table I Grain size measurements showing the difference at the top and the bottom as cast billet.

Alloys	Grain size Top (µm)	Grain size Bottom (µm)
1.Al-Hf	378	-
2.Al-Hf-Zr	163	148
3.Al-Hf-Sc	544	148
4.Al-Hf-Sc-Zr	102	223
5.Al-Hf-Sc-Zr	700	88
6.Al-Sc-Zr	213	258

Table II Data for alloy 4 (Al-Hf-Sc-Zr) for different temperatures and times.

Temperature (^oC)	Time (hr)	Dispersoid radius (nm)	St.dev	Volume fraction,f_v	Number density N	f/r (nm^{-1})
500	1	8	2,29	$3,89E10^{-2}$	$1,75E10^{22}$	$4,77E10^{-3}$
	10	9	4,33	$4,78E10^{-3}$	$1,44E10^{21}$	$5,16E10^{-4}$
	100	18	5,61	$2,07E10^{-2}$	$7,84E10^{20}$	$1,12E10^{-3}$
550	1	17	9,76	$4,13E10^{-3}$	$1,93E10^{20}$	$2,40E10^{-4}$
	10	20	6,18	$6,18E10^{-3}$	$1,81E10^{20}$	$3,07E10^{-4}$
	100	53	19,93	$5,33E10^{-2}$	$8,46E10^{19}$	$1,00E10^{-3}$
600	1	22	6,07	$3,85E10^{-2}$	$8,56E10^{20}$	$1,75E10^{-3}$
	10	55	24,82	$1,26E10^{-2}$	$1,84E10^{19}$	$2,30E10^{-4}$
	100	93	30,29	$1,21E10^{-2}$	$3,58E10^{18}$	$1,30E10^{-4}$

Table III Data for alloy 5 (Al-Hf-Sc-Zr) for different temperatures and times.

Temperature (^oC)	Time (hr)	Dispersoid radius (nm)	St.dev	Volume fraction,f_v	Number density N	f/r (nm^{-1})
500	1	7	1,30	$1,08E10^{-2}$	$8,32E10^{21}$	$1,60E10^{-3}$
	10	11	3,00	$8,67E10^{-3}$	$1,61E10^{21}$	$7,98E10^{-4}$
	100	22	5,53	$8,97E10^{-3}$	$1,97E10^{20}$	$4,05E10^{-4}$
550	1	10	2,41	$6,36E10^{-3}$	$1,50E10^{21}$	$6,33E10^{-4}$
	10	18	4,78	$9,16E10^{-3}$	$3,55E10^{20}$	$5,00E10^{-4}$
	100	56	26,71	$1,82E10^{-2}$	$2,43E10^{19}$	$3,22E10^{-4}$
600	1	22	5,33	$3,59E10^{-3}$	$1,91E10^{19}$	$1,64E10^{-4}$
	10	38	10,5	$3,25E10^{-3}$	$1,44E10^{19}$	$8,61E10^{-5}$
	100	85	32,70	$5,97E10^{-3}$	$2,33E10^{18}$	$7,03E10^{-5}$

Appendix

Table IV Data for alloy 6 (Al-Sc-Zr) for different temperatures and times.

Temperature (^{o}C)	Time (hr)	Dispersoid radius (nm)	St.dev	Volume fraction,f_v	Number density N	f/r (nm^{-1})
500	1	6	1,17	$7{,}40E10^{-3}$	$6{,}97E10^{21}$	$1{,}17E10^{-3}$
	10	9	2,33	$3{,}70E10^{-3}$	$1{,}21E10^{21}$	$4{,}11E10^{-4}$
	100	20	5,53	$1{,}27E10^{-2}$	$3{,}59E10^{20}$	$6{,}23E10^{-4}$
550	1	14	3,29	$2{,}04E10^{-2}$	$1{,}71E10^{21}$	$1{,}44E10^{-3}$
	10	24	7,30	$1{,}48E10^{-2}$	$2{,}43E10^{20}$	$6{,}07E10^{-4}$
	100	61	23,10	$1{,}51E10^{-2}$	$1{,}56E10^{19}$	$2{,}46E10^{-4}$
600	1	22	5,97	$9{,}07E10^{-3}$	$1{,}94E10^{20}$	$4{,}06E10^{-4}$
	10	51	21,22	$5{,}69E10^{-3}$	$1{,}02E10^{19}$	$1{,}11E10^{-4}$
	100	104	35,76	$1{,}24E10^{-2}$	$2{,}65E10^{18}$	$1{,}20E10^{-4}$

Publication list

Below are all the publications where I have participated during my Ph.D listed.

1. H.Hallem, W.Lefebvre, B.Forbord, F.Danoix, K.Marthinsen: The formation of $Al_3(Sc_xZr_yHf_{1-y})$-dispersoids in aluminium alloys, Submitted to Materials Science and Engineering, 2005.

2. W. Lefebvre, F. Danoix, H. Hallem, B. Forbord, A. Bostel, K. Marthinsen : Diffusion controlled formation of dispersoids in the Al-Zr-Sc-system as studied by 3D atom probe and TEM, Submitted to Acta Mater, 2005.

3. B.Forbord, L.Auran, W.Lefebvre, H.Hallem[d] and K.Marthinsen: Rapid precipitation of dispersoids during extrusion of a 3xxx-alloy with Zr and Sc, Submitted to Materials Science and Engineering, 2005.

4. B. Forbord, H. Hallem and K. Marthinsen: The Effect of Sc on the Extrudability and Recrystallization Resistance of Al-Mn-Zr-Alloys, Part 1, Proceedings of 2nd International Conference on Recrystallization and Grain Growth, Annecy, France (2004), 369-374.

5. H. Hallem, B. Forbord and K. Marthinsen: An Investigation of Cast Structures in Al-Hf-(Sc)-(Zr) Alloys and Their Subsequent Effect on Recrystallisation Resistance after Cold Rolling, Proc. 9th International Conference on Aluminium Alloys, Aug. 2-5 2004, Brisbane, Australia, eds. J.F. Nie, A.J. Morton and B.C. Muddle, Institute of Materials Engineering Australasia Ltd, 240-245

6. H. Hallem, B. Forbord and K. Marthinsen: Investigation of Al-Fe-Si Alloys with Additions of Hf, Sc and Zr Proc. 9th International Conference on Aluminium Alloys, Aug. 2-5 2004, Brisbane, Australia, eds. J.F. Nie, A.J. Morton and B.C. Muddle, Institute of Materials Engineering Australasia Ltd, 825-831

7. B. Forbord, H. Hallem and K. Marthinsen: The Effect of Alloying Elements on Precipitation and Recrystallisation in Al-Zr Alloys, Proc. 9th International Conference on Aluminium Alloys, Aug. 2-5 2004, Brisbane, Australia, eds. J.F. Nie, A.J. Morton and B.C. Muddle, Institute of Materials Engineering Australasia Ltd, 1179-1185

8. B. Forbord, H. Hallem and K. Marthinsen: The Influence of Precipitation Annealing Procedure on the Recrystallisation Resistance of Al-Mn-Zr Alloys With and Without Sc, Proc. 9th International Conference on Aluminium Alloys, Aug. 2-5 2004, Brisbane, Australia, eds. J.F. Nie, A.J. Morton and B.C. Muddle, Institute of Materials Engineering Australasia Ltd, 1263-1269

9. B. Forbord, W. Lefebvre, F. Danoix, H. Hallem and K. Marthinsen, Three dimensional atom probe investigation on the formation of $Al_3(Sc,Zr)$-dispersoids in aluminium alloys. Scripta Materialia, Volume 51, Issue 4, August 2004, Pages 333-337

10. H.Hallem, B.Forbord, K.Marthinsen, An Investigation of Dilute Al-Hf and Al-Hf-Si Alloys, Materials Science and Engineering A, Volumes 387-389, Pages 940-943, 2004.

11. Forbord, H. Hallem, N. Ryum and K. Marthinsen. Precipitation and recrystallisation in Al-Mn-Zr with and without Sc. Materials Science and Engineering A, Volumes 387-389, Pages 936-939, 2004.

12. S.Tangen, H.Hallem, H.Bjerkaas, J.Hjelen and E.Nes, Variation in subgrain structure over the cross section in an extruded Aluminium profile-Measured by EBSD, Conference proceedings Scandem , Oslo, 2003.

13. Y.Riddle, H.Hallem, N.Ryum. Highly recrystallisation resistant Al-Mn-Mg-alloys using Sc and Zr, pp. 563-568, Part 1, Proceedings of the 8th International Conference ICAA8, Cambridge, England (2002).